INSTITUTO POLITÉCNICO DE LISBOA

Instituto Superior de Engenharia de Lisboa

Escola Superior de Tecnologia da Saúde de Lisboa

Predictability of different calculating strategies for corneal tissue ablation by excimer laser

Sylvia Annabelle Grilo Gaspar

Thesis to obtain the Master's Degree in

Biomedical Engineering

Supervisors

Tiago Luís do Carmo Bravo Ferreira (Hospital da Luz Lisboa)

Pedro Manuel Alves Patrício da Silva (ISEL)

November 2022

INSTITUTO POLITÉCNICO DE LISBOA

Instituto Superior de Engenharia de Lisboa
Escola Superior de Tecnologia da Saúde de Lisboa

Predictability of different calculating strategies for corneal tissue ablation by excimer laser

Sylvia Annabelle Grilo Gaspar

Thesis to obtain the Master's Degree in
Biomedical Engineering

(Definitive Version)

Supervisors
Tiago Luís do Carmo Bravo Ferreira (Hospital da Luz Lisboa)
Pedro Manuel Alves Patrício da Silva (ISEL)

Examination Committee
Chairperson: António Jorge Duarte de Castro Silvestre (ISEL)
Main Examiner: Andreia Rosa (Faculdade Medicina, Universidade Coimbra)
Supervisor: Tiago Luís do Carmo Bravo Ferreira (Hospital da Luz Lisboa)

November 2022

[This page was intentionally left blank]

Acknowledgements

During the process of construing this Master Thesis, there were various people who have contributed for it to be accomplished and I will always remember how grateful I am to them.

Firstly, my sincere thanks to Professor Cecília Calado, who in the early stages of this work, gave me the initial guidelines.

After, I would like to express my deepest gratitude to my supervisors, Professor Tiago Bravo Ferreira and Professor Pedro Patrício for accepting this challenge, as well as for their commitment, their teachings, and for their guidance during this project.

I would like to thank the institution that made this thesis possible, Hospital da Luz Lisboa, and, in particular, Professor Filomena Ribeiro (head of the ophthalmology department), for allowing this study to be performed, always with her unique incentive and stimulation to do more and better. I also express my deep gratitude to my co-workers, who always supported me across this journey.

Finally, the last but absolutely not the least, I would like to thank and dedicate this thesis to my parents Maria Manuela Gaspar and Carlos Gaspar, for all their love, the teachings that were passed on to me and for always believing in me; to my brother Miguel Gaspar, for always looking out for me and for being such an inspiration; to my companion Pedro Nunes, who has always been my foundation throughout the hard times and has always given me the support that I needed; and to Gina Nunes and João Nunes, who have always treated me like a daughter.

To each and every one of you, a big thank you.

[This page was intentionally left blank]

Resumo

Actualmente existem vários métodos para melhorar a qualidade da visão, incluindo óculos, lentes de contacto ou recorrendo a cirurgia refractiva. A cirurgia refractiva a laser é um procedimento que recorre a laser *excimer* de modo a remover tecido corneano e corrigir erros refractivos, através da alteração do formato da córnea. Laser *excimer* TENEO 317 (Bausch & Lomb Technolas, Munich, Germany) utiliza tratamento Proscan ou Zyoptix, personalizado para cada paciente. De modo a garantir a segurança do paciente e a eficácia dos resultados, o tratamento efectuado pelo laser *excimer* tem tradicionalmente por base uma fórmula matemática, denominada fórmula exacta de Munnerlyn. Esta fórmula prevê a quantidade de tecido corneano removido (ablação) durante o tratamento, sendo que uma fórmula de Munnerlyn simplificada e aproximada permite obter este valor de uma forma mais imediata. A principal questão apresentada nesta tese tratou-se de aferir se a medição de ablação prevista pelo laser corresponde efectivamente à ablação real ocorrida na cirurgia. Adicionalmente, foi investigado se ambas as fórmulas aproximada e exacta de Munnerlyn ainda são fiáveis, para ambos os tratamentos. Para estudar esta questão, foi efectuada uma análise estatística (n = 86 olhos) de modo a avaliar qual dos seguintes seria mais preciso: simulador pertencente à plataforma do laser, a fórmula aproximada de Munnerlyn ou a fórmula exacta de Munnerlyn. A espessura da córnea (paquimetria) dos 86 olhos foi medida recorrendo a três aparelhos (tomografia de coerência óptica de segmento anterior, topografia por varrimento em fenda e tomografia de Scheimpflug) tanto no pré como no pós-operatório. Posteriormente foi realizada uma análise estatística. Os resultados para os tratamentos Proscan e Zyoptix demonstraram que a simulação do laser é precisa, quando comparado com as medições reais de ablação. Relativamente às fórmulas de Munnerlyn, concluiu-se que os cirurgiões podem confiar nestas fórmulas para o tratamento Proscan. No tratamento Zyoptix, as fórmulas de Munnerlyn subestimam a profundidade de ablação.

Esta tese também estudou: a precisão da espessura do flap (corte fino na córnea para aceder ao estroma, onde o laser é aplicado) que demostrou algumas variações que podem ser consideradas clinicamente insignificantes; e a comparabilidade entre três aparelhos diferentes de paquimetria, onde o Orbscan (Bausch & Lomb, Rochester, New York, USA) provou ser o mais variável nos seus resultados e o Pentacam (Oculus, Wetzlar, Germany) demonstrou ser o mais confiável, quando comparados com o Visante (Carl Zeiss Meditec, Jena, Germany).

Palavras-chave: Cirurgia refractiva; LASIK; laser Excimer; Ablação de tecido corneano; Fórmula de Munnerlyn

[This page was intentionally left blank]

Abstract

Currently there are many ways to improve the quality of vision, including glasses, contact lenses or refractive surgery. Laser refractive surgery is a procedure that uses an excimer laser to ablate corneal tissue and correct refractive errors by reshaping the cornea. Excimer laser TENEO 317 (Bausch & Lomb Technolas, Munich, Germany) uses either a Proscan or a Zyoptix treatment, which is customized to each patient. To guarantee patient safety and effective results, the treatment performed by the excimer laser is traditionally based on a mathematical formula, Munnerlyn's exact formula. This formula predicts the amount of corneal tissue that will be ablated during the procedure, and a simplified but approximated Munnerlyn's formula may be used to easily obtain this value. The central question of the current thesis was to measure if the corneal ablation thickness predicted by the laser corresponds to the real corneal ablation during the surgery. Additionally, we will investigate whether Munnerlyn's approximated and exact formulas are still reliable, for both types of treatment. To study this question, a statistical analysis was performed (n = 86 eyes) to test which of the following is the most accurate: the laser platform proprietary simulation, Munnerlyn's approximated formula or Munnerlyn's exact formula. The cornea thickness (pachymetry) of the 86 eyes was measured using three devices (Anterior segment optical coherence tomography, slit-scan topography and Scheimpflug tomography) both pre- and postoperatively.

An adequate statistical analysis was subsequently performed. The results for Proscan and Zyoptix treatment showed that the excimer simulation is accurate, when compared to the real measurements. Regarding Munnerlyn's formulas, we concluded that surgeons could rely on them in Proscan treatments. In the case of Zyoptix treatments, Munnerlyn's formula underestimated the ablation depth.

This thesis also studied: the accuracy of flap thickness (a thin cut in the cornea to access the stroma, where the laser acts) showed some variances that could be considered to be clinical insignificant; and the comparability among three different pachymetry devices, where Orbscan (Bausch & Lomb, Rochester, New York, USA) has proven to be the most uncertain and Pentacam (Oculus, Wetzlar, Germany) the most reliable, when comparing to Visante (Carl Zeiss Meditec, Jena, Germany).

Keywords: Refractive surgery; LASIK; Excimer laser; Corneal tissue ablation; Munnerlyn's formula

[This page was intentionally left blank]

Index

Index Figures

[This page was intentionally left blank]

List of Abbreviations

AD: ablation depth
AS-OCT: anterior segment optical coherence tomography
ATR: against-the-rule (astigmatism)
CCT: central corneal thickness
Cyl: cylinder
ECM: extracellular matrix
FS-LASIK: femtosecond assisted LASIK
FT: flap thickness
HOA: high order aberration
iFS: intralase femtosecond
LASER: light amplification by stimulated emission of radiation
LASIK: laser in situ keratomileusis
MK-LASIK: microkeratome assisted LASIK
OCT: optical coherence tomography
OZ: optical zone
PPR: predicted phoropter refraction
PRK: photorefractive keratectomy
PTA: percentage tissue altered
PRK: phototherapeutic keratectomy
RSB: residual stromal bed
SD: standard deviation
SE: spherical equivalent
Sph: sphere
WF: wavefront
WTR: with-the-rule (astigmatism)

[This page was intentionally left blank]

List of Symbols

Δapproximated: difference between real depth ablation and approximated Munnerlyn's formula

Δexact: difference between real depth ablation and exact Munnerlyn's formula

Δexcimer: difference between real depth ablation and excimer simulation

Δorbscan: pachymetry difference between Visante and Orbscan

Δpentacam: pachymetry difference between Visante and Pentacam

ArF: argon fluoride

D: dioptres

eV: electron volt

fs: femtosecond

Hz: hertz

K: keratometry

K_1: minimum (flat) keratometry

K_2: maximum (steep) keratometry

KrF: krypton fluoride

n: refractive index (of the cornea)

nm: nanometre

mJ: millijoule

mm: millimetre

R_1: original radius of curvature

R_2: radius of curvature after ablation

s: second

S_1: sagittal depth of the preoperative cornea

S_2: sagittal depth of the postoperative cornea

XeCl: xenon monochloride

XeF: xenon fluoride

μm: micrometre

[This page was intentionally left blank]

1. Objective

Excimer laser in refractive surgery is considered worldwide as the reference technique for the correction of spherical and cylindrical refractive error [1]. The success of this surgical procedure is due to its excellent results regarding safety, efficacy, and predictability. Its goal is to achieve optimal postoperative refractive results. The refractive outcomes are continually improving in consequence of the evolutions in laser platform technology and diagnostic devices. The accurate estimation of ablation depth is essential in refractive surgery regarding its safety and efficacy, because it determines the postoperative total corneal thickness, residual stromal bed (RSB) and refractive outcomes [1]. Initially, the Munnerlyn's formula was used to aid the surgeon in estimating the ablation depth. Today, the use of more complex ablation profiles, such as wavefront-guided, wavefront optimized, or topography-guided, complicates the calculation of stromal tissue consumption [1]. When planning a refractive treatment, surgeons tend to rely on the estimated ablation depth provided by the planning software of the laser platform [1,2]. Consequently, the surgeon works with this predicted value as a reference ablation depth even though it is a prediction and not an actual measurement [1]. Knowing the estimated ablation depth is important for two reasons: preoperatively, it enables surgeons to calculate the percentage tissue altered (PTA), which assesses the risk of ectasia; and postoperatively, it may be used to check whether a residual refractive error depends on the ablation depth if it was different from the preoperative estimated value [2]. These differences may depend on several factors, such as the technique used to measure the corneal thickness and the laser platform used to correct the refractive error [2]. It is important to be aware that an overestimation before surgery could exclude eligible patients from refractive surgery, while an underestimation could expose the patient to an increased risk of iatrogenic ectasia [1]. Ectasia may lead to significant visual loss [3,4] and may even require corneal transplantation for visual rehabilitation [5]. Therefore, the comparison of the predicted ablation depth with widely available objective measurements is necessary to verify the accuracy of the preoperative estimation. Corneal thickness measurements (pachymetry) may be evaluated with different devices, namely slit-scanning topography (Orbscan; Bausch & Lomb, Rochester, New York, USA), rotating Scheimpflug cameras (e.g., Pentacam; Oculus, Wetzlar, Germany), optical coherence tomography or optical low-coherence reflectometry [6].

The present thesis intends to investigate the accuracy of the ablation depth estimated by the excimer laser TENEO 317 (Bausch & Lomb Technolas, Munich, Germany) software version 1.27.2302.2, assisted with iFS Advanced Femtosecond Laser (Johnson & Johnson Vision, Irvine California, USA) version 1.70, analysing the corneal thickness difference between preoperative and postoperative measures from anterior segment optical coherence tomography Visante (Carl Zeiss Meditec, Jena, Germany). In addition, it will also discuss the comparison of pachymetry measurements from Visante with those of Orbscan and Pentacam, and the accuracy of the flap creation.

The thesis is organized as follows: In the introduction, we explore various important related topics such as corneal anatomy, refractive errors, description of the devices we are using, and explaining the refractive surgery procedure. In chapter three we will explain the methods and how the study was conducted, in chapter four we will present the results we collected, and in the next chapter, we will discuss if the ablation depth predicted by the laser is consistent with the real measurements, as well

as flap accuracy, and comparability between the three pachymetry devices. Finally, in the last chapter, we will present our conclusions and considerations.

2. Introduction

2.1. Corneal Anatomy

The optic system of our eye is constituted of various structures. The light enters the eye, is refracted as it passes through the cornea, then it passes by the pupil, being afterwards refracted by the crystalline lens [7]. The cornea and the lens act together as a combined lens to project an inverted image on the retina [7,8], more specifically in the fovea. This path is shown in Figure 1.

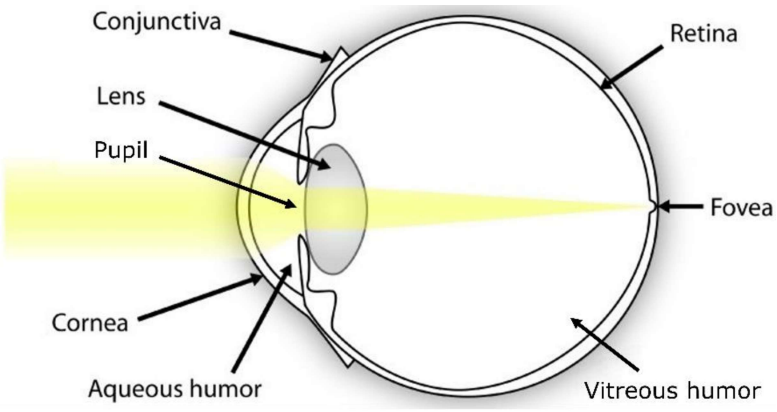

Figure 1 - The refraction of light in the human eye. Image adapted from [9].

The cornea represents approximately two-thirds of the eye's total refractive power [7–12]. In humans, the refractive power of the cornea is approximately 43 D [7,10–13]. This structure is horizontally oval, the diameter is 11 to 12 mm horizontally and vertically it measures 9 to 11 mm [7,10,13,14]. The anterior and posterior radius of curvature of the cornea has, on average, 7.8 mm and 6.5 mm, respectively [7,10]. Its shape is prolate, flatter in the periphery and steeper centrally, creating an aspheric optical system [7,11]. The central corneal thickness (CCT) ranges from 551 to 565 µm and it gradually increases towards the periphery, which ranges from 612 to 640 µm thickness [7,10]. The gradual change in tissue thickness is due to an increasing amount of collagen in the peripheral stroma [7,10]. Corneal thickness decreases with age [7,10]. The refractive index of the cornea is often quoted as 1.376 over the visible spectrum [15].

The cornea is a transparent avascular tissue acting as the primary structural barrier of the eye and protecting it against infections [7–12,14]. The tear film is the first interface between the air and the cornea, and it also affects the passage of light, the optical quality of the eye being highly dependent on its homogeneity [10,16]. Tear film has multiple roles: nutritional for the cornea, antibacterial, lubricant and refractive, contributing to the quality of vision [16,17]. The tear film is composed of three distinct layers: lipid, aqueous and mucous [10,16,18]. Recently, it has been considered to be a bi-layered structure, with aqueous and mucous layers forming a muco-aqueous gel under the lipid layer [10,16] (see Figure 2). The lipid layer constitutes the first-line protection of the ocular surface from the external environment [16]. This layer is essential since it smooths the surface of the tear film and maintains its stability, it slows evaporation and controls exchanges with the external environment [10,16]. The muco-aqueous layer consists of mucins diluted in water [16]. The aqueous part plays a primarily

antimicrobial role, and the mucous part allows the attachment of the tear film to the ocular surface epithelium through membrane mucins [16]. Mucins also favour the elimination of pathogenic organisms and external bodies by trapping them and eliminating them upon blinking [16].

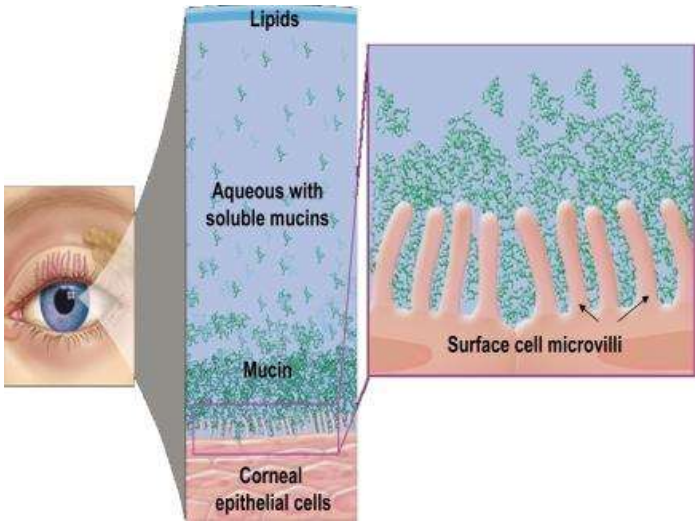

Figure 2 - Healthy tear film with lipid layer, bi-layered structure, with aqueous and mucous layers and intact surface cell microvilli. Image taken from [18].

Both cellular and acellular components are present in the cornea [7,10]. Cellular components include epithelial cells, keratocytes and endothelial cells, while acellular components are collagen and glycosaminoglycans [7,10]. The human cornea consists of six layers [7,9], represented in Figure 3, three of them are cellular, epithelium, stroma and endothelium, and two of them, Bowman and Descemet membrane, are interface layers [7]. Also, an additional acellular and strong layer in the pre-Descemet cornea called Dua's layer was recently discovered [7,9,19].

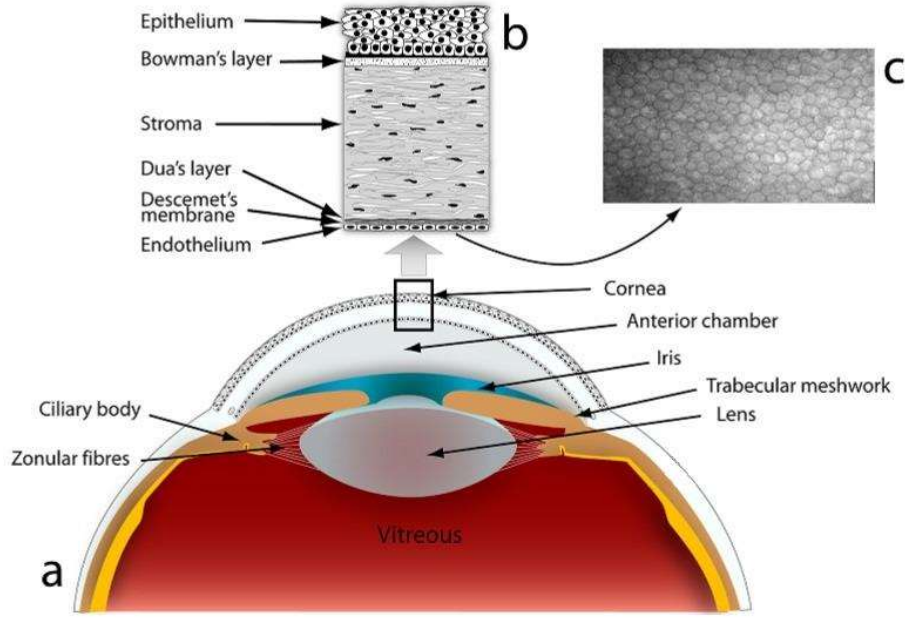

Figure 3 – Cornea anatomy. (a) Anterior section of the eye; (b) Cornea section illustrating the six layers; (c) *In vivo* confocal microscopy image of the endothelium layer. Image adapted from [9].

The epithelium is the first layer and is responsible for protecting the eye, absorbing oxygen and other nutrients [13] and is about 50 µm thick [8–10,14,17]. The epithelium is covered with the tear film and has a symbiotic relationship with it, which is optically important in smoothing out micro irregularities of the anterior epithelial surface [7,10,11]. The corneal epithelium is composed of five to seven cell layers of stratified and non-keratinized squamous epithelial cells [8–10]. More specifically, the epithelium layers consist of three types of cells, superficial cells, wing cells and basal cells [8,10] (its representation is in Figure 4). The most superficial layers consist of two to three flat polygonal cells, with microvilli on the surface increasing the surface area [8,10,11]. They have tight junction complexes to prevent tear film fluid from entering the intercellular spaces [8,10,11]. This barrier also prevents toxins and microorganisms from entering deeper into corneal layers [8,11]. The wing cells are two to three layered and named wing cells because of their shape [10,11,14]. Basal cells are a single layer in a cuboid or columnar form, making up 20 µm in thickness [10,11]. They have abundant organelles and are mitotically active [10]. Besides stem cells and transient amplifying cells, basal cells are the only corneal epithelial cells capable of mitosis [11]. They are also the source of the wing and superficial cells [8,10,11].

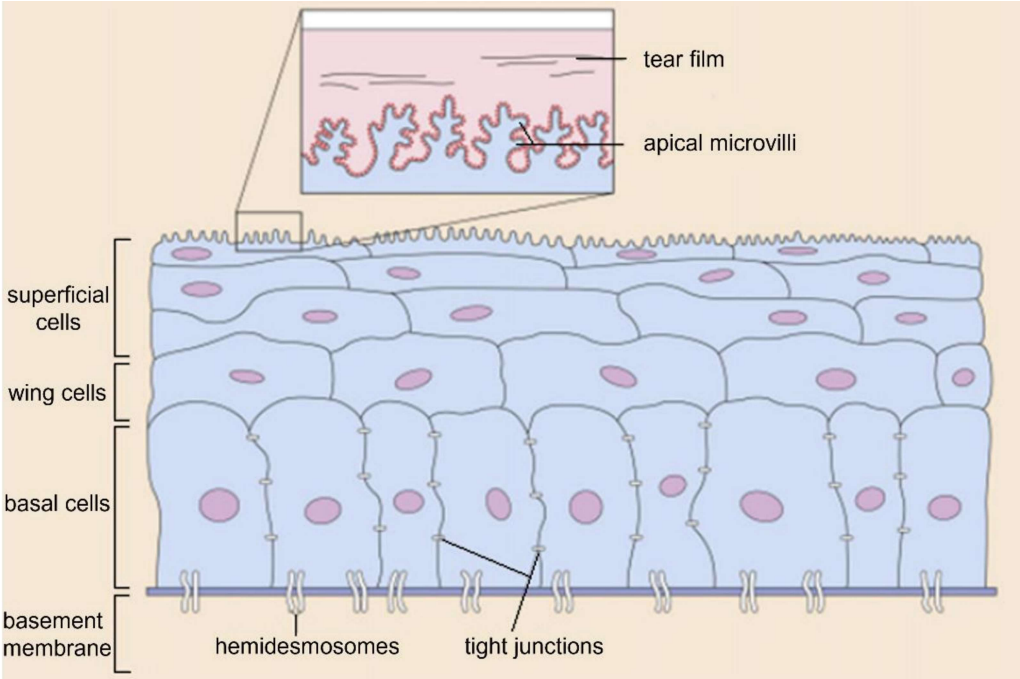

Figure 4 – Corneal epithelium composition representation. Image adapted from [11].

Basal cells are attached to the underlying basement membrane by hemidesmosomes [8,10,11,14] (see Figure 5). The strong attachment prevents the epithelium from separating from the underlying layers [10,11]. An abnormality in this attachment may result in corneal erosions or persistent epithelial defects [10,11]. The epithelium basement membrane is 40 to 60 nm thick and composed mostly of collagen (type I and IV) and laminin secreted by the basal cells, forming the *lamina lucida* and *lamina densa* [8,10,11,17]. From the basal epithelial cells, anchoring fibrils pass through the basement membrane ending up as anchoring plaques [10].

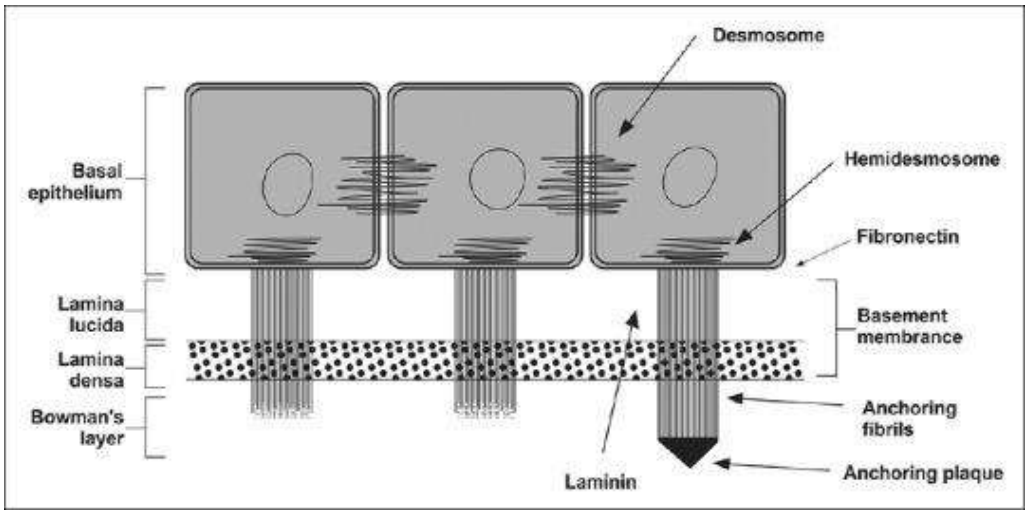

Figure 5 – Illustration of the junctional complexes of the corneal epithelium. Image taken from [10].

If the basement membrane is damaged, fibronectin levels increase and the healing process may be prolonged up to six weeks [7,10,11]. Corneal epithelial cells regularly undergo apoptosis and desquamation, and their turnover is assured by the basal layer [8,14]. The life span of epithelial cells is seven to ten days [7,8,10,14].

Bowman's membrane is situated between the basement membrane of the epithelial cells and just anterior to the stroma [7,8,11,14]. It is not a true membrane, but rather an acellular condensate of the most anterior portion of the stroma [7,8,11,14] (see Figure 6). It is about 12 µm thick and is a condensation of collagen and proteoglycans [9,10]. It is believed that this smooth layer helps the cornea maintain its shape [7,10,11,20]. However, when injured, it does not regenerate and scarring may occur [7,8,10,11]. Bowman's layer thins with ageing [20].

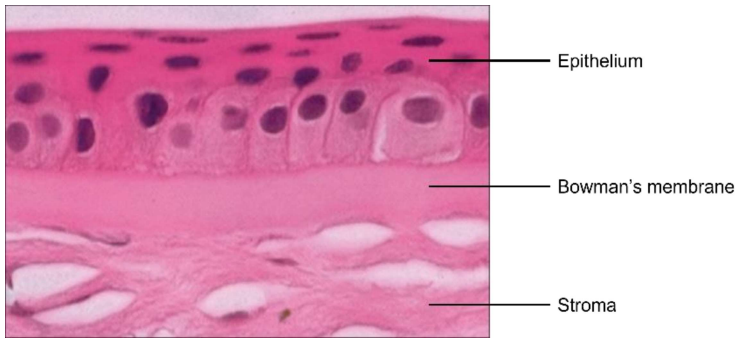

Figure 6 – Histologic cornea's cut of epithelium and Bowman's membrane. Image adapted from [10].

The stroma forms the bulk of the structure of the cornea [7,11] and represents 90% of its thickness [8,13,14,20]. The corneal stroma is composed of extracellular matrix (ECM), water and keratocytes [10,20]. It is transparent, which is a result of the precise organization of its fibres and ECM [10,11]. The ECM is composed of collagen lamellae, which are regularly arranged, and glycosaminoglycans [10]. Keratocytes are the major cell type of stroma, mostly being found in the anterior stroma [7,12]. They are involved in maintaining the ECM environment and they can synthesize collagen and glycosaminoglycans, while also creating matrix metalloproteinases, all necessary to maintain stromal

homeostasis [11]. Anterior corneal stroma rigidity appears to be especially important in maintaining the curvature of the cornea, as the anterior curvature resists changes to stromal hydration much more than the posterior stroma [7,10,14].

An additional acellular, well-defined and strong layer in the pre-Descemet cornea called Dua's layer was recently discovered and is 6 to 15 μm thick [7,9,17,19]. It consists of five to eight lamellae of collagen fibres, with no keratocytes [12,19].

Descemet's membrane is an elastic layer with a thickness of approximately 7 μm [7,13]. With age, the membrane thickens and can become up to 10 μm thick [8,11,13,14]. As the basement membrane of the endothelium, Descemet's membrane assists in the maintenance of corneal dehydration [8,14].

The endothelium layer is a single layer of 5 μm thickness, and its cells are hexagonal and metabolically active [7–10,13,14]. This monolayer has no continuous protein network [17]. The layer appears as a honeycomb-like mosaic (see Figure 7) when seen from the posterior side [7,10,11].

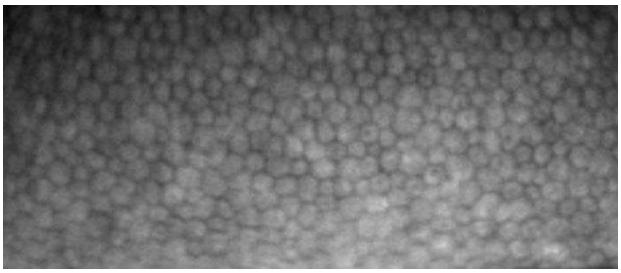

Figure 7 - Endothelium cells layer, on the specular microscopy (image obtained from Hospital da Luz).

The basal surface of the endothelium contains numerous hemidesmosomes promoting adhesion to Descemet's membrane [8,11] and lateral gaps and tight junctions [8,14]. The main function of the endothelium is to control stromal dehydration to prevent the formation of corneal oedema, which leads to the loss of transparency and consequently vision [8,14]. This dehydration is mediated by a pump-leak process as fluid leaves from the corneal stroma down the osmotic gradient from a relatively hypo-osmotic stroma toward a relatively hypertonic aqueous humour [11]. Endothelial cell density continues to change with ageing, declining from the second to the eighth decade, but also by trauma, inflammation and other diseases [11]. Endothelial cells are incapable of mitosis and therefore cannot regenerate *in vivo* [7,8,11,13,14]. Replacement of endothelial cell function from damage and cell death occurs not through cell division but migration, with centripetal migration of adjacent endothelial cells into the injured region [14]. The process of resurfacing the injured area is completed in three stages that can take several weeks [11]. The first stage is characterized by the establishment of initial coverage of the wound by migration of adjacent endothelial cells, which forms a temporary incomplete barrier with reduced pump sites and incompletely formed tight junctions [11,14]. In the second stage, the barrier and subsequently the number and quality of pump sites return to normal levels, the endothelial cells form irregular polygons, the corneal thickness typically returns to normal, and transparency is restored [11,14]. The third stage involves remodelling of the endothelial cells to form more regular hexagons, which can continue for several months [11,14].

The cornea is one of the most densely innervated tissues in the human body [7,14,21,22]. Corneal nerves are responsible for sensations of touch, pain, and temperature and play an important role in

blink reflex, wound healing and tear production and secretion [22,23]. Sensory nerves from the nasociliary branch of the ophthalmic division of the trigeminal nerve course radially toward the central cornea through the anterior stroma [14]. Thick and straight stromal nerve (see Figure 8) extends laterally and anteriorly to give rise to plexiform arrangements of progressively thin nerve fibres at several levels within the stroma [7]. Between Bowman's layer and the anterior stroma, these nerves form the subepithelial nerve plexus, and then perforate Bowman's layer to become the sub-basal epithelial nerve plexus, innervating the basal epithelial layer [14,21]. This is characterized by tortuous, thin beaded nerve fibres interconnected by numerous nerve elements [7]. The cornea also contains autonomic sympathetic nerve fibres [7].

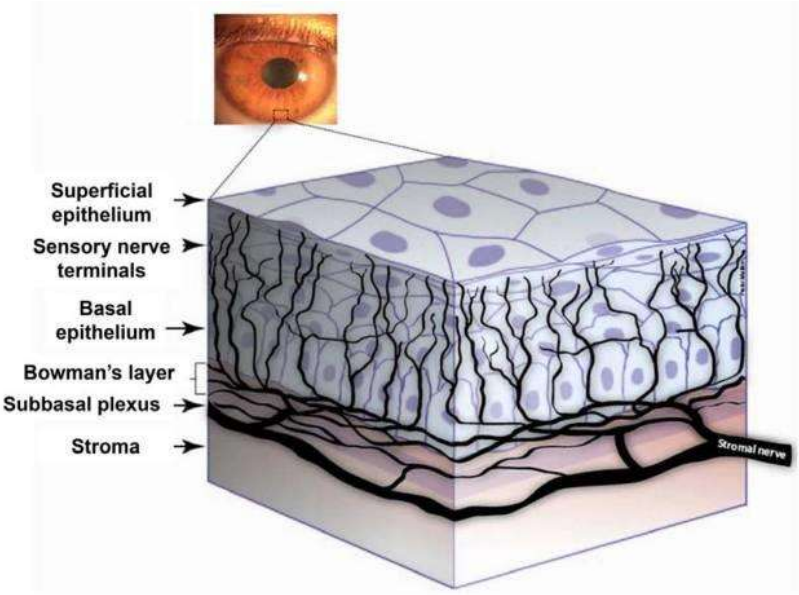

Figure 8 - Representation of human corneal nerves. Image taken from [21].

Although the cornea is avascular, it still relies on components of the blood [7,11]. It is supplied by very small vessels at the limbus [7,11].

Many factors contribute to corneal transparency, such as the regularity of the surface and thickness of the epithelium in association with the integrity of the lacrimal film, the regular architecture of the collagen fibrils in the stroma, the production of soluble crystalline proteins and the presence of proteoglycans produced by the stromal keratocytes, the regulation of the hydration level by the endothelium and the absence of vascularisation [8].

2.2. Refractive Errors

Ametropia (or refractive error) is the most frequent reason for the reduction in visual acuity [24,25]. The presence of any refractive error influences the total refractive power of the eye, and it prevents the correct focusing of light in the retina, and consequently a proper visual acuity [7]. This can be due to the shape of the eye (a longer or shorter axial length), abnormalities in the cornea (steeper or flatter radius), or lens (thickness or changes in shape) [7]. The types of refractive errors are myopia, hyperopia, astigmatism, and presbyopia [7,25].

Myopia, also known as nearsightedness, is when distant objects are not seen in focus [7,24]. The parallel rays of light of a distant object form in front of the retina and the image is thus blurred at the fovea [7,24–26]. The reason is that the refractive power of the visual system is too high in relation to the length of the eye [24] or the axial length is longer than normal [25].

Hyperopia, also known as farsightedness, a relaxed gaze into the distance results in a blurred image [24]. Parallel rays of light in the non-accommodating eye are focused posterior to the retina [25,26]. The reason is that the refractive power of the visual system is too small regarding the length of the eye, the focused image of a distant object lies behind the retina and the image on the retina is thus unclear [24,25] or the axial length is shorter than normal.

Astigmatism may be due to congenital and/or acquired reasons, including corneal diseases, trauma, and ocular surgery [7,27]. Astigmatism occurs when parallel rays of light entering the eye are not focused on a single point in the retina [7,25,27]. Most astigmatism has a corneal origin, but the lens and the retina may also have an effect (which in general is minimal) [7,26,27]. In individuals with corneal astigmatism, the cornea is steeper in one meridian than the other [7,27]. Astigmatism is classified according to its axis, which is corrected with a positive lens: with-the-rule (WTR) between 60 and 120 degrees; against-the-rule (ATR) between 150 to 180 and 0 to 30 degrees; or oblique between 31 to 59 or 121 to 149 degrees [7,27]. Corneal astigmatism may also be influenced by the tear film, the anterior and posterior curvature of the cornea, as well as the aqueous humour [7]. While most of the eyes have a small amount of irregular astigmatism, it becomes clinically significant in irregular corneas, such as the cases of corneal scars or corneal ectasia [7,27].

In presbyopia, or age-related farsightedness, the eye is restricted in its ability to focus on close objects [7,24]. The underlying causes are loss of elasticity of the ocular lens and structural change in the area of the zonular fibres and the ciliary muscle [24].

2.3. Slit-Scanning Elevation Topography (Orbscan IIz)

The word ‘‘topography’’ is derived from Greek as the combination of ‘‘to place’’ (*topo*) and ‘‘to write’’ (*graphein*), which means to describe a place [28]. The term ‘‘corneal topography’’ has been classically used for the reconstruction of the anterior corneal surface, which was, until recently, only achieved by reflective, Placido disc-based systems [28]. Slit-scanning elevation topography is a combination of a projective technique (slit-scanning) and a reflection technique (Placido-disc principle), with the aim of obtaining anterior and posterior curvature measurements and mapping both the anterior and posterior corneal surfaces [13,29]. Placido targets refer to a series of crosshairs that are projected onto the anterior cornea [30]. Disk-based corneal topography captures the Placido targets and calculates corneal curvature based on the size and distortion of the mires [30]. During image acquisition, forty slits are projected sequentially on the cornea, and its anterior and posterior edges are captured and analysed [13,29]. Like terrain topography, in which the surface elevation or depression of the terrain is shown in reference to the sea level, the corneal surface elevation is measured from a reference sphere [13]. In this case, the reference is not fixed because it is freely adjusted to each patient’s cornea to reach the best fit in diameter and position, producing a “best-fit sphere” [13,29]. This device measures both the anterior and posterior surfaces, which is especially useful for assessing corneas

with keratoconus or ectasia disorders or from patients who have undergone refractive surgery [13]. The Orbscan IIz (Bausch & Lomb) (Figure 9), determines the corneal thickness as the difference between the anterior and posterior corneal surfaces [13].

Figure 9 – Orbscan IIz device (photo taken at Hospital da Luz).

The union of computer software analysis with high-resolution concentric ring keratoscopic images allows the creation of colour-coded topographic maps of the cornea [7], in which green represents the normal range of corneal pachymetry, blue and purple colours indicate thicker areas and yellow and red indicate thinner areas [13] (see Figure 10).

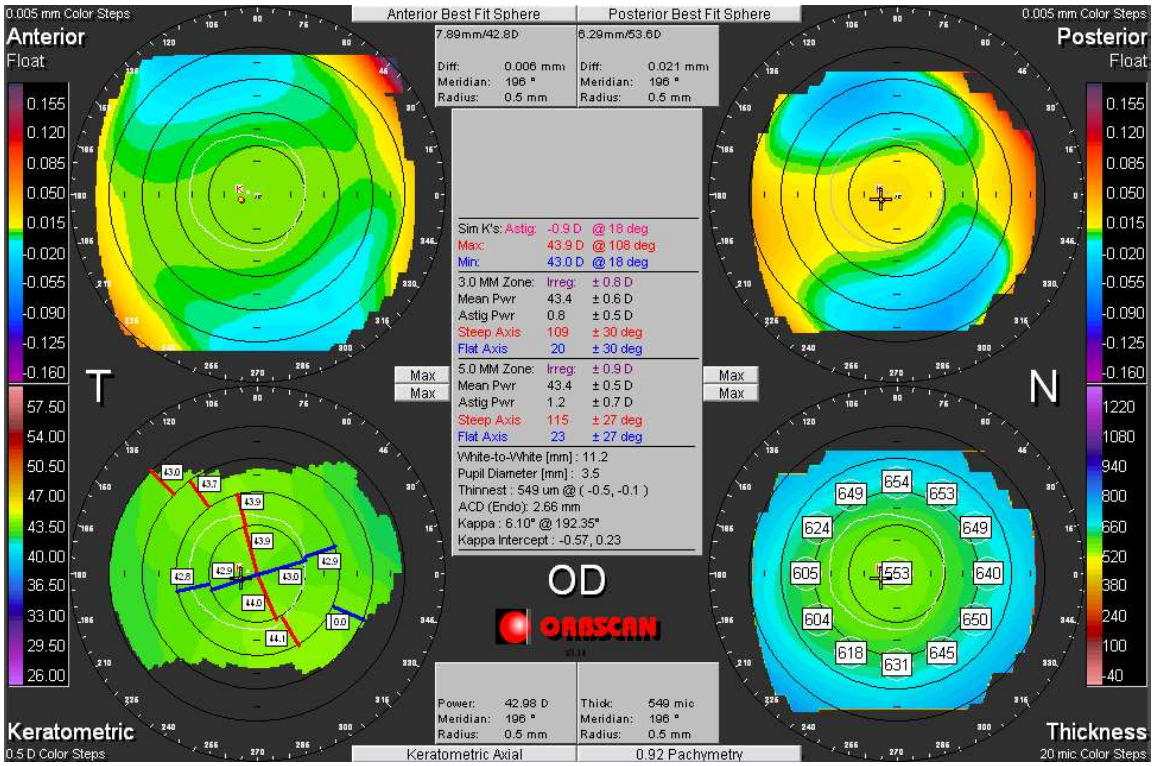

Figure 10 – Orbscan display (image obtained from Hospital da Luz).

This map also includes numeric values for corneal pachymetry. The wide spectrum of possibilities made this technique one of the most popular tools used for pre-refractive surgery evaluations [13]. Despite the learning curve required to conduct reliable examinations, the Orbscan presents good repeatability (± 3 μm) and provides a wide range of quantitative and qualitative information that can be used in clinical practice [13].

2.4. Aberrometer (Zywave)

Aberrometers measure the distortion of a wavefront (WF) of light in an optical system [31,32] by sending an infrared laser beam into the eye, through the pupil, to the retina and analysing the reflected ray [33,34]. In a perfect optical system, the light ray that emerges from the eye would be parallel to the one emitted and an undistorted plane wavefront would be formed [33]. In human eyes, the information that reaches the sensors of the aberrometer reveals the diverge imperfections of the optical components within the eye [32,33]. These optical imperfections prevent the light from focusing perfectly on the retina [32]. There are two kinds of aberrations: the low order aberrations (0, 1st and 2nd order) and high order aberrations (3rd, 4th, … order). The low order aberrations are also described as refractive errors, and this term in WF technology defines the second order Zernike polynomials [32]. The high order aberrations (HOAs) term is used to describe Zernike aberrations above second order [32]. These will worsen image quality even when lower order has been corrected [35]. High order aberrations are clinically relevant, as they are associated to night halos and glare [35]. The wave aberration is usually defined mathematically by a series of Zernike polynomials, that help to classify and represent optical aberrations [32]. Zywave (Bausch & Lomb, Rochester, New York, USA) (Figure 11), is a Shack-Hartmann aberrometer used to measure ocular aberrations [34,35].

Figure 11 – Aberrometer device (photo taken at Hospital da Luz).

This aberrometer was designed to measure the refractive errors over a range of +6.00 to −12.00 D and up to 5.00 D of cylinder, which represents the second order aberration of the eye [34]. Second order aberrations are the most important of the lower order aberrations [32,33], since they represent

more than 90% of the eye's total aberrations [35]. Although higher order WF errors are only a small fraction of the total optical aberrations of the eye, when combined with the additional aberrations induced by a laser refractive surgical treatment, they can become significant, reducing visual quality [34]. It is important to have HOAs information, since it will help the surgeon to decide which treatment is more suitable for the patient (see Figure 12). A Zyoptix treatment is a wavefront-guided customized aspheric procedure that considers the HOAs and minimizes the induced spherical aberrations. A Proscan treatment intends to create a natural aspheric shape of the cornea, aiming to reduce undesired surgical induced spherical aberrations.

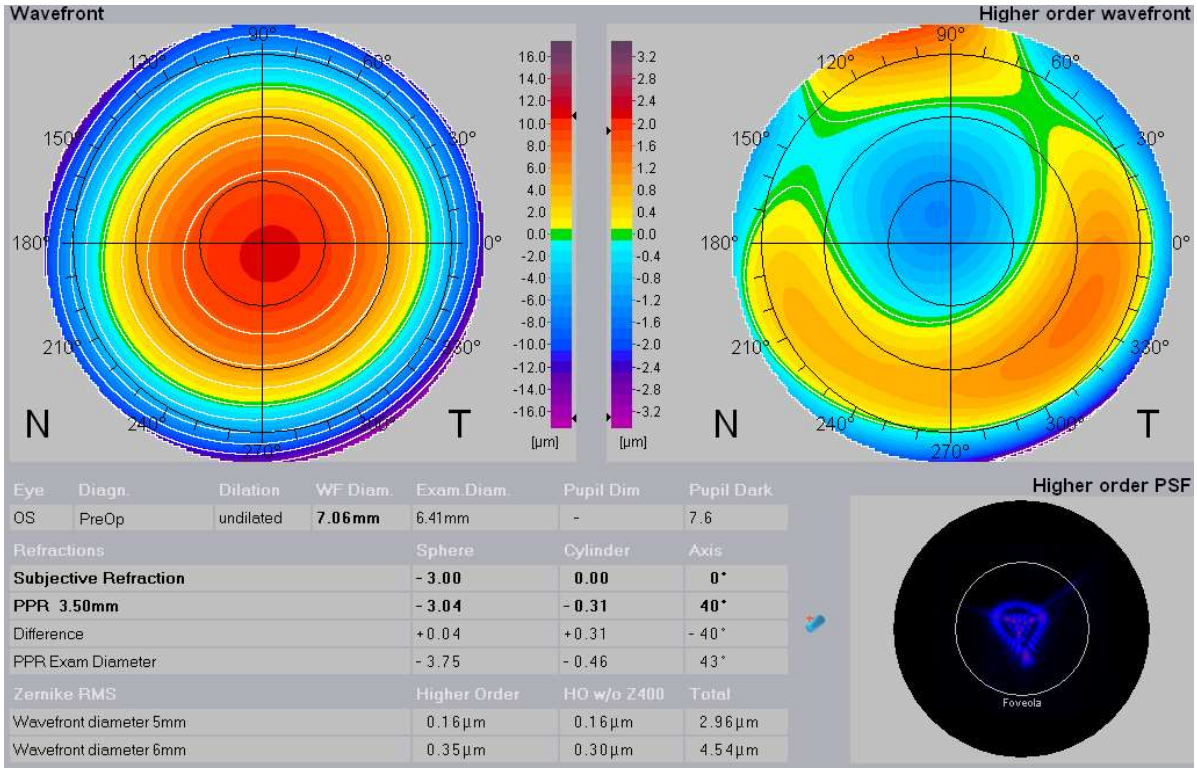

Eye	Diagn.	Dilation	WF Diam.	Exam.Diam.	Pupil Dim	Pupil Dark
OS	PreOp	undilated	7.06mm	6.41mm	-	7.6

Refractions	Sphere	Cylinder	Axis
Subjective Refraction	-3.00	0.00	0°
PPR 3.50mm	-3.04	-0.31	40°
Difference	+0.04	+0.31	-40°
PPR Exam Diameter	-3.75	-0.46	43°

Zernike RMS	Higher Order	HO w/o Z400	Total
Wavefront diameter 5mm	0.16µm	0.16µm	2.96µm
Wavefront diameter 6mm	0.35µm	0.30µm	4.54µm

Figure 12 – Aberrometer display (image obtained from Hospital da Luz).

2.5. Scheimpflug Imaging (Pentacam HR)

The word ''tomography'' is derived, from the Greek, as the combination of ''to cut" or "to section'' (tomos) and ''to write'' (*graphein*), which means to describe a place [28]. Corneal tomography is related to a three-dimensional reconstruction of the cornea and should be used for the characterization of the elevation of the front and back surfaces of the cornea, along with pachymetric mapping [28]. The Pentacam HR (Oculus) (see Figure 13) is a non-contact anterior segment tomographer with a rotating Scheimpflug camera that uses a 475 nm monochromatic slit of light to illuminate the cornea and a 1.45 megapixel camera for photography [29,36]. The camera rotates and it takes twenty five or fifty slit images of the anterior segment of the eye [13,29,36,37].

Figure 13 - Pentacam HR device (photo taken at Hospital da Luz).

These images are then reconstructed in a three-dimensional image, and the software generates different parameters [13,30]. The Pentacam represents its maps in the same colour-coded manner as the Orbscan maps, where green indicates normal values and reddish colours indicate values of concern [13] (see Figure 14). Similar to the Orbscan, the Scheimpflug imaging devices describe different corneal parameters and offer a wide range of variables and maps [13,30]. The Scheimpflug imaging devices provide corneal topography data, keratometry, radius of curvature, corneal power (with the axis and amount of astigmatism), pachymetry data (corneal thickness at the apex, at the thinnest corneal point, etc.), corneal eccentricity, anterior chamber depth, pupil diameter, angle size, degree of lens opacification and lens thickness [13,30] (also seen in Figure 14, on the left).

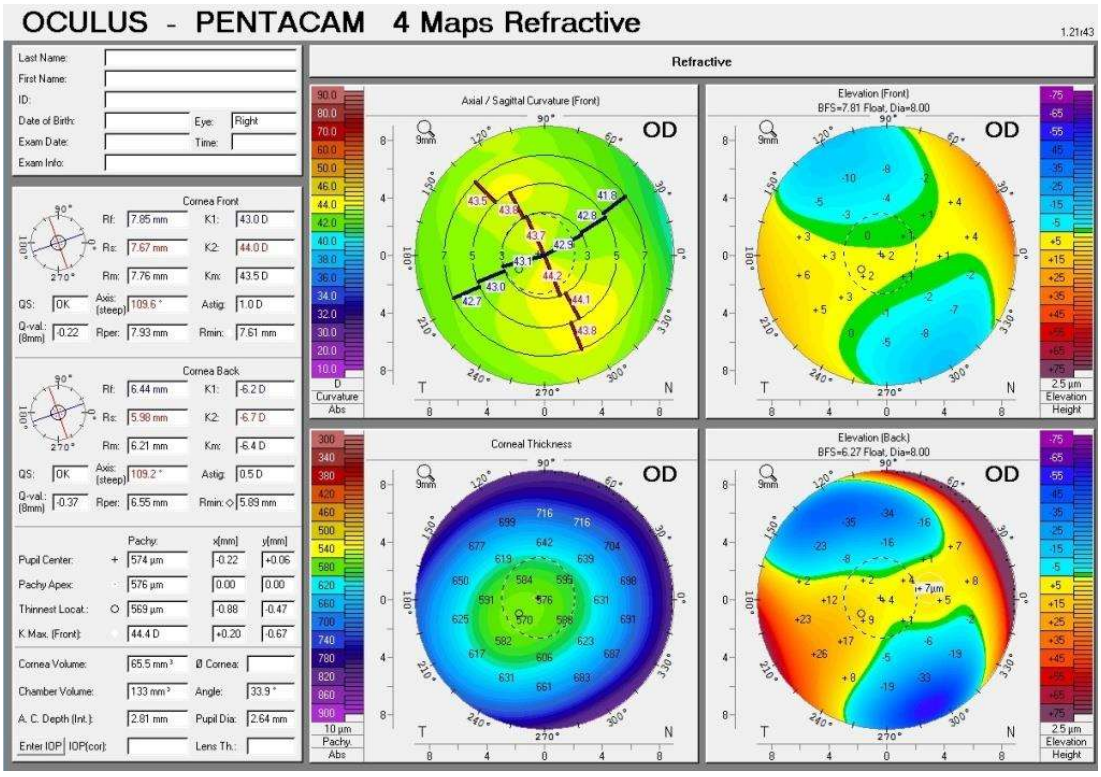

Figure 14 - Pentacam display (4 Maps Refractive) (image obtained Hospital da Luz).

When measuring and visualizing the anterior segment of the eye, Scheimpflug photography is a valuable tool in clinical practice, being one of the most used pre-surgical assessments [13] with ± 3 µm accuracy and repeatability [38].

2.6. Anterior Segment – Optical Coherence Tomography (Visante)

The optical coherence tomography (OCT) is used *in vivo* for imaging of the human retina and it is also applied to the anterior segment of the eye providing qualitative and quantitative information [13,37,39]. Anterior Segment - Optical Coherence Tomography (AS-OCT) Visante is a computerized instrument that acquires and analyses cross-sectional scans of the anterior segment of the eye [40]. Visante uses low coherence interferometry to compare the delay of infrared light reflections across tissues against a reference reflection [40–42], providing detailed *in vivo* examination of the anterior segment of the eye, without contact [6,40–42]. There are many applications for the Visante AS-OCT including accurate topography for keratoconus, anterior chamber angle assessment, planning and after corneal surgery, and research [41]. The AS-OCT Visante from Zeiss (see Figure 15), provides excellent high-resolution images of the anterior segment of the eye [41].

Figure 15 – AS-OCT Visante device (photo taken at Hospital da Luz).

Corneal surgeries such as refractive surgery require accurate preoperative measurements to reduce the risk of corneal ectasia, and postoperative assessment of complications such as interface fluid syndrome or inflammation [42]. High-resolution AS-OCT is useful in refractive surgery procedures, such as LASIK, because it allows the evaluation of the flap, with accurate measurements (see Figure 16) and the residual stromal bed thickness [13,39,41,42]. Its software can measure corneal thickness at any desired point, using the flap tool option by manually placing the cursors of the calliper at the limits of the anterior and posterior corneal surfaces [40].

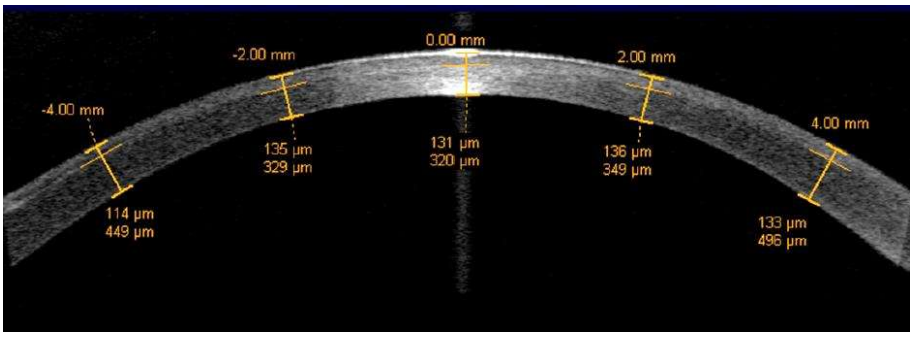

Figure 16 - High-resolution images of the cornea and the flap tool (image obtained from Hospital da Luz).

AS-OCT is useful to localize the demarcation line within the stroma (that indicates the transition zone between the untreated and the treated tissue) and measure the depth of this line [13]. The perpendicularity of the scanning laser beam to the central corneal surface is adjusted by placing the vertex at the centre of the OCT image and maximizing the vertex reflection [6].

2.7. Refractive Surgery

The effect of refractive surgery on patients extends beyond glasses independence, with the procedure leading to improved quality of life, and improved daily working performance [43]. Laser technology, such as the excimer laser and the femtosecond laser, have brought an era of corneal lasers in refractive surgery [44]. Excimer laser, commonly referred to as laser eye surgery, is considered worldwide as the reference technique for correction of ametropias, such as myopia, hyperopia, and astigmatism [1,45–48]. The laser irradiates the corneal stroma, to reshape the anterior surface of the cornea, thus changing its refractive power, as represented in Figure 17, to improve visual acuity with minimal patient discomfort [31,46,49].

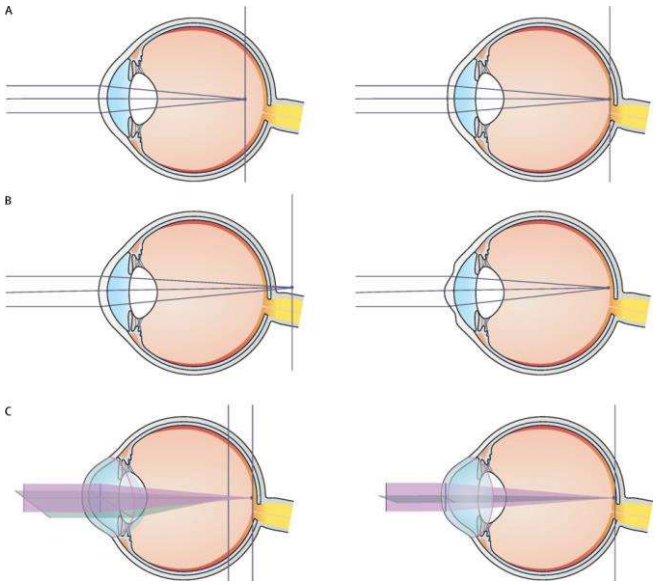

Figure 17 - Refractive errors before (left) and after (right) surgery. (A) Correction of myopia using central ablation to flatten the corneal curvature; (B) Correction of hyperopia using mid-peripheral ablation to steep the corneal curvature; (C) Astigmatic correction restores an ellipsoid-shaped eye to its normal spherical shape by flattening a specific axis. Image taken from [43].

Candidacy criteria includes sufficient corneal bed thickness following flap formation and corneal ablation, a healthy tear film, and the presence of a regular corneal topography [45].

Surface ablation techniques include photorefractive keratectomy (PRK), which involves removal of the epithelium through several methods (see Figure 18), followed by ablation of the Bowman's layer and the anterior corneal stromal tissue [43]. PRK is less involved in the development of postoperative ectasia and therefore can be considered the technique of choice for patients with thin corneas and for patients with recurrent corneal erosion syndrome, corneal dystrophies, dry eye disease or patients who have an increased risk of trauma [31].

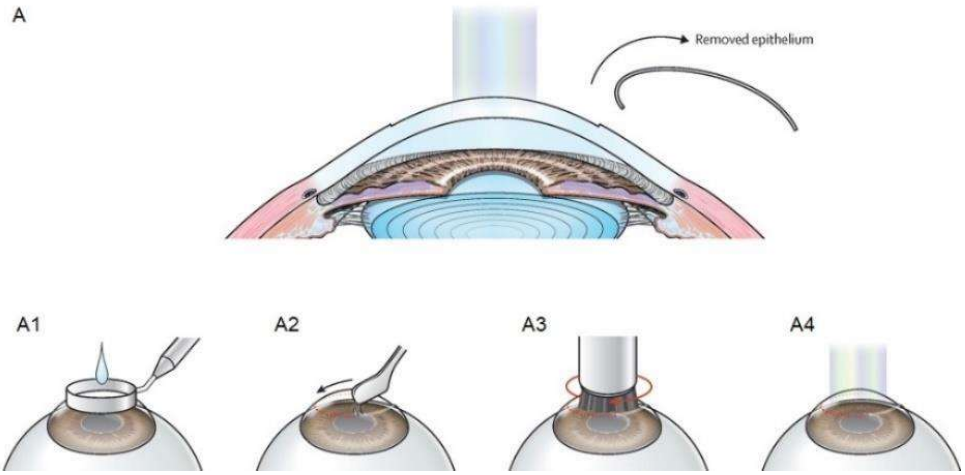

Figure 18 - (A) Surface ablation after the epithelium is removed and the excimer laser is applied in the corneal surface. There are several methods of epithelium removal: (A1) the trephine is centred and pressed on the corneal epithelium, and diluted alcohol is applied to loosen the epithelium; (A2) a blunt blade is used to scrape the epithelium; (A3) an Amoils brush can also be used to assist epithelium removal; (A4) with transepithelial PRK, a laser profile of phototherapeutic keratectomy (PTK) and laser treatment for refractive correction are performed in one step. Image adapted from [43].

Compared with PRK, visual recovery is faster and visual outcome is rapidly stable after laser in situ keratomileusis (LASIK) [44]. LASIK involves the creation of a thin cut in the cornea, called a flap. This flap is then pulled back, to enable remodelling of the tissue underneath with laser and repositioning the flap back after the corneal ablation has been performed [48,49] (see Figure 19). The corneal flap is created with a mechanical microkeratome or femtosecond (fs) laser [49]. It is well known that in LASIK, flap creation is a critical step in the procedure and that the goal is to obtain a flap of predictable thickness and morphology, that modifies corneal biomechanics as little as possible [50]. Consistent and thinner flaps allow more available thickness for ablation and result in increased speed of visual recovery after surgery [23,47].

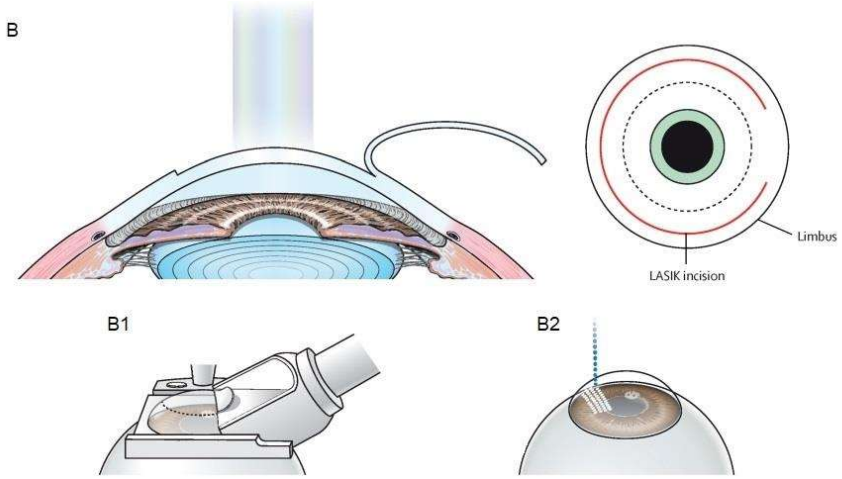

Figure 19 - (B) Surface ablation after the corneal flap is created by cutting the corneal tissue, leaving a hinge area; There are two methods to create the corneal flap: (B1) traditional mechanical LASIK, a hand-guided, oscillating blade (known as a microkeratome); (B2) femtosecond laser-assisted LASIK surgery, the femtosecond laser moves back and forth, emitting short, rapid bursts of laser light that create a series of minute bubbles at a predetermined depth. The mechanical or laser-created flap is then lifted, exposing the region of the cornea to be ablated. Image adapted from [43].

After this laser refractive surgery, there is a corneal response that induces keratocyte apoptosis [48]. Proliferation and migration of keratocytes begin within 12 to 24 hours, giving rise to activated keratocytes and myofibroblasts, which are critical components in the wound-healing cascade [48]. The timing, intensity, and spatial distribution of wound healing differ significantly between LASIK and PRK. This is because PRK involves injury on a broader area and removal of the epithelium, epithelial basement membrane, Bowman's layer, and a portion of the anterior stroma, while LASIK leaves these structures relatively undisturbed, except at the flap margin [48].

2.8. Corneal Flap

The first step in LASIK is the creation of the corneal flap, which is a critical and important step during this procedure [44,51]. There are various options to create the corneal flap, from automated microkeratome to femtosecond laser [23,51,52]. The choice depends on surgeon preference, and each affords different theoretical advantages [52]. The mechanical microkeratome uses shear force using an oscillating blade, travelling across the cornea in a torsional or translational approach [52]. With this method, the flap is thinner centrally and thicker peripherally, which increases the incidence of buttonhole perforation [44]. Because of this instability, corneas may be too steep, too flat, or too thin even after a successful procedure [44]. Regarding femtosecond lasers, it emits light pulses of short duration (10^{-15} s) with 1043 or 1053 nm wavelength (depending on the equipment), a 3 µm spot size and uses brief laser pulses to disrupt a lamellar plane with minimum collateral damage [30,44,52,53], which results in a smoother surface quality [48]. This enables bladeless incisions to be performed within the tissue at various patterns and depths with high precision [54]. Advantages of bladeless femtosecond assisted LASIK (FS-LASIK) over conventional microkeratome assisted LASIK (MK-LASIK) includes a decrease in flap complications, such as buttonhole or free cap formation, a decrease in the risk of infection, less induction of dry eye, and a gentler approach with minimal or no

transient visual loss (blackout period) due to close physiologic maintenance of intraocular pressure throughout the procedure [44,52,54]. Flap centration, diameter, and thickness are also more precise in femtosecond-created flaps since these parameters can be personalized with the surgeon's preferences [44]. Furthermore, the femtosecond laser allows thin and uniform flaps, which improves the stability, safety and precision of the flaps with minimum effects on stromal architecture [44]. Yet, the mechanical microkeratome remains a cost-effective method for LASIK flap creation [52]. Several studies have compared these two methods for corneal flap creation and found that the implementation of femtosecond laser has dramatically improved the safety, efficacy, reproducibility, and predictability of LASIK flaps [23,54–56]. After the laser has reshaped the stromal layer, the flap is carefully repositioned over the treated area by the surgeon and checked for the presence of air bubbles, debris and proper position on the eye [48]. The flap remains in position by natural adhesion until healing is completed [48].

Accurate measurement of flap thickness and estimation of RSB thickness during LASIK surgery are essential for preventing complications [52,57]. Determining whether sufficient tissue will remain after flap creation and laser ablation also minimizes the risk of ectasia [57]. A thin RSB is one of the most important factors contributing to biomechanical instability, as the flap left on site has a slight influence on the structural tensile strength of the cornea [58]. That is the importance of the percent tissue altered (PTA) (this equation will be explained in topic 2.11) and how the precision of flap thickness is vital for adequate corneal biomechanical properties and a smooth stromal bed [57]. Corneas are more stable with thin uniform flaps compared to thicker flaps [54]. Furthermore, thinner flaps allow us to have more corneal tissue available for ablation, which may be crucial, especially when high refractive errors are intended to be corrected [47]. However, it is important to note that, a too thin corneal flap increases the incidence of flap related complications including a free, irregular, incomplete, buttonhole, or lacerated flap [51]. A thick corneal flap increases the likelihood of trespassing the minimum safe RSB thickness, typically considered to be 250 μm [51].

2.9. Excimer Laser

An excimer laser is a system that sculpts the cornea to correct refractive errors [59]. The excimer laser uses photoablation in the stroma [48], by disrupting the molecular bonds of the tissue, without any damage to adjacent tissues, consequently changing its shape and curvature, allowing the rays of light to focus with great precision on the retina [47,48].

The term "excimer" is derived from a contraction of "excited dimer" [44,59]. The excimer laser is based on the combination of two gases: a noble gas and a halogen, both of which are generally stable in their normal low-energy state [44,59]. Reactive gases, such as chlorine and fluorine, mixed with inert gases, such as argon, krypton and xenon, when electrically excited, emit energetic pulses of ultraviolet light, which can make very precise changes to irradiated material, such as polymers [59]. When a high-voltage electrical discharge is delivered into the laser cavity containing these gases, they combine to form a higher energy excited-gas state compound [59]. Upon dissociation of this high-energy compound, a photon is released with energy corresponding to the bond energy of the noble gas-halogen molecule [59]. This wavelength of light energy is amplified in the laser system, resulting

in the production of a discrete high energy pulse of laser energy [59]. The specific wavelength of an excimer laser depends on the composition of the gases used in the laser system [44,59], such as ArF (193 nm), KrF (248 nm), XeCl (308 nm), or XeF (351 nm) [44]. The process of ablative photodecomposition involves three main components: absorption, bond breaking, and ablation [44]. The ArF excimer laser at 193 nm is optimal for corneal absorption and ablation since it is very well absorbed by the proteins, glycosaminoglycans and nucleic acids comprising the cornea, because of its sufficient photon energy (6.4 eV) and precision (penetrating the superficial layer approximately 0.3 μm) [44,59]. Since 193 nm photon is of higher energy than the molecular bond strength of these compounds, absorption of the laser energy results in breaking of the bonds, removing tissue from the corneal surface, with tissue ablation depth correlating positively with the algorithm of laser density [59]. The laser energy is well absorbed near the corneal surface and, thus, should have few deep direct or secondary mechanical (shockwave) effects on the corneal tissue and minimal thermal damage to the surrounding tissue [59]. The ablation process is fast, and excess energy is ejected with the effluent plume. It has been shown that the 193 nm excimer laser is neither mutagenic nor carcinogenic [59].

Although excimer machines from different manufacturers converge in technology, individual lasers differ in laser ablation algorithm, eye-tracking technology, frequency of laser ablation, corneal thickness ablated, duration of treatment, and physical design [59].

The first-generation excimer lasers were “broad beam lasers” that created less uniform surface profiles than the newer generations [56,59]. These newer-generation excimer lasers use scanning beams or flying spots, with smaller spot sizes and more efficient eye trackers [56,59]. The availability of clinical aberrometer, and flying spot technology, led to the development of wavefront-guided ablation profiles, aiming not only at correcting defocus and astigmatism, but also some of the eye’s high order aberrations [48].

The frequency of laser pulses varies from 10 to 1050 Hz depending on the laser model [59]. The higher the frequency, the faster the treatment, but the thermal effect is higher, so the cooling of the treated tissue is ensured by using different algorithms [59]. In the other hand, the shorter the pulses, the less influence of thermal effect is on the nearby tissues. Optimal laser frequency with the full beam is from 10 to 50 Hz, while with flying beam lasers it goes up to 1050 Hz, and the speed depends on the success of the algorithm for positioning consecutive pulse strikes [59].

The energy that the pulse is delivering varies from 10 to 250 mJ, also depending on the laser [59]. Every pulse with constant energy of radiation above minimal step precisely removes a certain amount of corneal tissue [47,59].

The degree of ablation goes from 0.25 to 0.6 μm by pulse hit and is standard for every laser, but many factors influence ablation degree [59]. The histological layer of the cornea has a different ablation degree (ablation of epithelium is faster than stromal ablation, while stromal ablation is 30% faster than Bowman’s membrane ablation) [59]. Scaring slows down the ablation, while dehydration of the tissue accelerates it [59]. Each laser unit uses a nomogram based on which it calculates the thickness of tissue that are removed for each dioptre we want to correct [47].

The accurate estimation of ablation depth is a crucial factor regarding safety because it determines the postoperative total corneal thickness and residual stromal bed [1]. In current practice, the only ablation

depth estimation accessible to the surgeon is the one predicted by the laser platform's software, when the treatment is programmed [1]. Therefore, the surgeon works with this predicted value as a reference ablation depth even though it is a prediction and not an actual measurement [1]. Underestimation of excimer laser ablation depth, error in measuring corneal thickness, and underestimation of flap thickness are recognized as possible causes for some iatrogenic ectasia cases [60]. Flap geometry, thickness, diameter, and hinge length are important characteristics that affect the biomechanical impact on the cornea [60]. Appropriate surgical planning and controlling such characteristics reduces the risk of ectasia. Possible mechanisms for post-LASIK ectasia are pre-existing corneal pathology primarily in the form of keratoconus or chronic biomechanical failure due to inadequate residual stroma bed [60].

2.10. Munnerlyn's Formula

The refractive outcomes are continually improving because of evolutions in laser technology and diagnostic devices [1]. Complex algorithms through advanced technology software create the refractive map of the cornea, programming the laser beam for which abnormalities it will correct, and saving corneal tissue [47]. It is very important in refractive surgery to calculate the ablation thickness preoperatively in order to safely decide whether or not to operate [47]. There are two ways to estimate ablation depth preoperatively: one is using the mathematical model of Munnerlyn's formula, and the other is provided from the software that each excimer laser uses for ablation [47,53,61].

The mathematical model of Munnerlyn's formula for myopic ablation, is shown in Figure 20, where the corneal power needs to be reduced [62]. The original radius of curvature is represented by R_1, and the new radius of curvature, after ablation, is designated as R_2. The centre of the curvature before ablation is denoted as B, and after ablation as A. The optical zone is given by OZ. The ablation depth, AD, at the optical axis is given by the difference between S_1 and S_2, where S_1 is the sagittal depth of the preoperative cornea and S_2 is the sagittal depth of the postoperative cornea, i.e., $AD=S_1-S_2$.

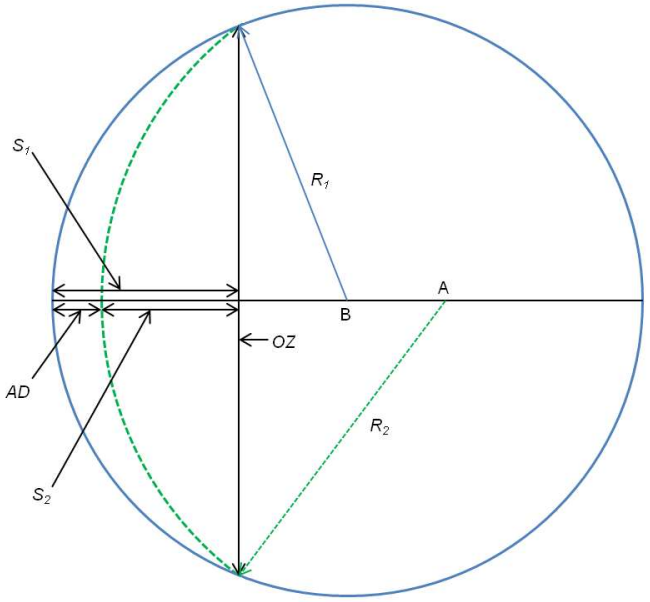

Figure 20 - Geometric representation of refractive correction for myopic ablation.

In Figure 20 we can see a triangle, where the hypotenuse is R_1 and the catheti are $\frac{OZ}{2}$ and $(R_1\text{-}S_1)$. Using Pythagorean Theorem we will get:

$$R_1^2 = (R_1 - S_1)^2 + \left(\frac{OZ}{2}\right)^2 \ (=)\ S_1 = R_1 - \sqrt{R_1^2 - \left(\frac{OZ}{2}\right)^2}.$$

The same theorem applies for R_2, as the hypotenuse, and $\frac{OZ}{2}$ and $(R_2\text{-}S_2)$, as the catheti. Thus, we may write:

$$R_2^2 = (R_2 - S_2)^2 + \left(\frac{OZ}{2}\right)^2 \ (=)\ S_2 = R_2 - \sqrt{R_2^2 - \left(\frac{OZ}{2}\right)^2}.$$

It is important to know that before the ablation, the refraction is assumed to be D dioptres and after the ablation, the refractive error is expected to be zero [62]. The amount of correction produced by the ablation in dioptres is [53,62]:

$$\mathrm{D} = (n-1)\left(\frac{1}{R_2} - \frac{1}{R_1}\right),$$

where n is the refractive index of the cornea. Since R_2 is larger than R_1 for myopic eyes, D becomes negative, which is representative of myopic power [62]. Solving the previous equation for R_2, we will get:

$$\frac{D}{(n-1)} = \left(\frac{1}{R_2} - \frac{1}{R_1}\right) \ (=)\ R_2 = \frac{(n-1)\times R_1}{D\times R_1 + \ (n-1)}.$$

As mentioned before, the ablation depth (AD) is given by the difference between S_1 and S_2:

$$AD = S_1 - S_2 \ (=)\ AD = R_1 - \sqrt{R_1^2 - \left(\frac{OZ}{2}\right)^2} - \left[R_2 - \sqrt{R_2^2 - \left(\frac{OZ}{2}\right)^2}\right].$$

Replacing R_2 by the expression obtained previously, we get the exact Munnerlyn's formula, which depends on three variables: the optical zone (OZ), the correction in dioptres (D) and the initial radius of curvature of the cornea (R_1) [47,53,62]:

$$AD = R_1 - \sqrt{R_1^2 - \left(\frac{OZ}{2}\right)^2} - \frac{(n-1)\times R_1}{D\times R_1 + \ (n-1)} + \sqrt{\left(\frac{(n-1)\times R_1}{D\times R_1 + \ (n-1)}\right)^2 - \left(\frac{OZ}{2}\right)^2}$$

$$AD = R_1 - \frac{R_1 \times (n-1)}{n-1+R_1 \times D} - R_1 \times \sqrt{\left(1 - \frac{OZ^2}{4 \times R_1^2}\right)} + \frac{R_1 \times (n-1)}{n-1+R_1 \times D} \times \sqrt{\left[1 - \frac{OZ^2}{4 \times R_1^2} \times \left(\frac{n-1+R_1 \times D}{(n-1)}\right)^2\right]}.$$

This formula may be simplified by taking into account that the optical zone is normally much smaller than the corneal radius, $\frac{OZ}{R_1} \ll 1$ [53]. Both square root terms from the previous equation can be approximated and expressed using Taylor's expansion formula [53]. If we consider

$$\mathrm{f}(x) = \sqrt{1-x},$$

then we may write, for small values of x, the approximation:

$$\mathrm{f}(x) \approx \mathrm{f}(0) + \mathrm{f}'(0)x,$$

where,

$$\mathrm{f}(0) = 1 \text{ and } \mathrm{f}'(0) = -\frac{1}{2}.$$

Ergo,

$$\mathrm{f}(x) \approx 1 - \frac{1}{2}x.$$

Using

$$x = \frac{OZ^2}{4 \times R_1^2},$$

the first square root term can be approximated by:

$$\sqrt{\left(1 - \frac{OZ^2}{4 \times R_1^2}\right)} = \sqrt{1-x} = \mathrm{f}(x)$$

$$\mathrm{f}(x) \approx 1 - \frac{1}{2} \times \frac{OZ^2}{4 \times R_1^2} = 1 - \frac{OZ^2}{8 \times R_1^2}.$$

Using

$$x = \frac{OZ^2}{4 \times R_1^2} \times \left(\frac{n-1+R_1 \times D}{(n-1)}\right)^2,$$

the second square root term can be approximated by:

$$\sqrt{\left[1 - \frac{OZ^2}{4 \times R_1^2} \times \left(\frac{n-1+R_1 \times D}{(n-1)}\right)^2\right]} = \sqrt{1-x} = \mathrm{f}(x)$$

$$\mathrm{f}(x) \approx 1 - \frac{1}{2} \times \frac{OZ^2}{4 \times R_1^2} \times \left(\frac{n-1+R_1 \times D}{(n-1)}\right)^2 = 1 - \frac{OZ^2}{8 \times R_1^2} \times \left(\frac{n-1+\mathrm{R}_1 \times D}{(n-1)}\right)^2.$$

Replacing these two expressions in the previous formula for the ablation depth, we obtain [62]:

$$AD \approx R_1 - \frac{R_1 \times (n-1)}{n-1+R_1 \times D} - R_1\left[1 - \frac{OZ^2}{8 \times R_1^2}\right] + \frac{R_1 \times (n-1)}{n-1+R_1 \times D} \times \left[1 - \frac{OZ^2}{8 \times R_1^2} \times \left(\frac{n-1+R_1 \times D}{(n-1)}\right)^2\right] =$$

$$= \frac{OZ^2}{8 \times R_1} + \left[-\frac{OZ^2}{8 \times R_1^2} \times \frac{R_1 \times (n-1)}{n-1+R_1 \times D} \times \left(\frac{n-1+R_1 \times D}{(n-1)}\right) \times \left(\frac{n-1+R_1 \times D}{(n-1)}\right)\right] =$$

$$= \frac{OZ^2}{8 \times R_1} + \left[-\frac{OZ^2}{8 \times R_1} \times \left(\frac{n-1+R_1 \times D}{(n-1)}\right)\right] = \left(\frac{OZ^2 \times (n-1) - OZ^2 \times (n-1) - OZ^2 \times R_1 \times D)}{8 \times R_1 \times (n-1)}\right) =$$

$$= -\frac{OZ^2 \times D}{8 \times (n-1)}.$$

If we considered $n = 1.376$ [53] the denominator may be replaced by $8 \times (1.376\text{-}1) = 3.008 \approx 3$. The Munnerlyn's formula, obtained by using these simplifications, states that the theoretical ablation thickness depth used clinically is based on two variables, the dioptres we want to correct (D) and the optical zone that we will use (OZ) [47,48,53]:

$$AD \approx \frac{OZ^2}{3} \times D.$$

If D is in dioptres and OZ in millimetres, the ablation depth will be in micrometres. The ablation algorithm is applied in the cornea, more specifically, in the optical zone, with less ablation depth being required in smaller optical zones for the same attempted correction [48]. However, small optical zones can severely compromise vision if they are smaller than pupil diameter [48]. A transition zone around the optical zone is created to avoid an abrupt step between treated and untreated areas [48].

Because of the approximations, the exact ablation depth is always larger than the ablation depth predicted by the Munnerlyn's approximated formula [53]. It is difficult to directly compare the two formulas because the exact formula depends on three variables, while the approximated formula depends on only two variables, the dioptres and optical zone [53]. It is immediately obvious from the Munnerlyn's approximated formula that ablation depth increases as the square of the optical zone size, an important clinical relationship that is not apparent in the exact formula [53]. The Munnerlyn's approximated formula is extremely accurate for small optical zones, however, for larger optical zones and dioptres, the approximated formula underestimates the ablation depth [53]. The advantage of the Munnerlyn's approximated formula is that it is so simple that it can be estimated mentally and used to check the results of any calculation [53]. An accurate estimation of ablation depth is most critical in patients with large optical zones and large corrections since there is a greatest risk for postoperative ectasia [53].

2.11. Percentage Tissue Altered (PTA)

Corneal ectasia is one of the most feared complications following corneal refractive surgery as it can result in an irreversible loss of visual acuity [4,49,63]. It is important to know that corneal ectasia after LASIK is a rare, yet potentially devastating complication characterized by progressive corneal thinning and bulging, which may lead to significant visual loss [3,4] and consequently, may eventually require corneal transplantation for visual rehabilitation [5]. Post-LASIK ectasia is characterized by a progressive increase in myopia, with or without increasing astigmatism, with steepening of the cornea and topographic asymmetric with inferior corneal steepening [4,63]. Corneal ectasia after LASIK occurs when the biomechanical integrity of the cornea is compromised with tissue alteration beyond a safe threshold required to maintain its shape and curvature [3,49,64]. This can happen in three different scenarios: when a cornea that is already prone to develop ectasia is subjected to surgery; when a weaker but clinically stable cornea is subjected to surgery; or when a relatively normal cornea is weakened by surgery, exceeding a safety threshold [3,64]. It is very important to determine preoperative risk factors before LASIK, since refractive surgery decreases collagen tension, by disrupting cornea biomechanics [63]. One of the reasons for corneal ectasia is a weakened residual stromal bed due to loss of a significant amount of stromal tissue in case of correction of high refractive errors or it may also be due to producing a thicker flap than planned [63]. This problem can be minimized or avoided by maintaining a *RSB* of at least 250 μm [47,53]. Residual stromal bed is calculated by subtracting flap thickness and ablation depth from the central corneal pachymetry [47,53,57]:

$$RSB = \textit{thickness before LASIK} - (\textit{flap thickness} + \textit{ablation thickness})$$

There is a relationship between preoperative corneal thickness, flap thickness and ablation depth, which determines the biomechanical changes after LASIK [3,49,64]. The *PTA* metric, representing the percentage of anterior corneal tissue that is modified during refractive surgery, has been described as an independent indicator of the risk of developing corneal ectasia in patients undergoing LASIK [49]. *PTA* is a better parameter to describe the postoperative effects on the cornea since it is a more accurate measure of the risk of ectasia than any of its components [3,64] and it has a higher correlation that other factors already established in the literature, such as RSB [3]. *PTA* is defined from the following equation [3,47,49,58,64,65]:

$$PTA = \frac{(FT + AD)}{CCT},$$

where FT corresponds to flap thickness, *AD* to ablation depth and *CCT* to central corneal thickness. Among patients with normal preoperative corneal topographies, a *PTA* above 40% was identified as the single, most significant independent indicator for predicting the development of corneal ectasia [3,47,49,58]. *PTA* does have some limitations, as the accurate estimation of *PTA* depends on the real thickness of the created flap [49]. Even when thin flaps are planned, thicker flaps may be created,

resulting in an increased risk of post-LASIK corneal ectasia [49]. Such variation in flap thickness may explain some cases of low-risk patients who develop post-LASIK corneal ectasia [49]. Once more, it is important to know the accuracy of flap thickness, pachymetry, as well as ablation depth, so that we can precisely calculate *PTA*.

After this theoretical framework, this thesis aims to investigate the accuracy and reliability of various clinical parameters, such as: real ablation depth and its different ways of prediction; flap thickness programmed during the surgery; and pachymetry measurements with three different devices.

3. Methodology

3.1. Study Design

We undertook an ambispective study, tracing patients that were already treated in the past and patients that have been treated during the period of our study with FS-LASIK for myopia or myopic astigmatism. We considered this refractive error, since the laser treatment focuses on the central cornea in myopia, flattening it and producing in the centre a deeper ablation than in periphery [48].

Our main purpose was to compare the laser platform of Technolas TENEO 317 (Bausch & Lomb) estimation of central ablation depth with the ablation depth that was manually calculated using optical low-coherence interferometry AS-OCT Visante device, and to compare these values with the exact Munnerlyn's formula and the approximated formula. This calculation regarded the difference between the measurements of pachymetry (in the central cornea) in preoperative and third month postoperative examination. Also, we compared the measurements between Orbscan and Pentacam, both with AS-OCT Visante, from preoperative and postoperative acquisitions. Finally, we investigated the accuracy of the intended flap thickness, measuring it manually with the aid of the AS-OCT Visante flap tool, in the vertex of the cornea, and comparing it with the value programmed in the iFS Advanced IntraLase femtosecond laser (Johnson & Johnson Vision) during the surgery.

This study received approval from the Ethics Committee and Investigation Committee of Hospital da Luz Lisboa.

3.2. Preoperative Examination

The preoperative ocular examination was performed by the ophthalmologist, which includes manifest refraction, corrected distance visual acuity, slit-lamp biomicroscopy and fundus examination. Following this procedure, the orthoptist performed exams to check whether the patient is a candidate for refractive surgery. Topography (Pentacam and Orbscan), aberrometry (Zywave) and AS-OCT (Visante) were some of the mandatory exams. After a careful evaluation of the exams by the ophthalmologist, the parameters for the surgery were decided, including the type of laser treatment (Proscan or Zyoptix), optical zone, flap thickness and its diameter.

3.3. Surgical Procedure

A total of 86 eyes were evaluated from 45 surgeries. These surgeries were performed by eight different ophthalmologists. The surgical procedure was divided into two parts: the flap creation and the excimer laser ablation.

Flap creation was performed using iFS Advanced IntraLase femtosecond laser (Johnson & Johnson Vision). The flap thickness was programmed either as 110 µm or 120 µm, and the intended flap diameter between 8.20 mm and 9.35 mm. It is important to mention that this data was collected from surgeries performed by different surgeons, each having their own technique and experience. This may be a limitation and may have influenced some of our results.

Excimer laser ablation was performed with Technolas TENEO 317 (Bausch & Lomb). The treatment was chosen between Proscan and Zyoptix by the surgeon. The optical zone was programmed in a

range between 6.50 mm and 7.50 mm. The target (sph) programmed in this platform was zero dioptres, for all patients, and the estimated RSB was above 300 µm.

It is also important to know that there is a nomogram associated in these treatments, which is a laser manufacture property algorithm that estimates the ablation performed for each case. There is also a different nomogram for each treatment. Proscan treats 95% of the sphere and 100% of cylinder of the manifest refraction, and Zyoptix treats the sphere based on measured HOAs and 100% of cylinder measured in the PPR (predicted phoropter refraction) on the aberrometer. Both Munnerlyn's formulas were calculated using different spherical equivalent references according to each treatment: the refraction determined by the ophthalmologist for the Proscan; and the PPR refraction obtained on the aberrometer for the Zyoptix.

3.4. Postoperative Examination

Visits for ocular examination performed by the ophthalmologist were scheduled for the day after the surgery, one week, one month and three months after the procedure. In the third month visit, the orthoptist repeated the acquisition in Orbscan, Pentacam and AS-OCT (Visante) to measure the pachymetry.

3.5. Devices Measurements

Measurements taken from preoperative and postoperative in Orbscan, Pentacam and Visante were acquired by different orthoptists, but the same orthoptist acquired the exams from the same patient. At least two measurements in each eye were performed in each of the three devices. For all patients, only the best quality acquisitions for each eye, from each device were considered for the study. The pachymetry considered was at the central corneal thickness from Orbscan, Pentacam and Visante. Central corneal thickness is a fundamental pachymetric index that is the basis of identifying corneal thinning disorders [30], as it plays an important function in screening for keratoconus and preoperative evaluation in corneal refractive surgery [37,66].

All the acquisitions were taken according to each device's instructions. Regarding the pachymetry, in Orbscan and Pentacam, this measurement was automatically calculated using the devices' software. In Visante, it was measured using the standard flap tool that performed automatic detection of anterior and posterior corneal surfaces [66]. Whenever this detection was not precise, we corrected it manually, by adjusting the boundary lines.

3.6. Statistical Analysis

All data was collected directly from the devices (Visante, Orbscan, Pentacam, IntraLase and TENEO). The statistical analysis was performed using the statistical functions of Excel and IBM SPSS Statistics 27 version.

In all subchapters, ablation depth accuracy, flap thickness accuracy and devices comparison, our statistical analysis started with the representation of each sample distribution, and the calculation of its minimum, mean, maximum and standard deviation (SD). Then, we compared the distributions

obtained by different methodologies: the real ablation depth, measured through Visante, with the excimer simulations, the approximated and the exact Munnerlyn's formulas; the flap measurements evaluated using Visante with its expected surgery value; and pachymetry measurements from Visante with Orbscan and Pentacam.

Since statistical comparison test usage depends on whether the underlying data is normally distributed or not, we proceeded to implement normality tests – Kolmogorov-Smirnov's ($n \geq 50$) or Shapiro-Wilk's ($n < 50$). Any significant result from these tests indicates that the tested sample follows a non-normal distribution, while normally distributed samples will be identified whenever these tests return non-significant results. After determining sample normality, the adequate statistical test was applied according to the hypotheses under study. For comparisons of means between two groups we used independent samples t-test or Mann-Whitney's test for normally or non-normally distributed samples, respectively. With these, the starting null hypothesis, H_0, was that both groups had identical means, while the alternative hypothesis, H_A, stated that the means of the two groups were not equal. A test that results in a p-value lower than alpha (0.05) is significant and indicates that we reject the null hypothesis, suggesting that the groups are different. For comparisons of means of one group to an expected or reference value, we used one-sample t-test or its non-parametric equivalent for normally or non-normally distributed samples, respectively. With these, the starting null hypothesis, H_0, was that the group mean was not different from the expected value, while the alternative hypothesis, H_A, stated that the mean of the group was not equal to the reference value. A test that results in a p-value lower than alpha (0.05) is significant and indicates that we reject the null hypothesis, suggesting that the group mean is different from expected. In all cases where we performed two or more comparisons simultaneously, we have applied Bonferroni's correction. As multiple comparisons are performed, the likelihood of incurring a type I error (false positive) increases. Bonferroni's correction is one of several statistical corrections that can be used to combat this effect, and works by multiplying the obtained raw p-values by the number of pairwise comparisons being made. By increasing the p-value against the same value of alpha, the test becomes more stringent, and we are less likely to incorrectly reject the null hypothesis. While p-value-based statistical tests tells us whether there are differences between groups, it does not tell us the strength of those differences. To provide an additional description of group differences, we calculated the effect size between pairwise groups, expressed as Cohen's d – where we divided the means' difference by the standard deviation. Using the thresholds set by statistical convention, an obtained value of up to 0.2 indicates a small effect, a value between 0.2 and 0.5 represents a medium effect, a value between 0.5 and 0.8 is indicative of a large effect, and a value above 0.8 represents a very large effect.

To summarize, it should be noted that, in each case, the examined samples were not independent, and statistical comparisons had to be done with care. For instance, in what regards the ablation depth accuracy, each of the 86 eyes was evaluated in four categories: the real ablation depth (measured with Visante), the excimer simulation (laser platform), the approximated Munnerlyn's formula and the exact Munnerlyn's formula. Besides the standard statistical distribution comparison tests, we represented in a plot the dispersion distribution of all values, taking into account each ablation depth studied. We also represented the distribution of the differences between the measures in each

category with the real ablation depth. A careful examination of these figures, together with the calculation of the mean and its standard deviation from the difference's distribution, allowed us to obtain useful information about the associations between all the methodologies. A similar treatment has been made to study the flap thickness accuracy, where this parameter was compared with its expected value using Visante and also, the pachymetry from each of the 86 eyes was measured with three different pachymetry devices, Visante, Orbscan and Pentacam.

4. Results

Patients were aged between 18 and 54 years old, with no history of ocular disease or previous keratorefractive surgery. All patients underwent FS-LASIK and had myopia with or without astigmatism. We evaluated a total of 86 eyes from 45 patients, 28 of which were female (62.2%) and 17 were male (37.8%). Demographically, we can see in Figure 21 the distribution of the patient's gender by age range.

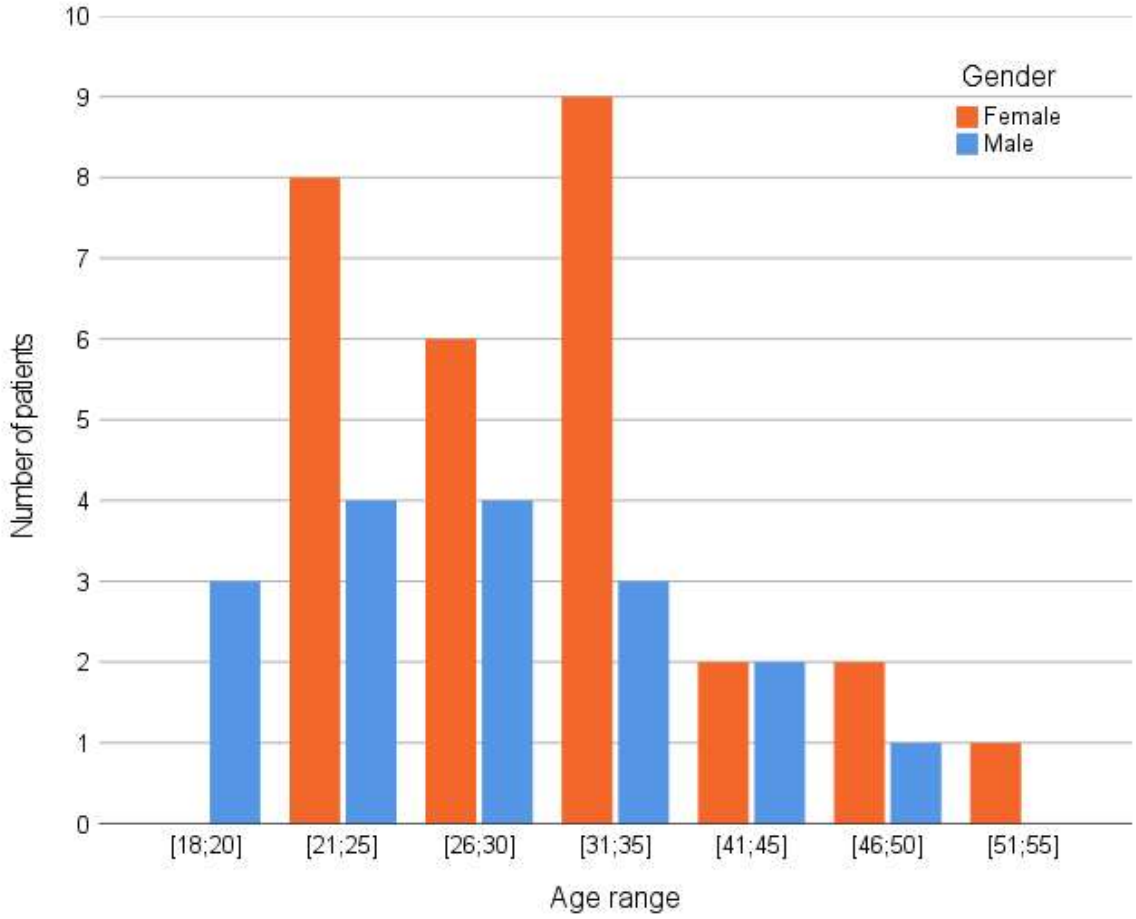

Figure 21 - Distribution of patient gender by age range.

4.1. Ablation depth accuracy

Accurate determination of ablation depth is an important factor in deciding patient eligibility for corneal surgery. For the ablation depth evaluation, we divided our population into two groups, considering the treatment each surgeon has decided for their candidates: Proscan with a total of 45 eyes, and Zyoptix with 41 treated eyes. For both treatments we compared values across the four categories in study: real ablation depth measured in Visante, ablation simulated by the excimer laser software, and values obtained with the approximated and exact Munnerlyn's formulas.

4.1.1 Proscan treatment

In Figure 22 to Figure 25, we can see the distribution for each of the four analysed categories. Descriptive statistics can be found in Table 1 and test of normality in Table 2 (both shown in Annexes).

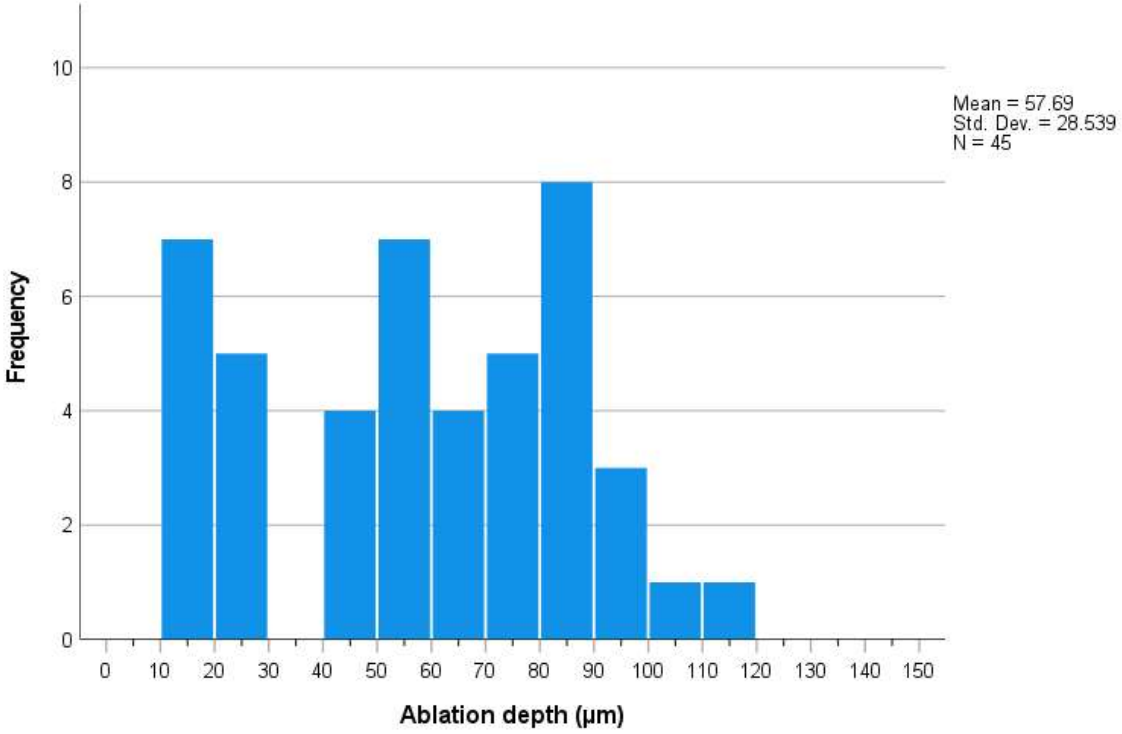

Figure 22 – Distribution of ablation depth for real measurements given by Visante.

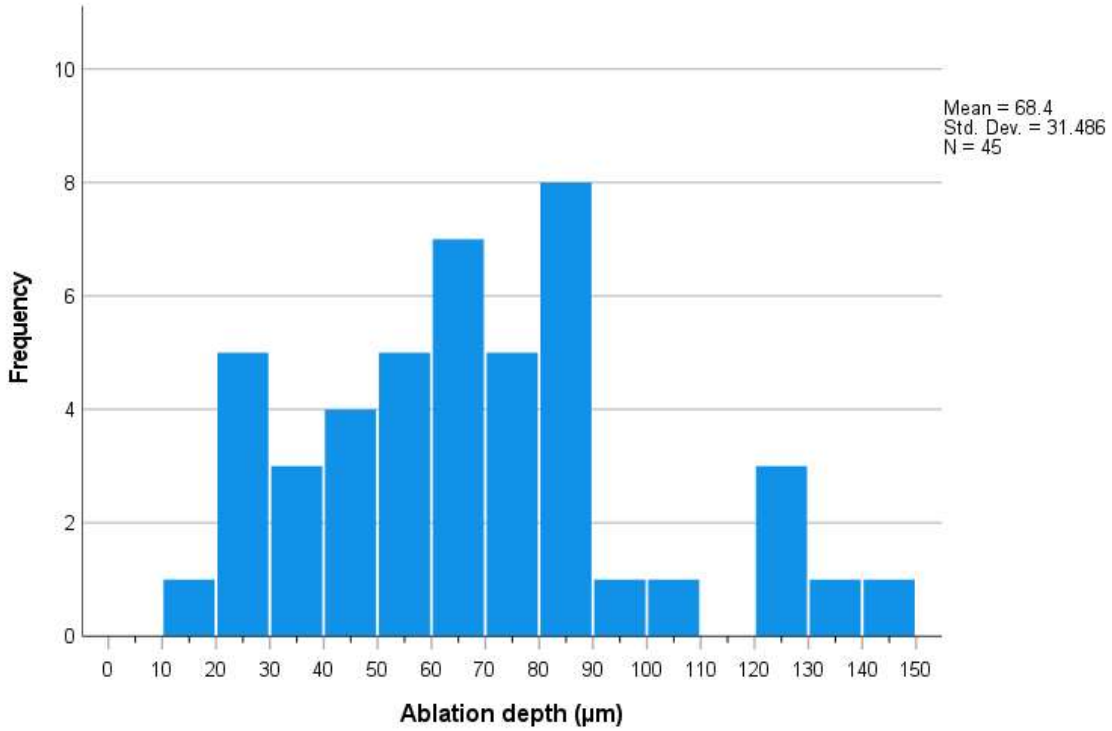

Figure 23 – Distribution of ablation depth for the excimer simulation.

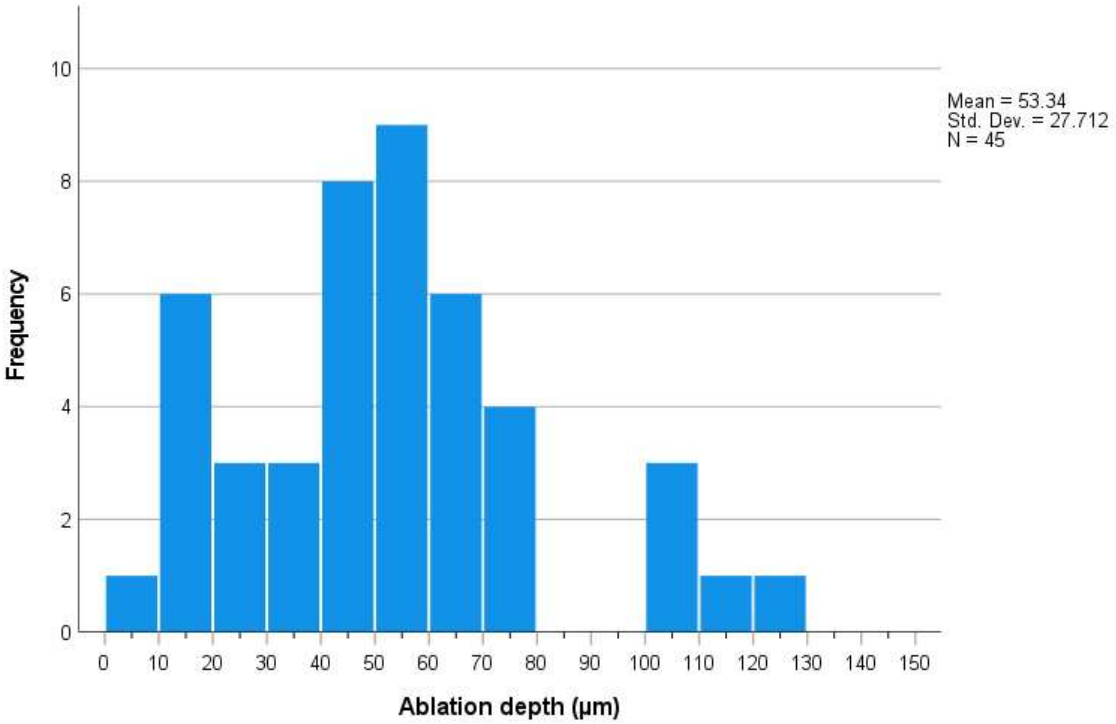

Figure 24 – Distribution of ablation depth for the approximated Munnerlyn's formula.

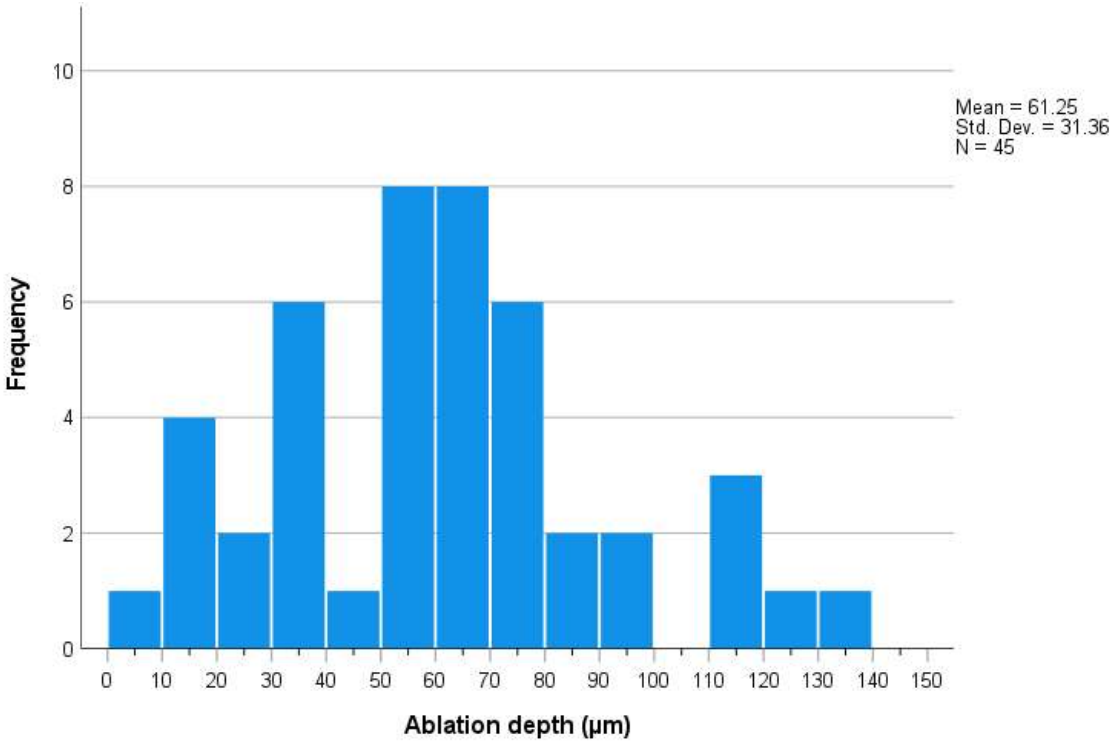

Figure 25 – Distribution of ablation depth for the exact Munnerlyn's formula.

We wanted to compare the measurements acquired from Visante (real ablation depth) with the simulated values from the laser excimer software, to know how reliable these simulations were, and also to compare them with both Munnerlyn's formulas, approximated and exact, to see if the surgeon can still rely on them.

In Figure 26, we can see the dispersion of different ablation depths according to the four categories and conclude that there were no significant differences between the real measurements and any of the other three categories.

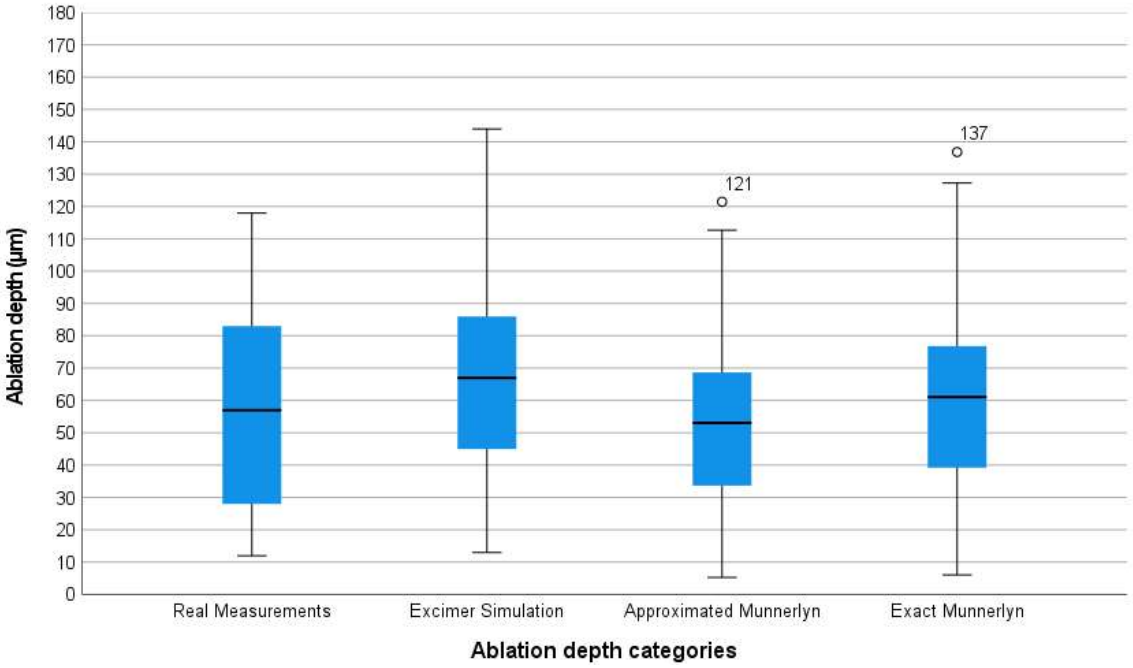

Figure 26 – Ablation depth values from the four categories.

Our null hypotheses stated that the mean ablation depth measurements from Visante were equal to the mean ablation depth from excimer simulation, or those derived from either Munnerlyn's formulas. The alternative hypotheses stated that there were differences between the mean ablation depth measurements from Visante and the mean ablation depth from each of the other three categories:

$$H_0: \mu_{\text{Real Ablation Depth}} = \mu_{\text{Excimer Simulation}}$$

$$H_A: \mu_{\text{Real Ablation Depth}} \neq \mu_{\text{Excimer Simulation}}$$

and,

$$H_0: \mu_{\text{Real Ablation Depth}} = \mu_{\text{Approximated Munnerlyn}}$$

$$H_A: \mu_{\text{Real Ablation Depth}} \neq \mu_{\text{Approximated Munnerlyn}}$$

and,

$$H_0: \mu_{\text{Real Ablation Depth}} = \mu_{\text{Exact Munnerlyn}}$$

$$H_A: \mu_{\text{Real Ablation Depth}} \neq \mu_{\text{Exact Munnerlyn}}$$

We can see that in all three categories the values were not statistically different from the real ablation depth measured in Visante (Bonferroni adjusted p-value of 0.28, 1.0 and 1.0, see Table 3, Table 4 and Table 5, respectively, in Annexes). This means that ablation depth from excimer simulation, approximated and exact Munnerlyn's formulas tended to not be statistically different from the real

ablation depth measured by Visante, with a relatively small effect, in all cases (Cohen's d of -0.356, 0.154 and -0.119, see Table 6, Table 7 and Table 8, respectively, in Annexes).

Despite the lack of statistical differences between categories, looking at Figure 27, to the dispersion of their ablation values, we see that excimer simulation had a slight tendency to overestimate the ablation depth, especially in extreme low and high values. Both approximated and exact Munnerlyn's formulas followed the same pattern, except between 60 µm and 90 µm where approximated Munnerlyn's formula tended to underestimate the ablation depth.

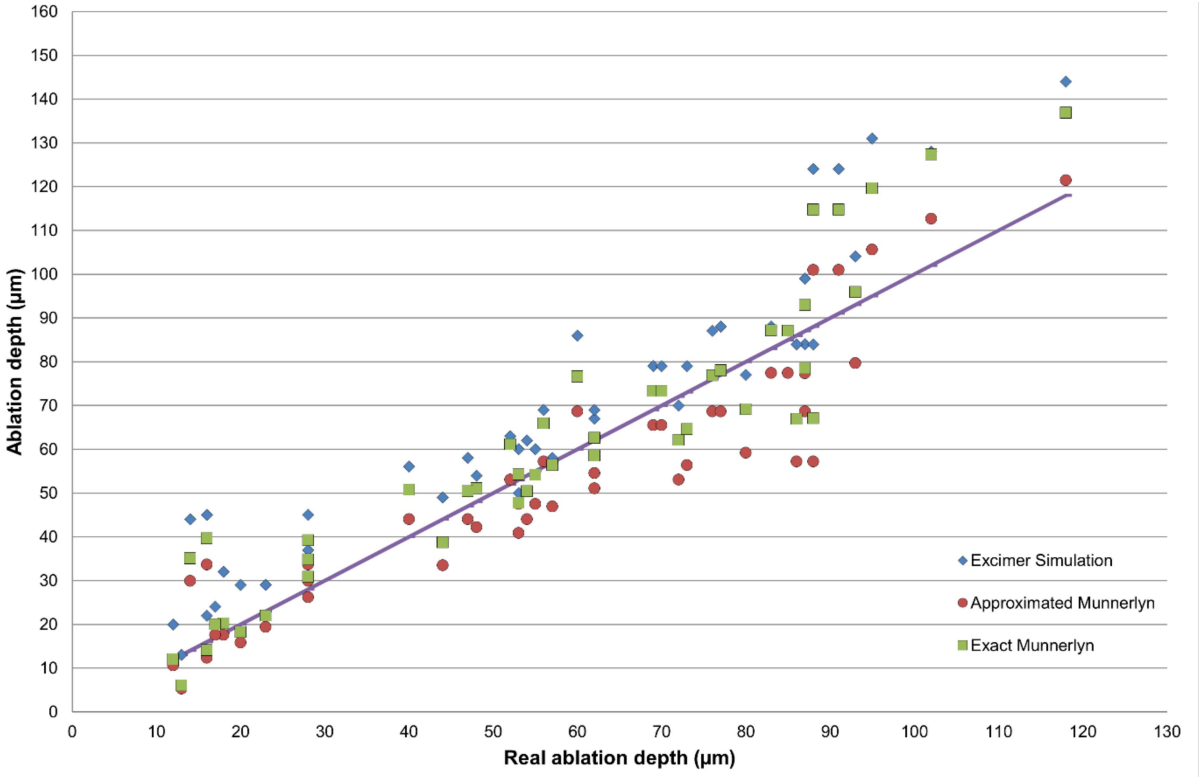

Figure 27 – Dispersion of ablation depth values. Blue diamonds represent the matching ablation depth between real ablation and excimer simulation; Red dots represent the matching ablation depth between real ablation and approximated Munnerlyn's formula; Green squares represent the matching ablation depth between real ablation and exact Munnerlyn's formula; Purple line corresponds to the real ablation depth, measured in Visante, which stands as reference.

In Figure 28, we present the differences between the real ablation depth, measured in Visante, with the values of the excimer simulation (Δexcimer), the approximated Munnerlyn's formula (Δapproximated) and exact Munnerlyn's formula (Δexact). It is noticeable that the average values of the different ablation categories were really close to each other (see Table 9). However, Δexcimer standed out as the one with the largest mean value of -10.7 µm. As for Δapproximated and Δexact, the mean values were 4.3 µm and -3.6 µm, respectively. Additionally, we calculated the SD of the differences between the real ablation depth and the various ablation categories, which gave us the accuracy of the excimer and Munnerlyn's formulas, according to the sample. The SD values of Δexcimer, Δapproximated and Δexact were ± 10.6 µm, ± 10.6 µm and ± 11.2 µm, respectively. Thus,

the results showed that the performance of the excimer and both formulas was similar to the real ablation depth.

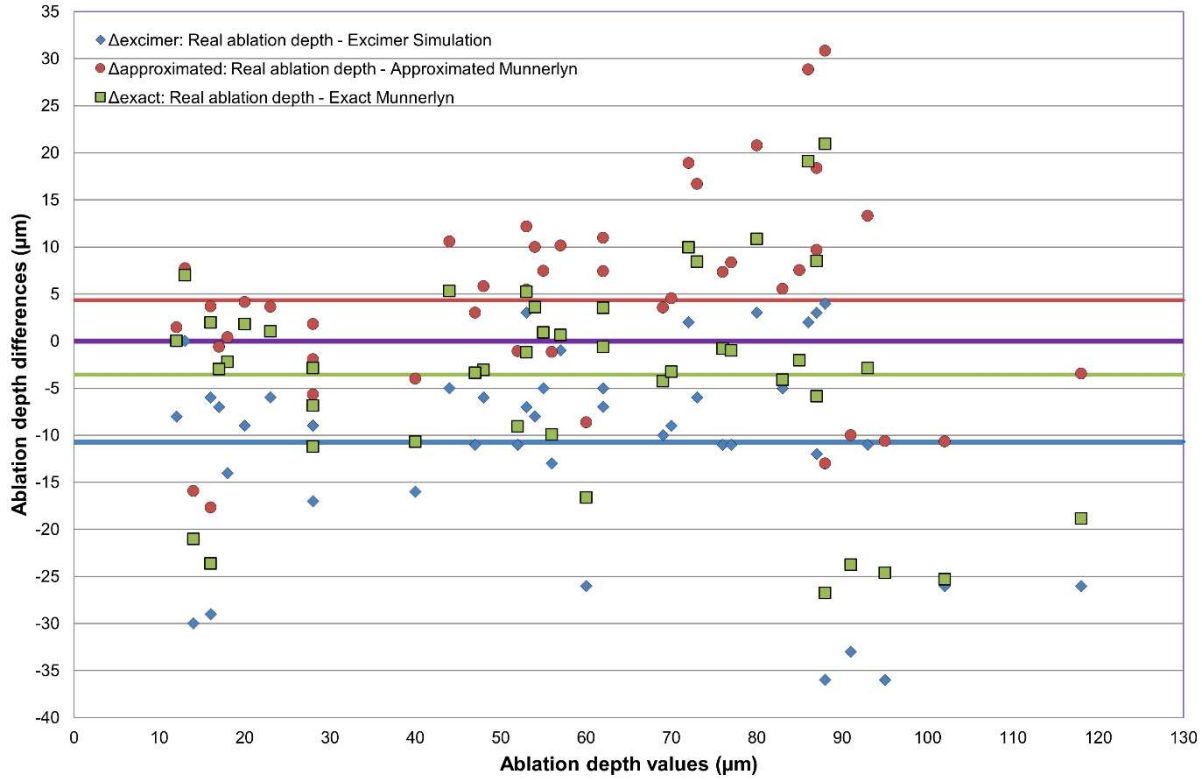

Figure 28 – Distribution of the differences in ablation depth values. Blue diamonds represent Δexcimer; Red dots represent Δapproximated; Green squares represent Δexact; Purple line follows the x-axis, and stands for the reference real ablation depth values, given by Visante. Blue line corresponds to the mean of Δexcimer (-10.7 µm); Red line corresponds to the mean of Δapproximated (4.3 µm); Green line corresponds to the mean of Δexact (-3.6 µm).

4.1.2 Zyoptix treatment

In Figure 29 to Figure 32, we can see the distribution for each of the four analysed categories. Descriptive statistics can be found in Table 10 and test of normality in Table 11 (both shown in Annexes).

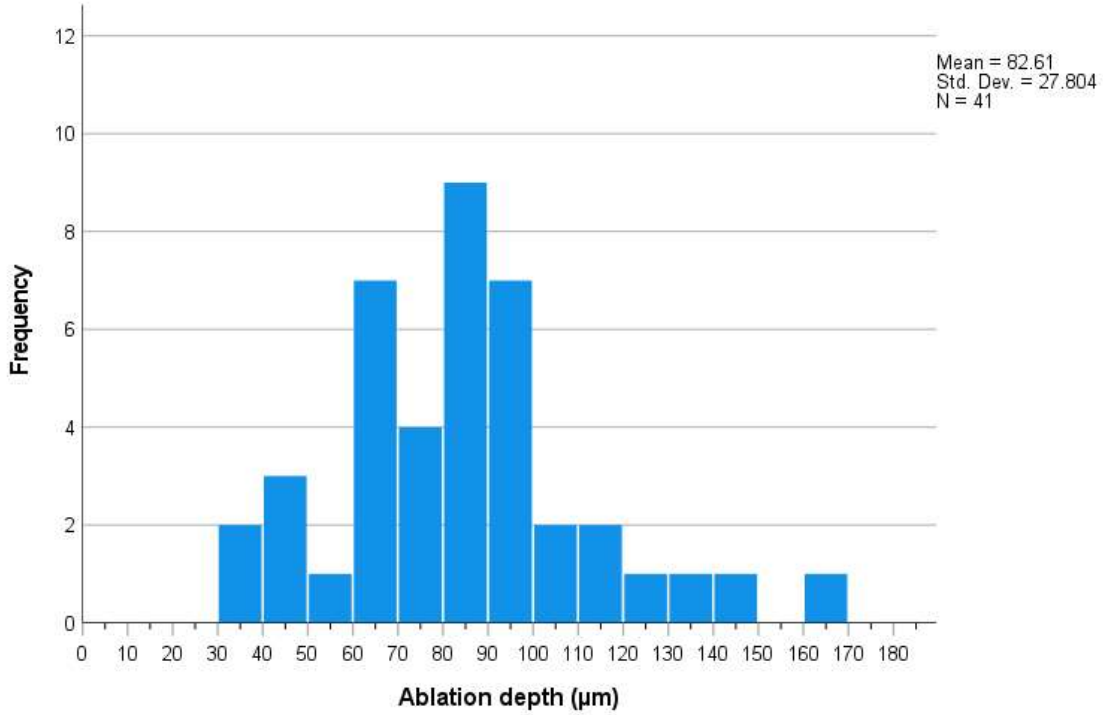

Figure 29 – Distribution of ablation depth for the real measurement.

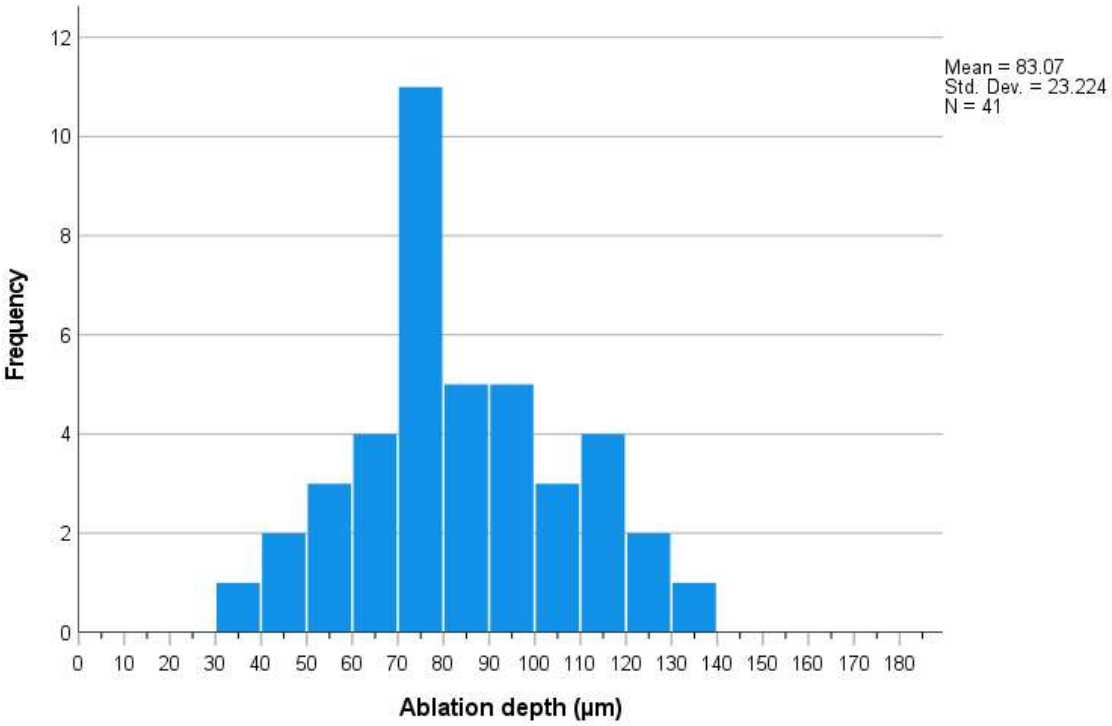

Figure 30 – Distribution of ablation depth for the excimer simulation.

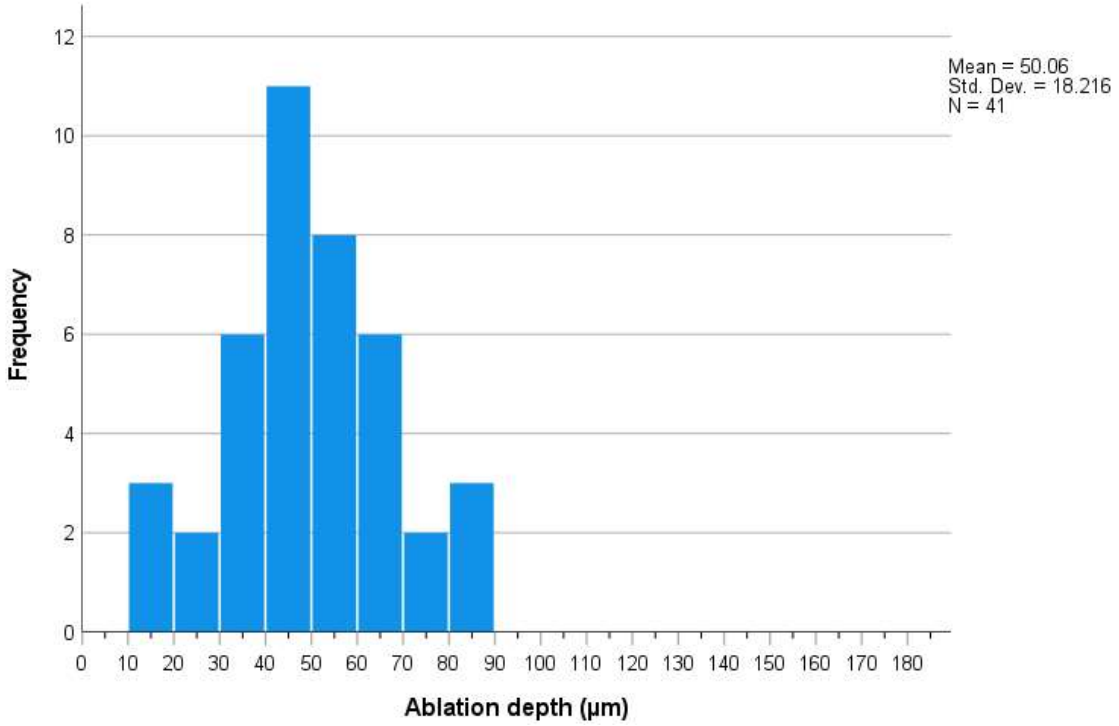

Figure 31 – Distribution of ablation depth for the approximated Munnerlyn's formula.

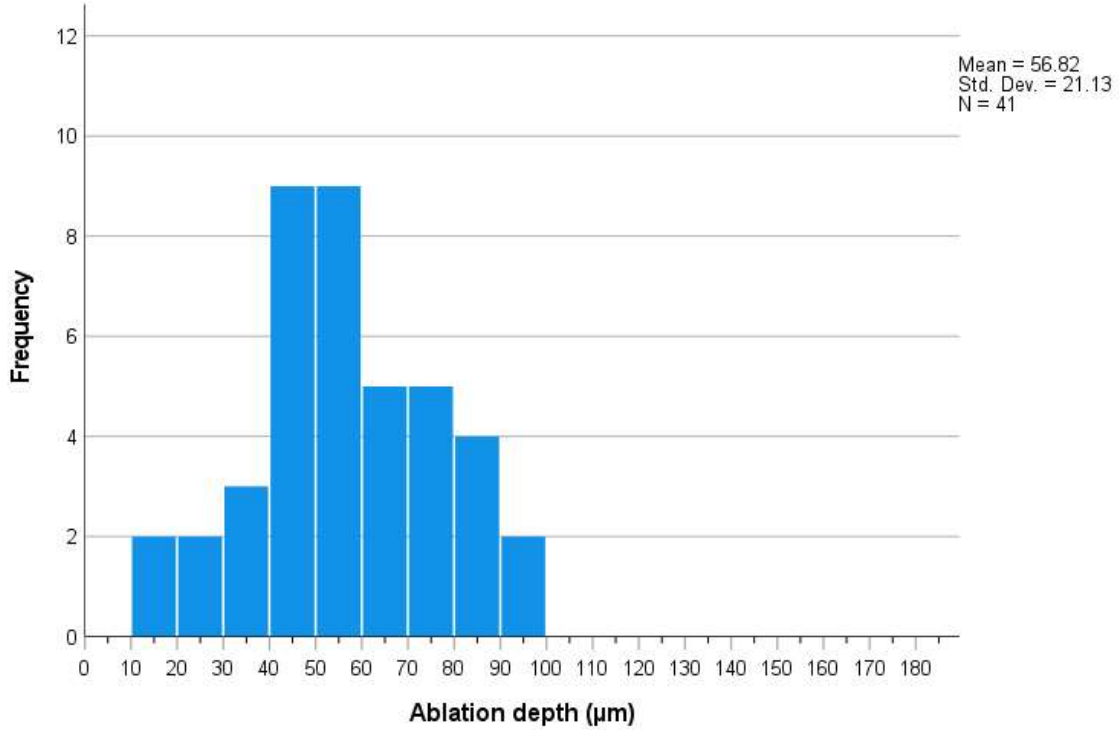

Figure 32 – Distribution of ablation depth for the exact Munnerlyn's formula.

Once again, we wanted to compare the measurement acquired from Visante (real ablation depth) with the simulated values from the laser excimer software, to know how reliable these simulations were, and we also wanted to compare with both Munnerlyn's formulas, approximated and exact, to see if the surgeon can still rely on them.

In Figure 33, we can see the dispersion of different ablation depth according to the four categories and conclude that both Munnerlyn's formulas predicted significantly lower ablation depth compared to the real measurements from Visante.

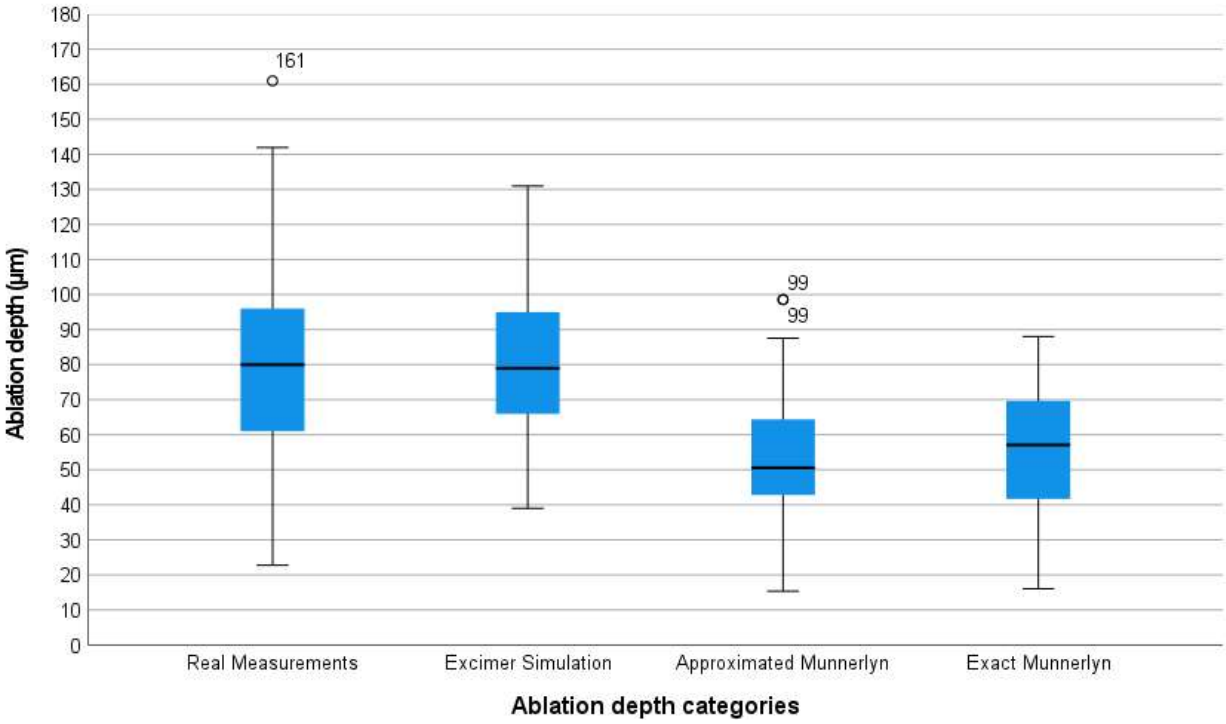

Figure 33 - Ablation depth values from the four categories.

Our null hypotheses stated that the mean ablation depth measurements from Visante were equal to the mean ablation depth from excimer simulation, or those derived from either Munnerlyn's formula. The alternative hypotheses stated that there were differences between the mean ablation depth measurements from Visante and the mean ablation depth from each of the other three categories:

$$H_0: \mu_{\text{Real Ablation Depth}} = \mu_{\text{Excimer Simulation}}$$

$$H_A: \mu_{\text{Real Ablation Depth}} \neq \mu_{\text{Excimer Simulation}}$$

and,

$$H_0: \mu_{\text{Real Ablation Depth}} = \mu_{\text{Approximated Munnerlyn}}$$

$$H_A: \mu_{\text{Real Ablation Depth}} \neq \mu_{\text{Approximated Munnerlyn}}$$

and,

$$H_0: \mu_{\text{Real Ablation Depth}} = \mu_{\text{Exact Munnerlyn}}$$

$$H_A: \mu_{\text{Real Ablation Depth}} \neq \mu_{\text{Exact Munnerlyn}}$$

We can see that the values were not statistically different between the real ablation depth measured in Visante and the excimer software (Bonferroni adjusted p-value of 1.0, see Table 12, in Annexes). Between the real ablation depth measurements and both Munnerlyn's formulas, the values were

statistically different (Bonferroni adjusted p-values of < 0.001 and < 0.001, see Table 13 and Table 14, respectively, in Annexes). This means that ablation depth from excimer simulation tended to be similar to the real ablation depth measured by Visante, with a small effect (Cohen's d of -0.058, see Table 15, in Annexes). On the contrary, both approximated and exact Munnerlyn's formulas tended to differ from the real ablation depth values, both with a large effect (Cohen's d of 1.069 and 0.928, see Table 16 and Table 17, respectively, in Annexes).

Looking at Figure 34, which represents the dispersion of the different ablation depth categories, we see that both Munnerlyn's formulas tended to underestimate the ablation depth values, and that these differences were more evident in ablation values above 110 µm.

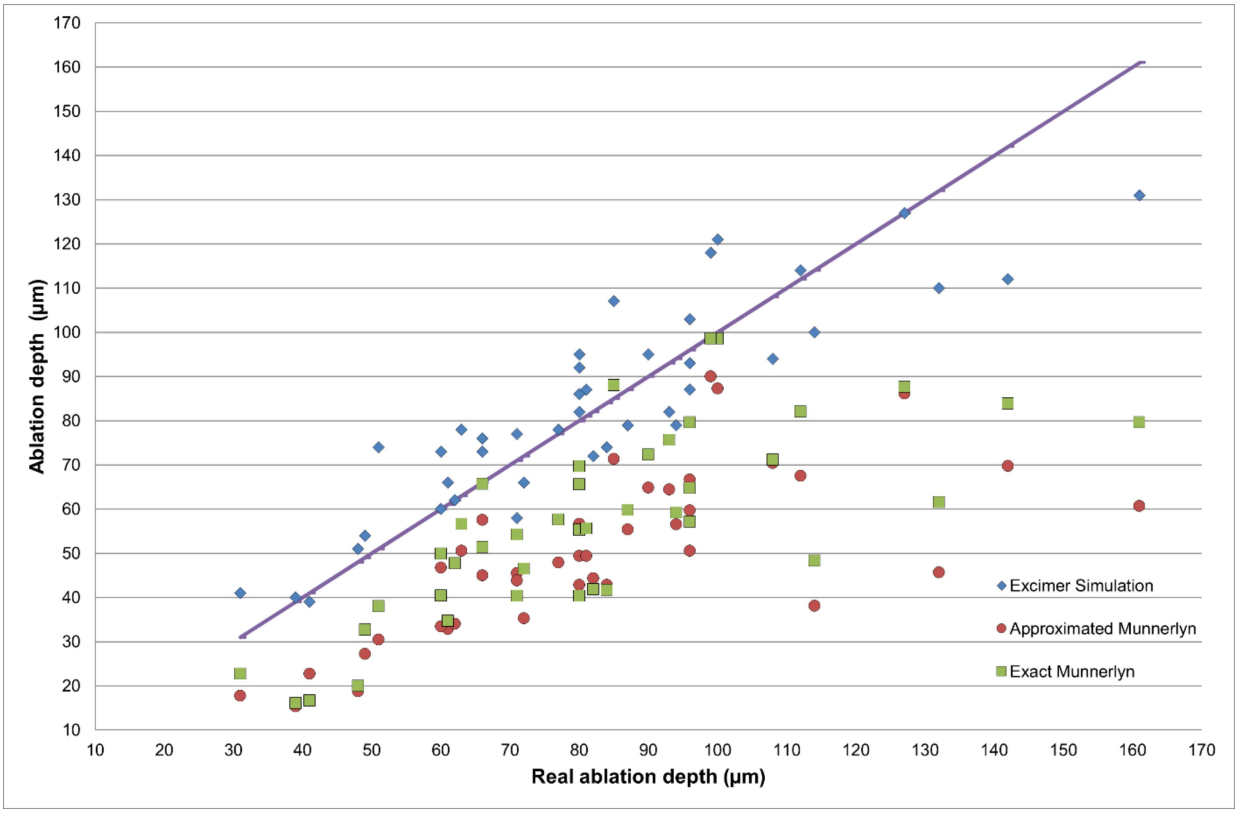

Figure 34 – Dispersion of ablation depth values. Blue diamonds represent the matching ablation depth between real ablation and excimer simulation; Red dots represent the matching ablation depth between real ablation and approximated Munnerlyn's formula; Green squares represent the matching ablation depth between real ablation and exact Munnerlyn's formula; Purple line corresponds to the real ablation depth, measured in Visante, which stands as reference.

In Figure 35, we present the differences between the real ablation depth, measured in Visante, with the values of the excimer simulation (Δexcimer), the approximated Munnerlyn's formula (Δapproximated) and exact Munnerlyn's formula (Δexact). It is noticeable that the average values of the different excimer simulations were really close to the real ablation depth, unlike both Munnerlyn's formulas which presented very distinct values (see Table 18). The Δexcimer standed out as the one with the smallest mean value of -0.5 µm. As for Δapproximated and Δexact, the mean values were 32.6 µm and 25.8 µm, respectively. We have also calculated the SD of the differences between the real ablation depth and the various ablation categories, which gave us the accuracy of the excimer

and Munnerlyn's formulas, according to the sample. The SD values for Δexcimer, Δapproximated and Δexact were ± 12.9 µm, ± 19.8 µm and ± 18.7 µm, respectively. Thus, the results showed that the performance of the excimer is quite similar to the real ablation depth, on the other hand, both Munnerlyn's formulas were not as accurate.

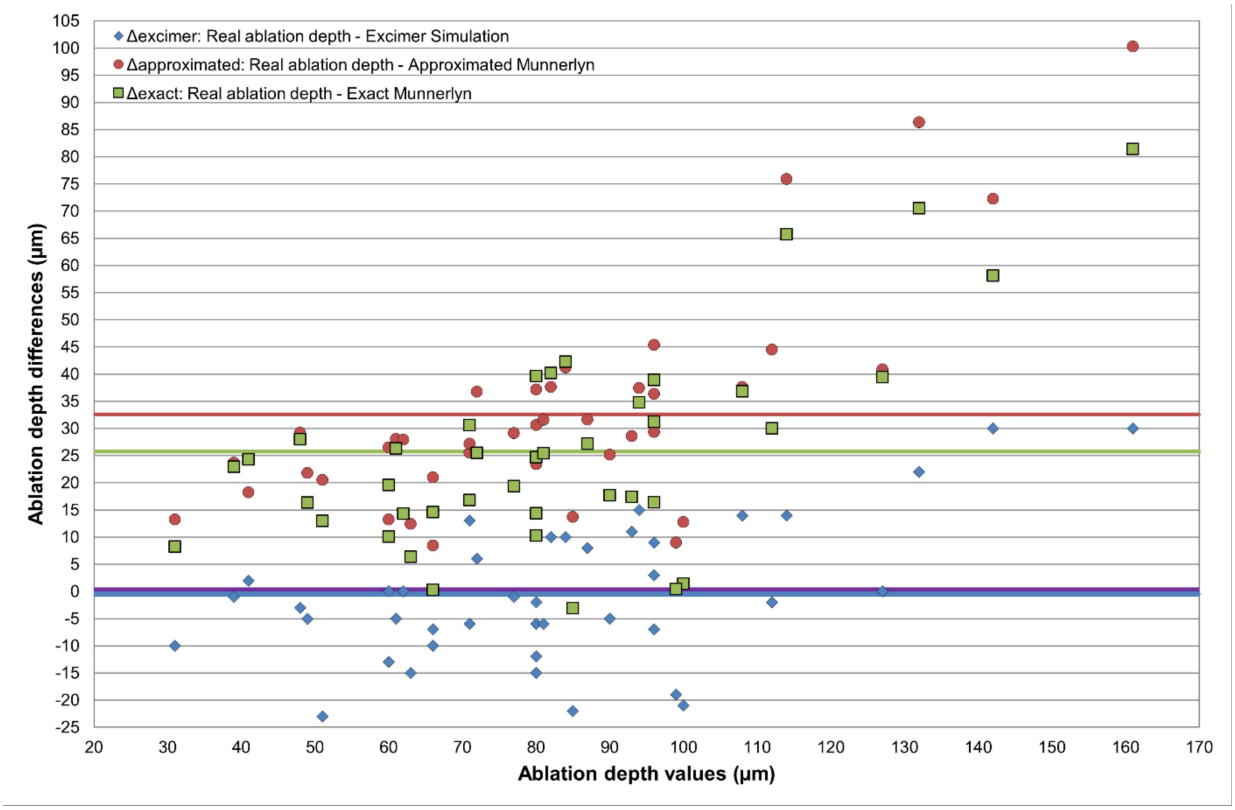

Figure 35 – Distribution of the differences in ablation depth values. Blue diamonds represent Δexcimer; Red dots represent Δapproximated; Green squares represent Δexact; Purple line follows the x-axis, and stands for the reference real ablation depth values, given by Visante. Blue line corresponds to the mean of the Δexcimer (-0.5 µm); Red line corresponds to the mean of the Δapproximated (32.5 µm); Green line corresponds to the mean of the Δexact (25.8 µm).

We can see that in Proscan treatment, all the categories were similar when compared with the real ablation depth, although excimer simulation tended to slightly overestimate it, especially in extreme ablation values conditions. In the case of the Zyoptix treatment, both formulas largely underestimated the ablation depth. Therefore, one should be cautious when using the Munnerlyn's formulas to guide ablation decision when performing a Zyoptix treatment.

4.2. Flap thickness accuracy

Measuring flap thickness with accuracy is important to safeguard residual bed stroma after flap creation and laser ablation. Thus, we wanted to compare the flap thickness measured with Visante acquisitions, with the expected values from iFS to know how accurate its performance actually was.

In Figure 36 and Figure 37 we can see the distribution of the measurements in Visante for 110 µm and 120 µm flap thickness, respectively. Descriptive statistics can be found in Table 19 and test of normality in Table 20 (both shown in Annexes).

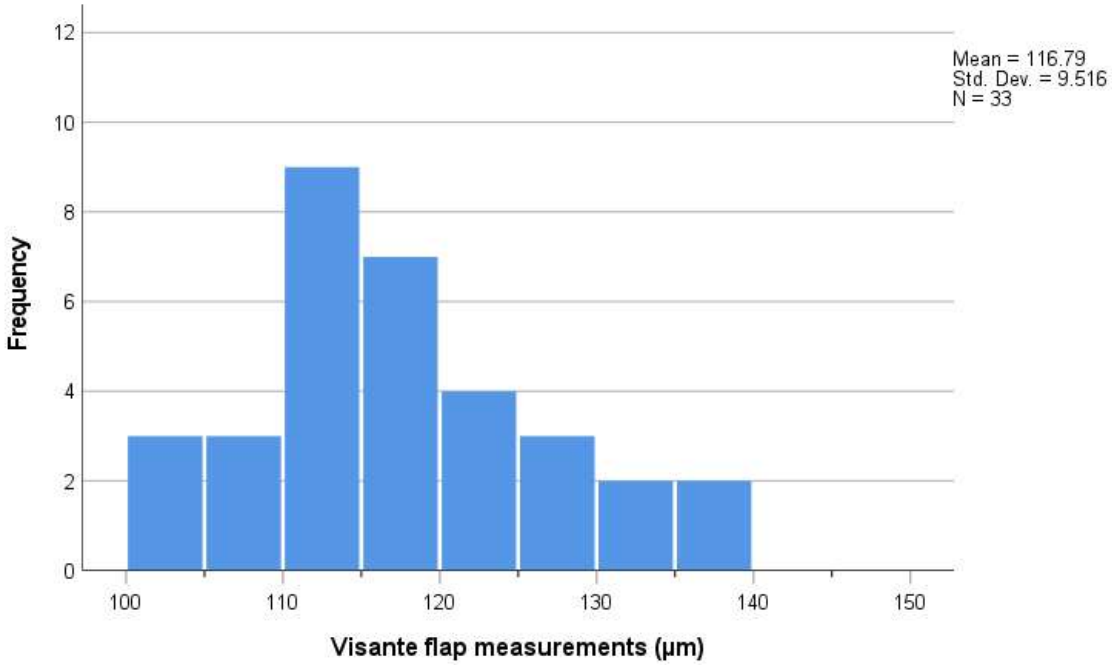

Figure 36 – Distribution of Visante flap measurements for 110 µm flap thickness.

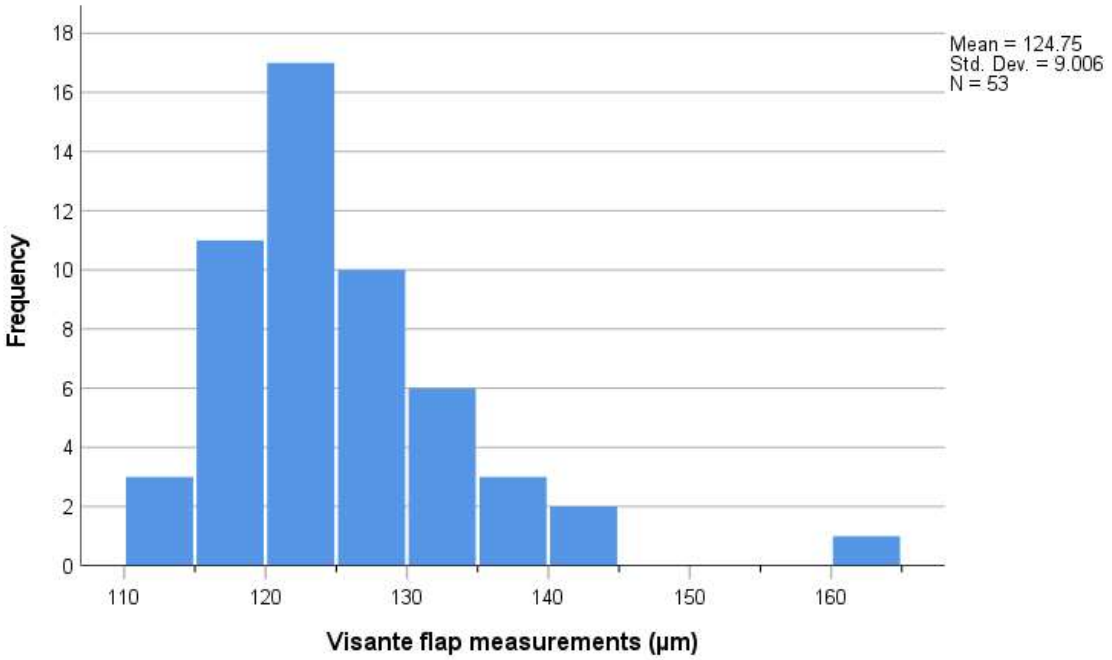

Figure 37 – Distribution of Visante flap measurements for 120 µm flap thickness.

In Figure 38 and Figure 39 we can see the dispersion of each flap thickness measured in Visante according to the iFS programmed parameter, with an horizontal line in purple standing for 110 µm and 120 µm thickness, respectively, as a reference. Of particular note, the median Visante measurements for flap thickness of 120 µm (Figure 38) was much closer to the expected value of 120 µm (median of 122 µm), than the one for 110 µm (median of 115 µm) (Figure 39). We can also see a moderate outlier in 110 µm flap programming, with a 139 µm value and a severe outlier in 120 µm flap programming, with 164 µm value.

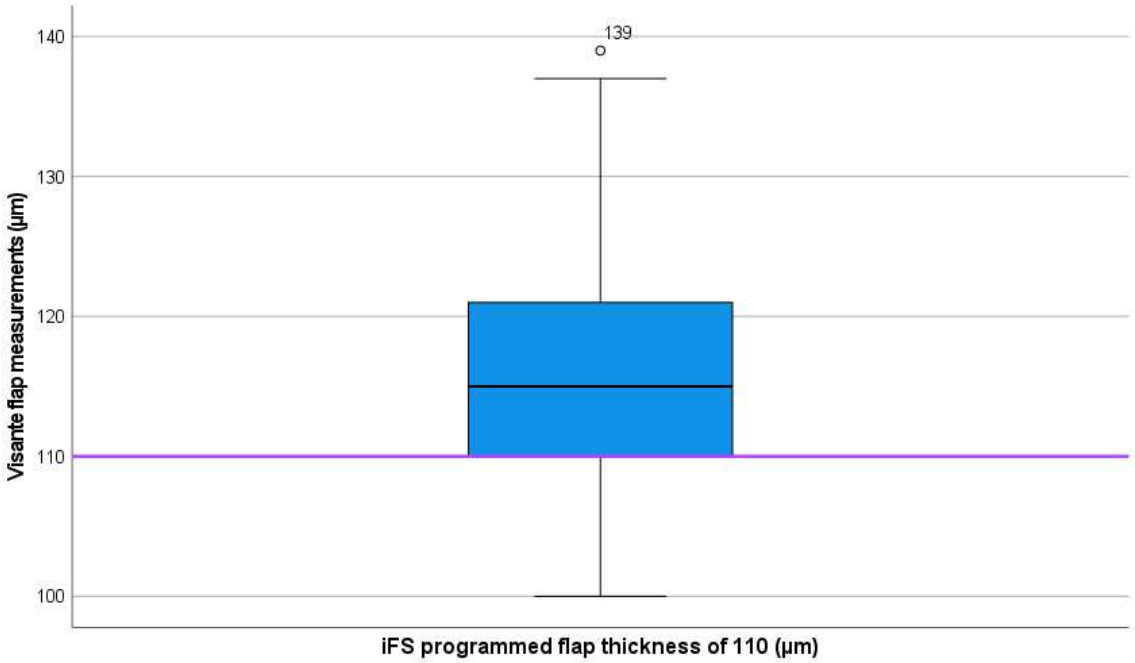

Figure 38 – Visante measurements for 110 µm flap thickness**.**

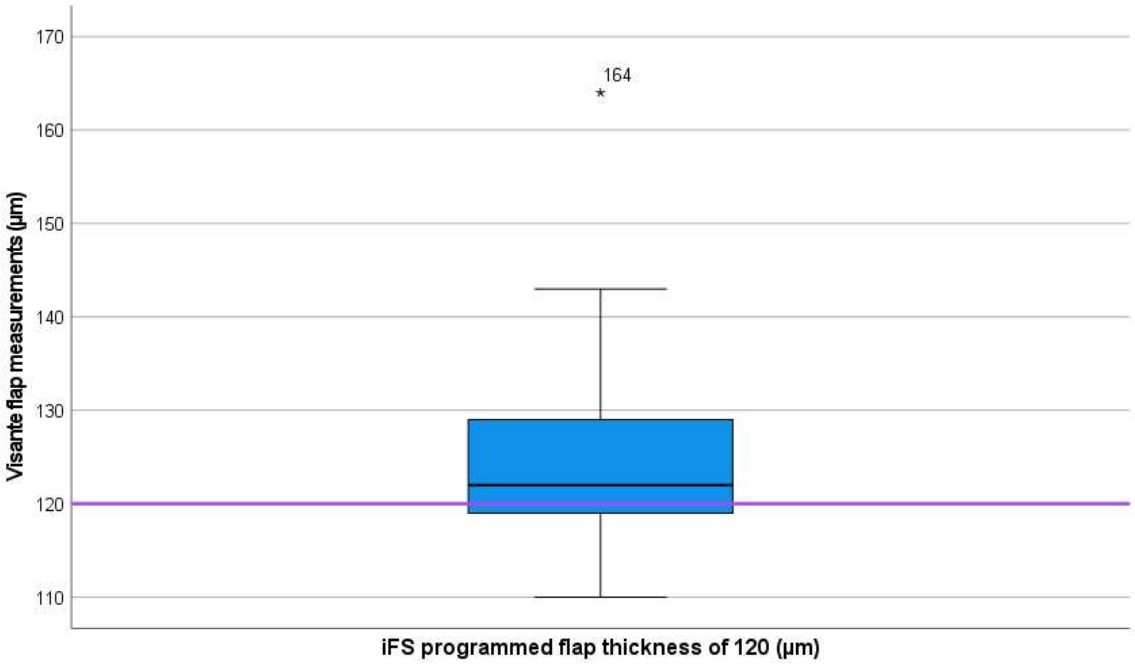

Figure 39 – Visante measurements for 120 µm flap thickness**.**

Our null hypotheses stated that the mean measurements taken from Visante were similar to the actual value programmed at the surgery (110 µm or 120 µm). The alternative hypotheses stated that the mean measurements taken from Visante were not equal to the value programmed at the surgery:

$$H_0: \mu_{\text{Visante measurements for 110 µm}} = \text{iFS flap value 110 µm}$$

$$H_A: \mu_{\text{Visante measurements for 110 µm}} \neq \text{iFS flap value 110 µm}$$

and,

$$H_0: \mu_{\text{Visante measurements for 120 µm}} = \text{iFS flap value 120 µm}$$

$$H_A: \mu_{\text{Visante measurements for 120 µm}} \neq \text{iFS flap value 120 µm}$$

In both cases, the documented Visante values were statistically different from the respective baseline expected values (p-value < 0.001 for 110 µm flaps and p-value of < 0.001 for 120 µm flaps, see Table 21 and Table 22, respectively, in Annexes). These statistical differences matched with a relatively medium effect in both cases (Cohen's d of 0.713 for 110 µm and 0.528 for 120 µm, see Table 23 and Table 24, respectively, in Annexes).

In Figure 40, we can see the measurements for both 110 µm and 120 µm flap thickness set during the surgery. Graphically, we can see that flap measurements mostly tented to be above the programmed value. Despite being statistically different, the 110 µm measurements (with a mean of 6.8 µm and a SD of ± 9.5 µm) were not as accurate as the 120 µm measurements (with a mean of 4.8 µm and a SD of ± 9.0 µm), which were slightly closer to its exact value.

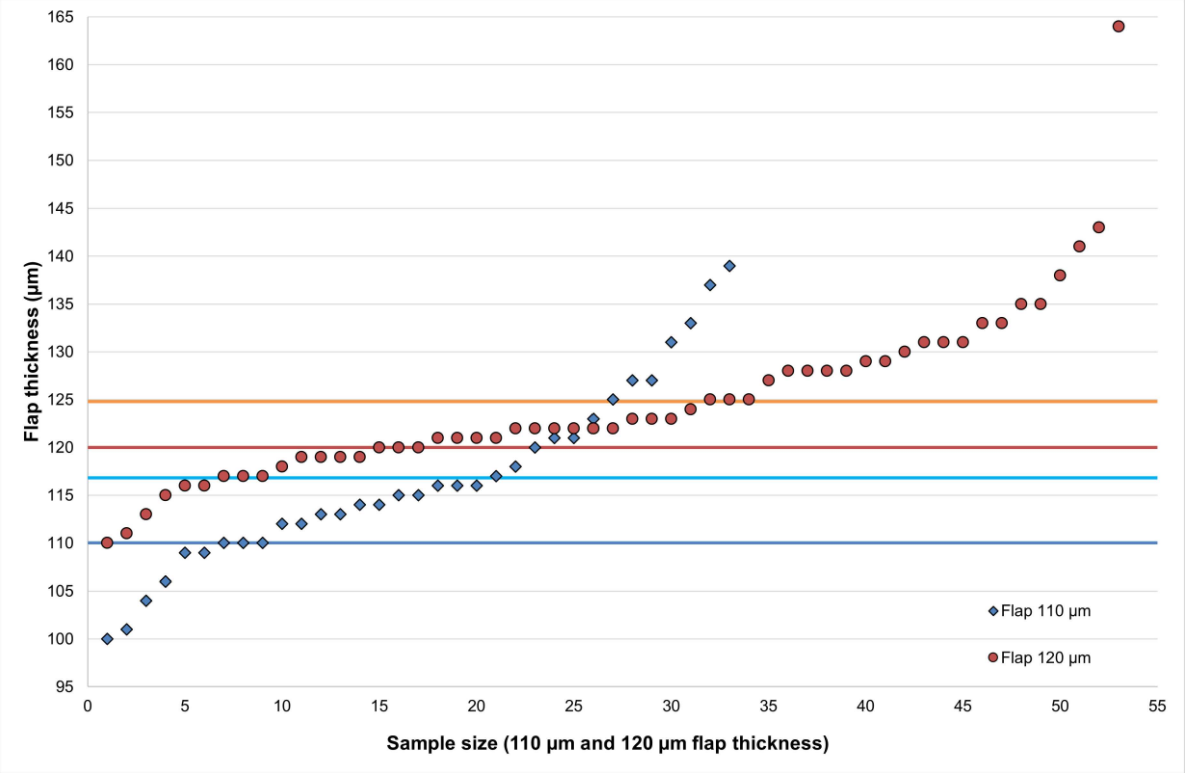

Figure 40 – Distribution of flap thickness measurements. Blue diamonds represent the measurements for expected flap value of 110 µm; Red dots represent the measurements for expected flap value of 120 µm; Dark blue line corresponds to the exact flap value of 110 µm; Light blue line corresponds to the mean of the measurements of 110 µm flap (116.8 µm); Red line corresponds to the exact flap value of 120 µm; Orange line corresponds to the mean of the measurements of 120 µm flap (124.8 µm).

Our results indicated that iFS tended to cut a slightly thicker flap than expected. However, although statistically significant, these differences may not be clinically relevant, given the fact that the mean differences did not exceed 7 µm.

4.3. Devices comparison

Different pachymetry measuring devices apply different internal algorithms in order to calculate pachymetry values. This might give rise to discrepancies between the output of different devices. We collected all the measurements of CCT, preoperatively and postoperatively, from the acquisitions of three devices to evaluate the comparability of these measurements. Visante serves as our reference device, since pachymetry was manually measured and because of its highest measurement accuracy (with a ± 1.5 µm error, approximately).

4.3.1 Preoperative

Figure 41 to Figure 43, show the distribution of the preoperative measurements from Visante, Orbscan and Pentacam devices, respectively. Descriptive statistics are shown in Table 25 and test of normality in Table 26 (both shown in Annexes).

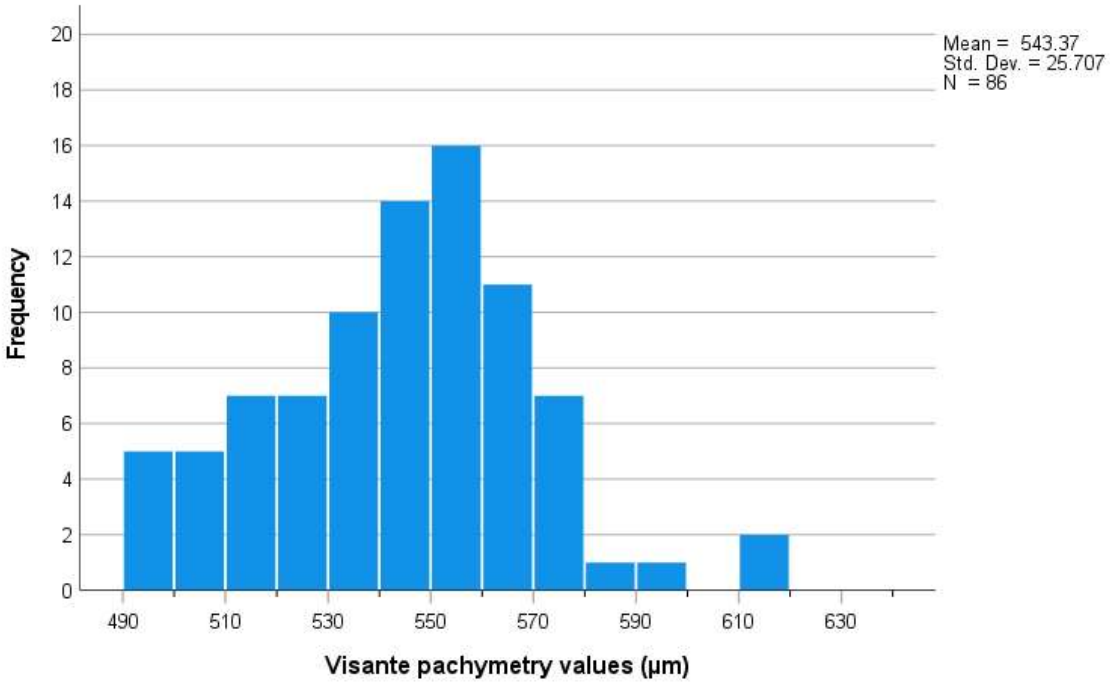

Figure 41 – Distribution of Visante pachymetry values.

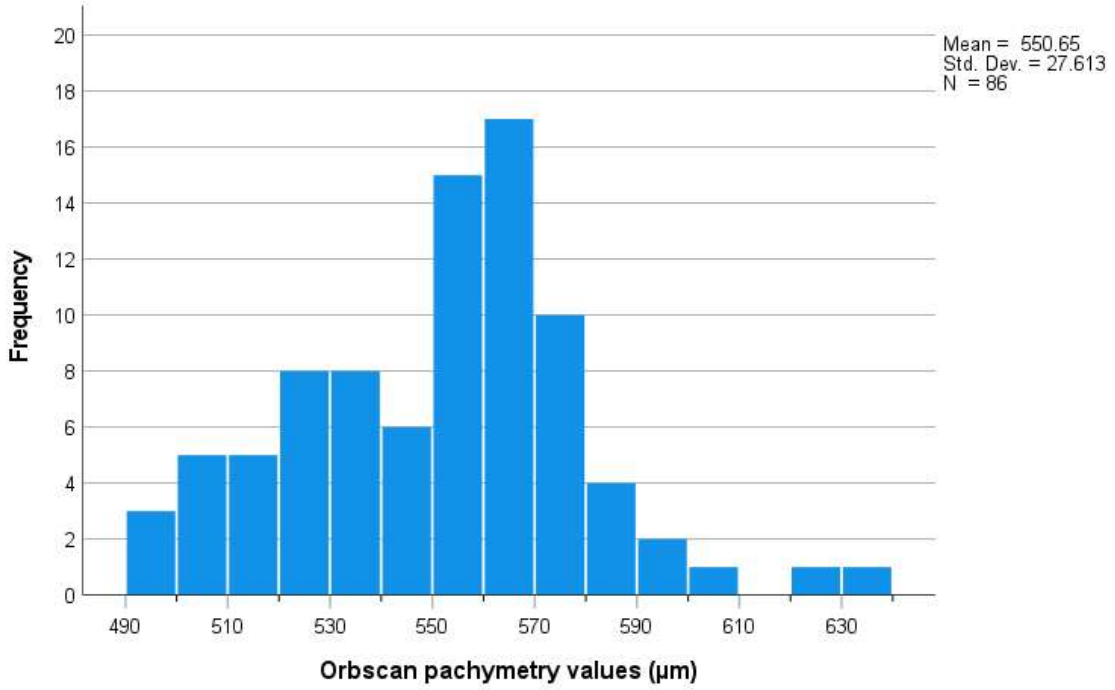

Figure 42 – Distribution of Orbscan pachymetry values.

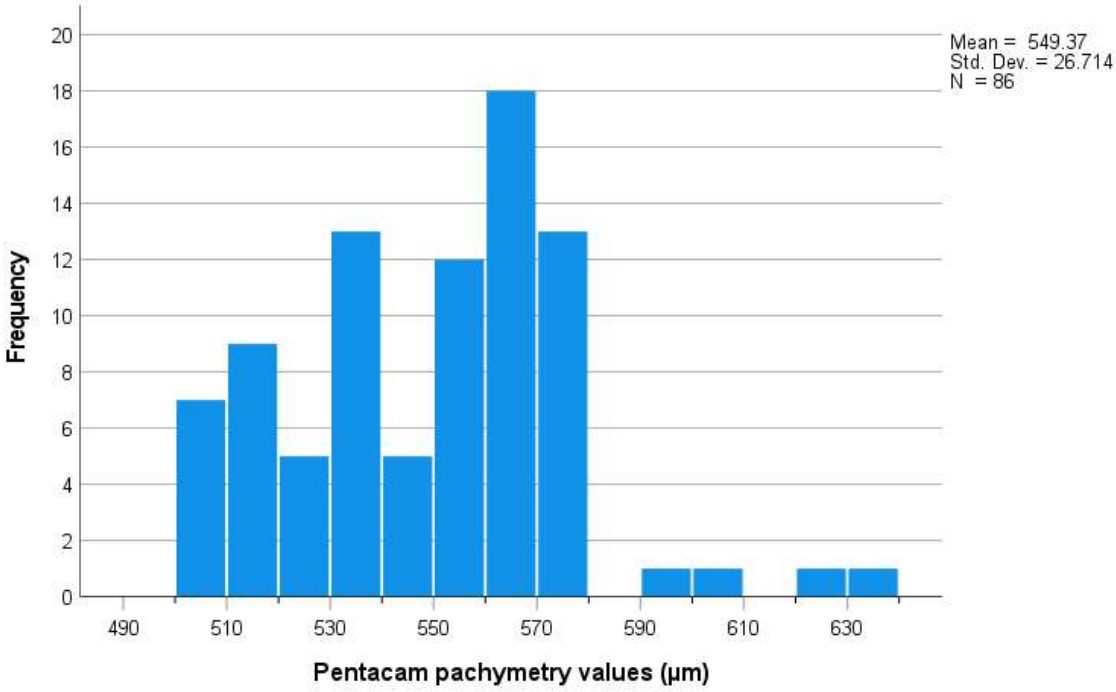

Figure 43 – Distribution of Pentacam pachymetry values.

In Figure 44, we can see the dispersion of CCT acquired in Visante, Orbscan and Pentacam, and conclude that there were no significant differences between Visante and the other two devices. Additionally, we observe that our sample had two eyes with a ticker pachymetry than the rest of our population, represented by two moderate outliers in each device.

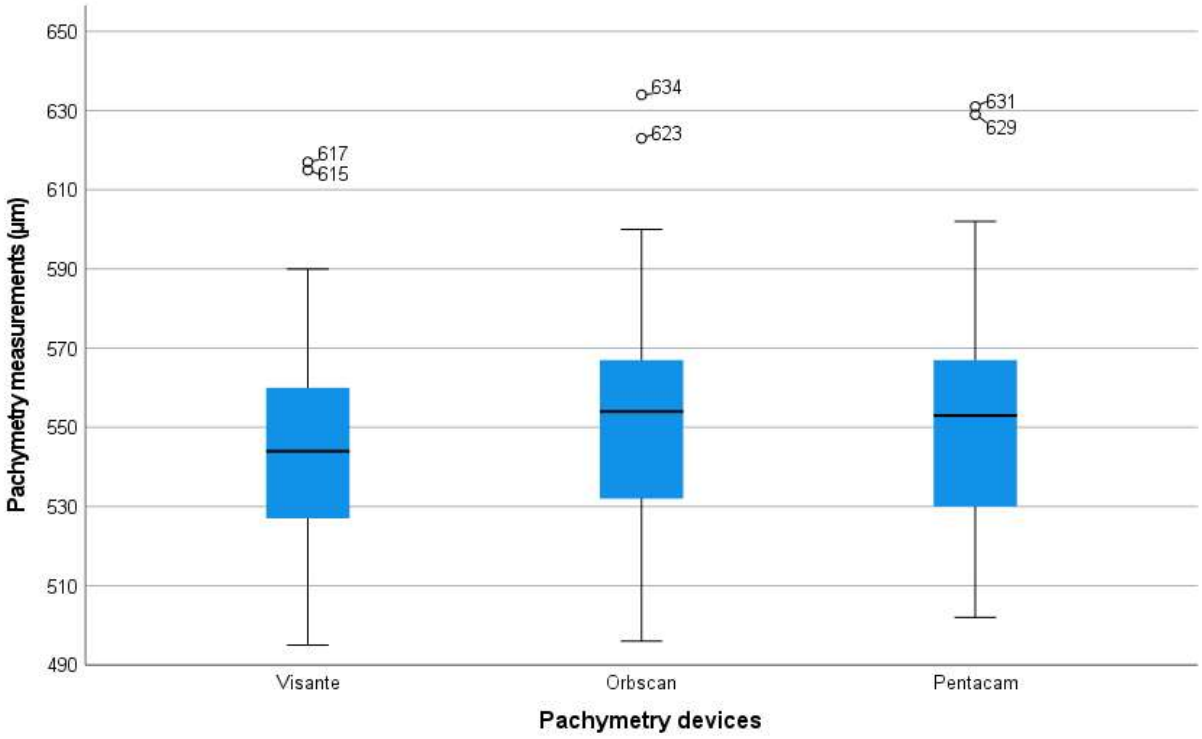

Figure 44 – Pachymetry measurements from Visante, Orbscan and Pentacam**.**

Our null hypotheses stated that the mean measurements taken from Visante were equal to the mean measurements taken from Orbscan or Pentacam. The alternative hypotheses stated that the mean measurements taken from Visante were not equal to the mean measurements taken from Orbscan or Pentacam:

$$H_0: \mu_{\text{Visante measurements}} = \mu_{\text{Orbscan measurements}}$$
$$H_A: \mu_{\text{Visante measurements}} \neq \mu_{\text{Orbscan measurements}}$$

and,

$$H_0: \mu_{\text{Visante measurements}} = \mu_{\text{Pentacam measurements}}$$
$$H_A: \mu_{\text{Visante measurements}} \neq \mu_{\text{Pentacam measurements}}$$

Therefore, we can see that neither Orbscan nor Pentacam values were statistically different from Visante values (Bonferroni adjusted p-values of 0.15 and 0.27, see Table 27 and Table 28, respectively, in Annexes). This means that pachymetry values extracted from Orbscan and Pentacam tended to not be statistically different from those measured by Visante, with a relatively small effect, in both cases (Cohen's d of -0.273 and -0.229, see Table 29 and Table 30, respectively, in Annexes).
Figure 45 depicts the distribution of each measurement between Orbscan and Pentacam, compared to the Visante reference. Despite the lack of statistically significant differences, here we can see that both Orbscan and Pentacam measurements had a small tendency to get further away from the Visante reference line, with Orbscan presenting a larger overall deviation. In both cases, they tended to overestimate the pachymetry when compared to Visante.

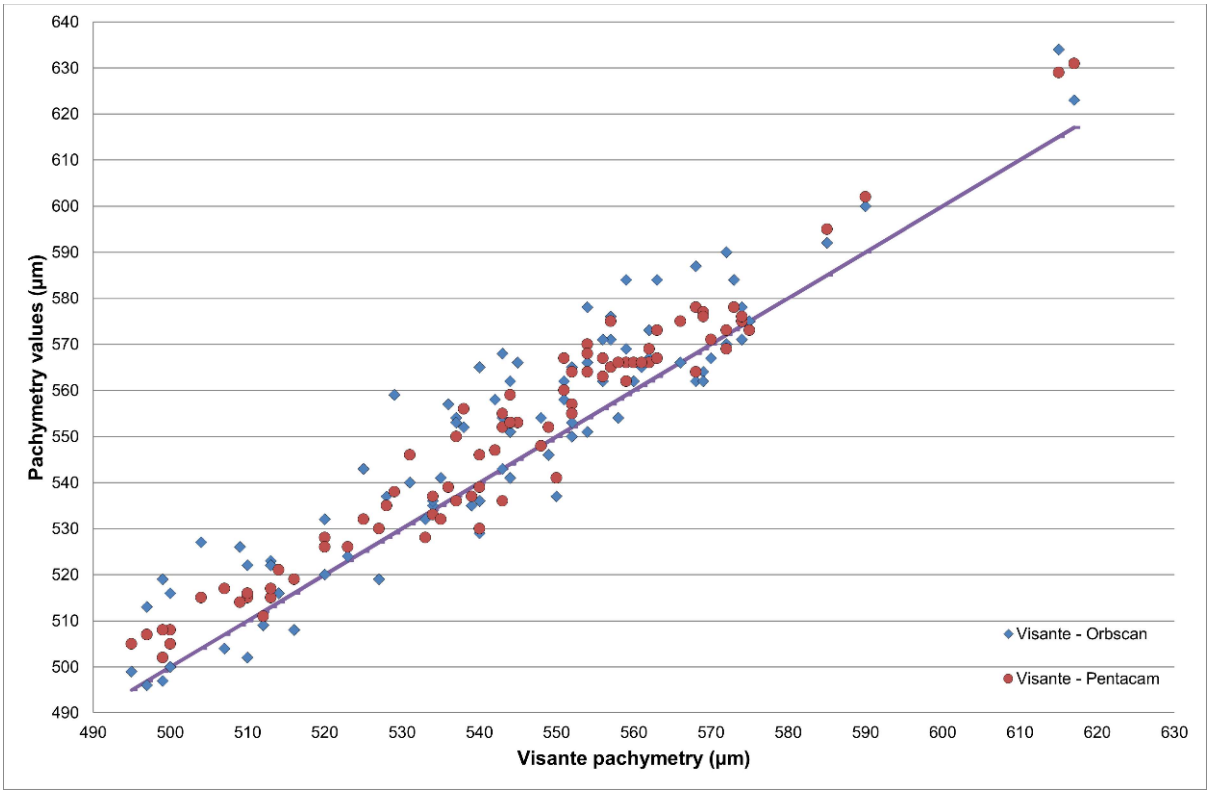

Figure 45 – Dispersion of pachymetry values**.** Blue diamonds represent the matching pachymetry between Visante and Orbscan; Red dots represent the matching pachymetry between Visante and Pentacam; Purple line corresponds to Visante's pachymetry which stands as reference.

In Figure 46, we present the differences between each measurement of Visante with Orbscan (Δorbscan) and Pentacam (Δpentacam). It is noticeable that the average values of pachymetry differences from both devices were quite close to those of Visante (see Table 31). The mean of Δorbscan is -7.3 µm and the mean value of Δpentacam is -6.0 µm. Therefore, this showed that Pentacam tended to be closer to Visante values, when compared to Orbscan. We have also calculated the SD of the differences between both devices versus Visante, which gave us an estimate of their accuracy. The SD values of Δorbscan and Δpentacam were ± 9.9 µm and ± 5.8 µm, respectively. This proved that Orbscan had a higher difference of results from Visante, when compared to Pentacam. Furthermore, this can be seen graphically, as the blue diamonds' dispersion tended to be quite larger than the red dots' dispersion. However, both devices tended mostly to overestimate pachymetry when compared to Visante measurements**.**

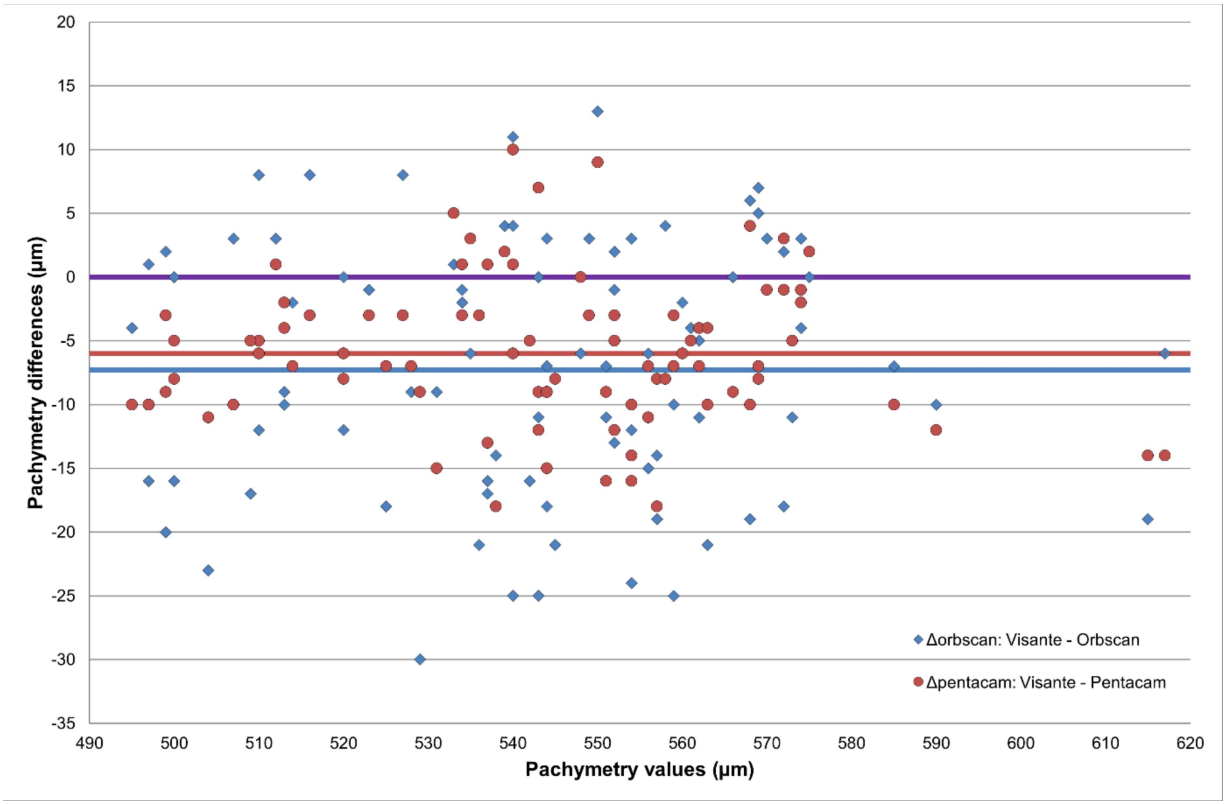

Figure 46 – Distribution of the differences in pachymetry measurements. Blue diamonds represent Δorbscan; Red dots represent Δpentacam; Purple line stands as reference for Visante's measurements; Blue line corresponds to the mean of Δorbscan (-7.3 µm); Red line corresponds to the mean of Δpentacam (-6.0 µm).

4.3.2. Postoperative

In Figure 47 to Figure 49, we can see the distribution of the postoperative measurements from Visante, Orbscan and Pentacam devices, respectively. Descriptive statistics can be found in Table 32 and test of normality in Table 33 (both shown in Annexes).

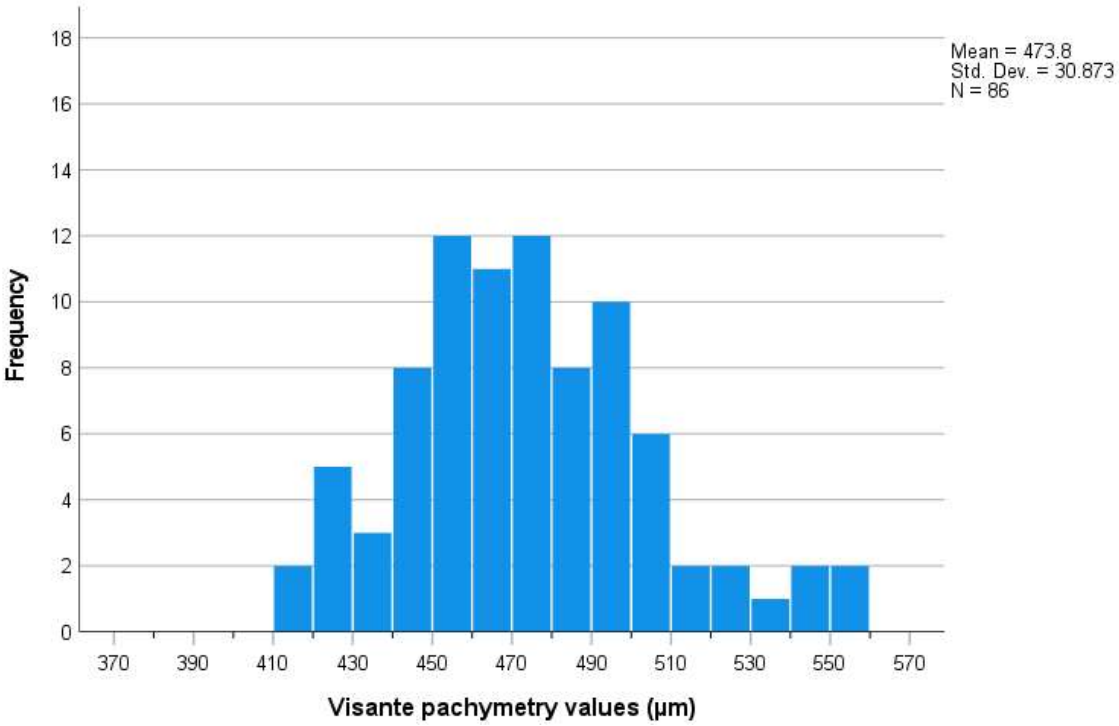

Figure 47 – Distribution of Visante pachymetry values.

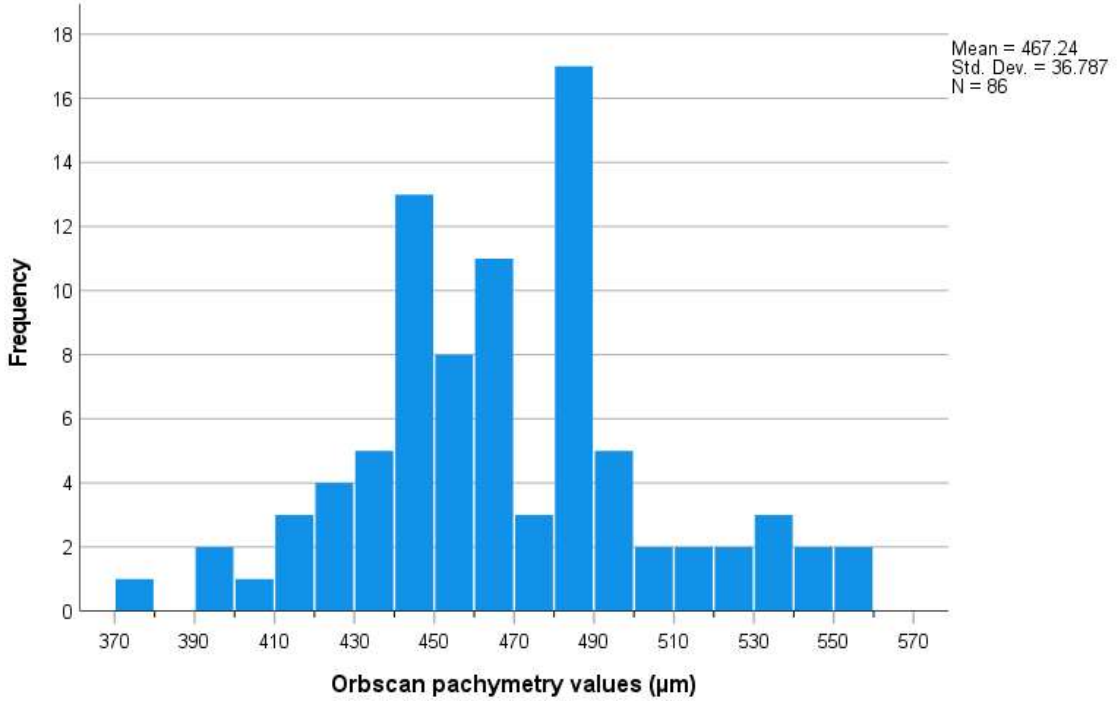

Figure 48 – Distribution of Orbscan pachymetry values.

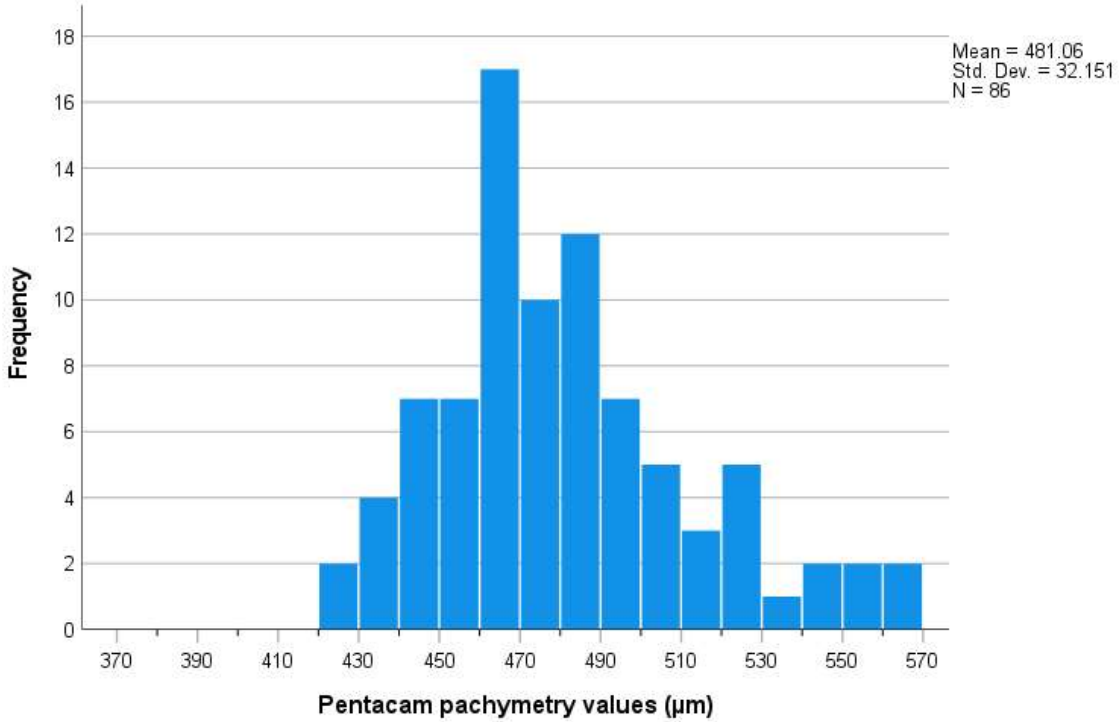

Figure 49 – Distribution of Pentacam pachymetry values.

Figure 50 shows the dispersion of pachymetry acquired in Visante, Orbscan and Pentacam. We may conclude that there were no significant differences between the pachymetry values obtained from Visante and any of the other devices. Additionally, we observe an inferior moderate outlier in Orbscan of 373 µm, which was the most divergent value obtained.

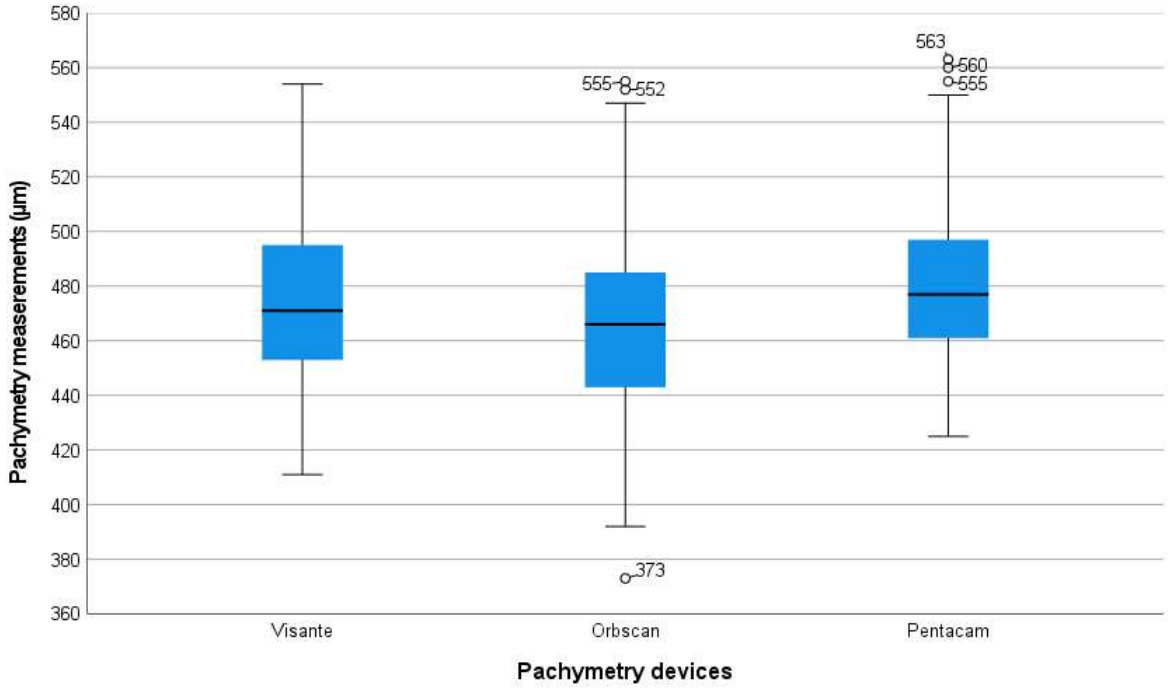

Figure 50 – Pachymetry measurements from Visante, Orbscan and Pentacam.

Our null hypotheses stated that the mean measurements taken from Visante were equal to the mean measurements taken from Orbscan or Pentacam. The alternative hypotheses stated that the mean measurements taken from Visante were not equal to the mean measurements taken from Orbscan or Pentacam:

$$H_0: \mu_{\text{Visante measurements}} = \mu_{\text{Orbscan measurements}}$$
$$H_A: \mu_{\text{Visante measurements}} \neq \mu_{\text{Orbscan measurements}}$$

and,

$$H_0: \mu_{\text{Visante measurements}} = \mu_{\text{Pentacam measurements}}$$
$$H_A: \mu_{\text{Visante measurements}} \neq \mu_{\text{Pentacam measurements}}$$

We can see that neither Orbscan nor Pentacam values were statistically different from Visante values (Bonferroni adjusted p-values of 0.41 and 0.27, see Table 34 and Table 35, respectively, in Annexes). This means that pachymetry values extracted from Orbscan and Pentacam tended to not be statistically different from those measured by Visante, with a relatively small effect in both cases (Cohen's d of 0.193 and -0.230, see Table 36 and Table 37, respectively, in Annexes).

In Figure 51, we can observe the distribution of each measurement between Orbscan and Pentacam, compared to the Visante, as a reference. Here, we can see that Orbscan measurements had a small tendency to get further away from the reference line, when compared with Pentacam measurements. While Orbscan measurements tended to slightly underestimate pachymetry, Pentacam measurements tended to slightly overestimate pachymetry, when compared to the Visante measurements.

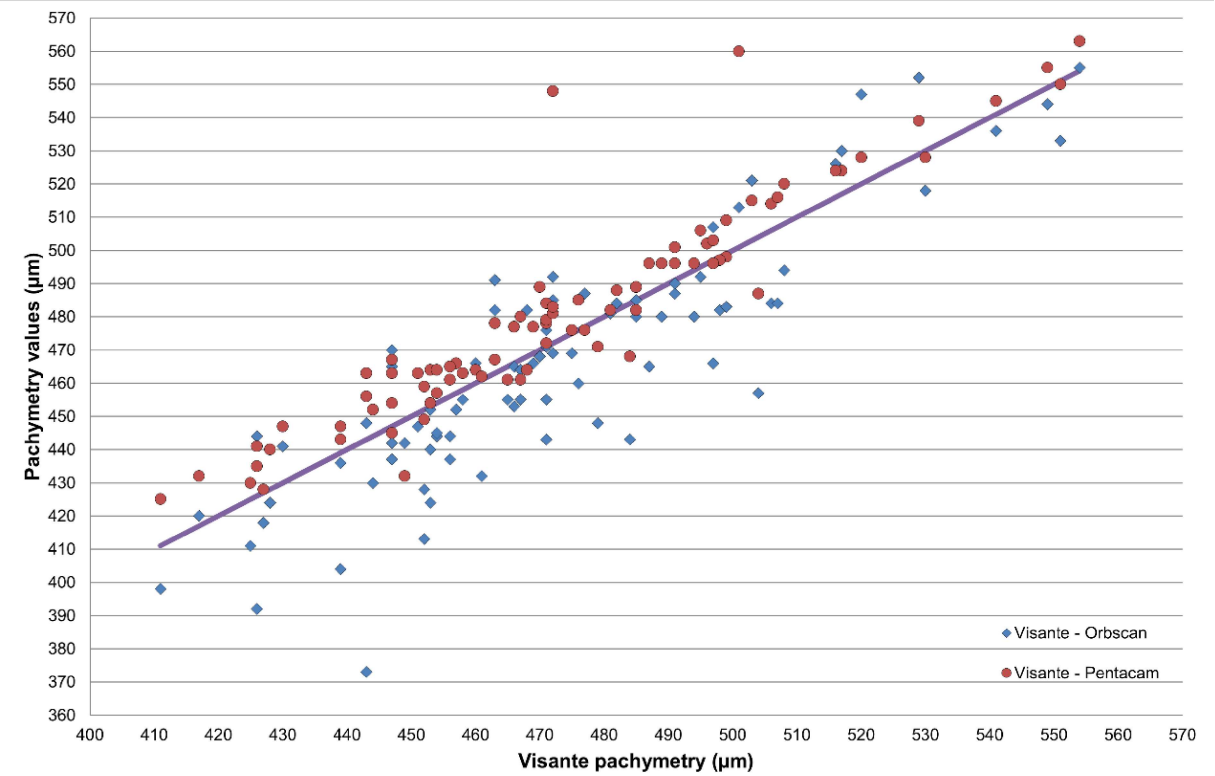

Figure 51 – Dispersion of pachymetry values. Blue diamonds represent the matching pachymetry between Visante and Orbscan; Red dots represent the matching pachymetry between Visante and Pentacam; Purple line corresponds to Visante's pachymetry which stands as reference.

In Figure 52, we present the differences between each measurement of Visante with Orbscan (Δorbscan) and Pentacam (Δpentacam). It is noticeable that the average values of pachymetry differences from both devices were quite close to those of Visante (see Table 38). The mean of Δorbscan is 6.6 µm and the mean value of Δpentacam is -7.3 µm. We have also calculated the SD of the differences between both devices versus Visante, which gave us an estimate of their accuracy. The SD of Δorbscan and Δpentacam were ± 17.3 µm and ± 11.9 µm, respectively. This proved that Orbscan still had a higher difference of results from Visante, when compared to Pentacam, in postoperative measurements. Once again, this is clearly shown graphically, as the blue diamonds' dispersion, tended to be quite larger than the red dots' dispersion. Orbscan measurements tended to underestimate pachymetry, while Pentacam measurements tended to overestimate pachymetry, when compared to Visante measurements.

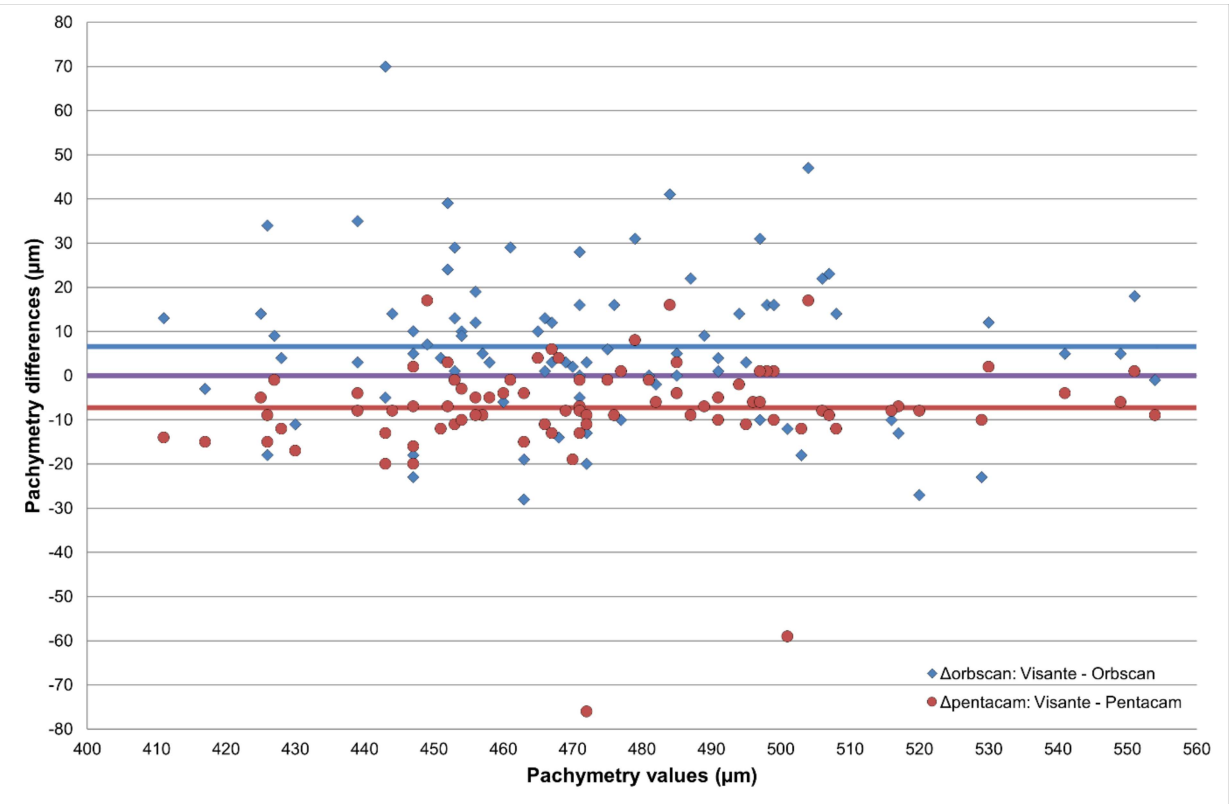

Figure 52 – Distribution of the differences in pachymetry measurements. Blue diamonds represent Δorbscan; Red dots represent Δpentacam; Purple line stands as reference for Visante's measurements; Blue line corresponds to the mean Δorbscan (6.6 µm); Red line corresponds to the mean Δpentacam (-7.3 µm).

To conclude, we found that, while Orbscan average measurements were not statistically different from Visante's, it tended to have larger variances and to mostly overestimate pachymetry in preoperative measurements and mostly underestimate pachymetry in postoperative data. Pentacam also presented average measurements that were statistically not different from Visante's, but showed much lower variances in its output. Nevertheless, there was a slight tendency to consistently overestimate the pachymetry, both in pre- and postoperative measurements.

5. Discussion

The main purpose of our study was to compare the measurements acquired from Visante for the real ablation depth, with the simulated values from the laser excimer software, for two types of treatments (Proscan and Zyoptix), to know how accurate these simulations were, and also to compare them with both approximated and exact Munnerlyn's formulas, to investigate if these formulas are still reliable. Considering the data we have collected in our study, we can conclude that for the Proscan treatment the excimer simulation is often accurate, however it tended to slightly overestimate ablation (the mean value for Δexcimer is -11 μm and its SD is ± 11 μm) when compared to real measurements. Regarding the approximated and exact Munnerlyn's formulas, the surgeon can rely on both formulas to simulate the ablation depth (the mean value for Δapproximated is 4 μm with a SD of ± 11 μm and Δexact is -4 μm with a SD of ± 11 μm). As for the Zyoptix treatment, the excimer simulation is the most accurate when compared to the real measurements (the mean value for Δexcimer is -1 μm and its SD is ± 13 μm), however both approximated and exact Munnerlyn's formulas turn out to be unreliable, and were proven to be statistically different (the mean value for Δapproximated is 33 μm with a SD of ± 20 μm and Δexact is 26 μm with a SD of ± 19 μm). This may be due to the fact that Zyoptix is a customized treatment that takes into account ocular aberrations of each specific patient, and that this aberration effect is not considered in Munnerlyn's formulas.

Using the collected data, we also investigated whether the flap thickness programmed in iFS during the surgery was comparable to the real value measured by Visante. We showed that Visante measurements, for both 110 μm and 120 μm flap thickness were significantly different from the expected values. However, the measurements obtained for flap thickness were much closer to the expected value of 120 μm than those for a flap thickness of 110 μm. Nevertheless, the mean differences did not exceed 7 μm with a SD of ± 10 μm, which in most clinical setting is a negligible deviation.

Finally, we compared Visante measurements with those of Orbscan and Pentacam to assess device comparability and accuracy. Even though both Orbscan and Pentacam devices tended to be accurate when compared to Visante, we did find some differences. Considering our sample in preoperative measurements, the SD of Δorbscan and Δpentacam were ± 9.9 μm and ± 5.8 μm, respectively. Nonetheless, when comparing to postoperative measurements, where the pachymetry is often thinner, the SD values were higher, i.e., ± 17.3 μm and ± 11.9 μm for Δorbscan and Δpentacam, respectively. Moreover, while Pentacam tended to slightly overestimate the pachymetry (pre- and postoperatively), Orbscan tended to mostly underestimate thinner pachymetry and overestimate thicker pachymetry. These small differences in pachymetry, may be due to the fact that each device has different acquisition methods. Despite this, we consider it is important to study the pachymetry of refractive surgery candidates with different devices, especially when close to the value of 250 μm of residual stromal bed and/or to a PTA of 40%, to prevent future complications, namely corneal ectasia.

A limitation of the current thesis is that the measurements were acquired by different orthoptists, which can lead to slightly different results in pachymetry. Therefore, to guarantee the same precision among all data, it will be important in future studies, to have the same orthoptist acquiring all the measurements. Another limitation in this study was the lower affluence to the refractive surgery during

the pandemic period, which delayed and shortened the expected sample of treated eyes. Also, due to the pandemic period, there were many no shows in postoperative evaluations, leading to the exclusion of those patients from the database.

Some relevant topics of investigation for future studies, include evaluating the flap thickness, individually for each surgeon. It would also be relevant to expand the sample size in the ablation depth analysis, increasing the statistical analysis power and better understanding if the excimer laser software needs improvements. This should ultimately result in an algorithm that might increase predictability of future excimer laser refractive surgeries, improving their results and, consequently postoperative patient satisfaction and quality of life.

6. Conclusion

In this work, we highlighted the importance of assessing different methodologies for calculating ablation depth and pachymetry. While some tools produced similar results, under certain circumstances, others underperformed. Proscan and Zyoptix ablations were proven to be accurate when compared with Δexcimer (with a mean value and SD of -11 µm and ± 11 µm, respectively for Proscan and -1 µm and ± 13 µm, respectively for Zyoptix). In Proscan treatments, Munnerlyn's formulas have demonstrated to be accurate (with a mean and SD of 4 µm and ± 11 µm, respectively for Δapproximated, and with a mean and SD of -4 µm and ± 11 µm, respectively for Δexact). Regarding Zyoptix treatments, Munnerlyn's formulas were shown to be unreliable, essentially underestimating ablation depth (with a mean and SD of 33 µm and ± 20 µm, respectively for Δapproximated, and with a mean and SD of 26 µm and ± 19 µm, respectively for Δexact), specially for ablation depth values above 110 µm.

Regarding the flap thickness, statistical analysis proved that flap thickness programmed in iFS did not match the expectation. The accuracy of iFS regarding its SD was ± 10 µm, which is clinically irrelevant. This could be considered as a safe margin from the device, in order to avoid thinner flaps, which could increase flap complications.

In terms of pachymetry acquisition, we found that large variances can lead to gross mismatches between devices output. Orbscan had, overall, the most uncertain measurements when comparing to our control device. It showed an overestimation of values in preoperative (mean of 7 µm above Visante measurements) and an underestimation in the postoperative data (mean of 7 µm below Visante measurements). In terms of precision, Orbscan had the tendency to be the most unpredictable (Δorbscan SD of ± 10 µm and ± 17 µm, pre- and postoperative, respectively), when comparing to Pentacam (Δpentacam SD of ± 6 µm and ± 12 µm, pre- and postoperative, respectively). As for Pentacam, it had the most regular measurements when comparing to our control device, although it often overestimated the pachymetry (mean of 6 µm and 7 µm above Visante measurements, in pre- and postoperative, respectively). These findings underline the importance of utilizing different evaluation approaches in order to mitigate uncertainty, improving candidate eligibility for laser refractive surgery.

Overall, we can conclude that ablation depth predicted by the excimer simulation is the closest to the actual ablation treatments. However, none of the studied categories were 100% accurate with their respective prediction and the results were sometimes quite disperse. Regarding the studied pachymetry devices and flap thickness evaluation, it is mandatory to know their precision in order to have confidence in their results.

.

Bibliography

[1] Febbraro JL, Picard H, Moran S, Grise-Dulac A, Salomon L, Gatinel D. Comparison of laser platform estimation and objective measurement of maximum ablation depth using Scheimpflug pachymetry in myopic femtosecond laser in situ keratomileusis. Cornea. 2020;39(3):316–20. doi:10.1097/ICO.0000000000002143.

[2] Savini G, Cummings AB, Balducci N, Barboni P, Huang J, Lombardo M, *et al*. Agreement between predicted and measured ablation depth after femtosecond laser-assisted LASIK for myopia. J Refract Surg. 2016;32(3):164–70. doi:10.3928/1081597X-20160121-03.

[3] Santhiago MR. Changing a paradigm: PTA is more important than the residual stromal bed as a risk factor for post-LASIK ectasia. Rev Bras Oftalmol. 2015;74(2):61–2. doi:10.5935/0034-7280.20150014.

[4] Wolle MA, Randleman JB, Woodward MA. Complications of refractive surgery: ectasia after refractive surgery. Int Ophthalmol Clin. 2016;56(2):129–41. doi:10.1097/IIO.0000000000000102.

[5] Byun YS, Chung SH, Park YG, Joo CK. Posterior corneal curvature assessment after epi-LASIK for myopia: comparison of Orbscan II and Pentacam imaging. Korean J Ophthalmol 2012;26(1):6–9. doi:10.3341/kjo.2012.26.1.6.

[6] Li H, Leung CKS, Wong L, Cheung CYL, Pang CP, Weinreb RN, *et al*. Comparative study of central corneal thickness measurement with slit-lamp optical coherence tomography and visante optical coherence tomography. Ophthalmology. 2008;115(5):796-801.e2. doi:10.1016/j.ophtha.2007.07.006.

[7] Ferreira T. Improving strategies on toric intraocular lens power calculation. Dissertation. NOVA Medical School, Faculdade de Ciências Médicas. 2018. http://hdl.handle.net/10362/70297.

[8] Guérin LP, Le-Bel G, Desjardins P, Couture C, Gillard E, Boisselier É, *et al*. The human tissue-engineered cornea (hTEC): recent progress. Int J Mol Sci. 2021;22(3):1291. doi:10.3390/ijms22031291.

[9] Navaratnam J, Utheim TP, Rajasekhar VK, Shahdadfar A. Substrates for expansion of corneal endothelial cells towards bioengineering of human corneal endothelium. J Funct Biomater. 2015;6(3):917–45. doi:10.3390/jfb6030917.

[10] Sridhar MS. Anatomy of cornea and ocular surface. Indian J Ophthalmol. 2018;66(2):190–4. doi:10.4103/ijo.IJO_646_17.

[11] DelMonte DW, Kim T. Anatomy and physiology of the cornea. J Cataract Refract Surg. 2011;37(3):588–98. doi:10.1016/j.jcrs.2010.12.037.

[12] Meek KM, Knupp C. Corneal structure and transparency. Prog Retin Eye Res. 2015;49:1–16. doi:10.1016/j.preteyeres.2015.07.001.

[13] Rio-Cristobal A, Martin R. Corneal assessment technologies: current status. Surv Ophthalmol 2014;59(6):599–614. doi:10.1016/j.survophthal.2014.05.001.

[14] Eghrari AO, Riazuddin SA, Gottsch JD. Overview of the cornea: structure, function, and development. Prog Mol Biol Transl Sci. 2015;134:7-23. doi:10.1016/bs.pmbts.2015.04.001.

[15] Patel S, Tutchenko L. The refractive index of the human cornea: a review. Contact Lens Anterior Eye. 2019;42(5):575–80. doi:10.1016/j.clae.2019.04.018.

[16] Herbaut A, Liang H, Denoyer A, Baudouin C, Labbé A. Tear film analysis and evaluation of optical quality: a review of the literature. J Fr Ophtalmol. 2019;42(2):e21–35. doi:10.1016/j.jfo.2018.12.001.

[17] Blackburn BJ, Jenkins MW, Rollins AM, Dupps WJ. A review of structural and biomechanical changes in the cornea in aging, disease, and photochemical crosslinking. Front Bioeng Biotechnol. 2019;7:66. doi:10.3389/fbioe.2019.00066.

[18] Gayton JL. Etiology, prevalence, and treatment of dry eye disease. Clin Ophthalmol. 2009;3:405–12. doi:10.2147/opth.s5555.

[19] Dua HS, Faraj LA, Said DG, Gray T, Lowe J. Human corneal anatomy redefined: a novel pre-descemet's layer (Dua's layer). Ophthalmology. 2013;120(9):1778–85. doi:10.1016/j.ophtha.2013.01.018.

[20] Espana EM, Birk DE. Composition, structure and function of the corneal stroma. Exp Eye Res. 2020;198:108137. doi:https://doi.org/10.1016/j.exer.2020.108137.

[21] Cruzat A, Qazi Y, Hamrah P. In vivo confocal microscopy of corneal nerves in health and disease. Ocul Surf. 2017;15(1):15–47. doi:10.1016/j.jtos.2016.09.004.

[22] Shaheen BS, Bakir M, Jain S. Corneal nerves in health and disease. Surv Ophthalmol. 2014;59(3):263–85. doi:10.1016/j.survophthal.2013.09.002.

[23] Moshirfar M, Brown TW, Heiland MB, Rosen DB, Ronquillo YC, Hoopes PC. Comparative analysis of LASIK flap diameter and its centration using two different femtosecond lasers. Med Hypothesis Discov Innov Ophthalmol. 2019;8(3):241–9.

[24] Schiefer U, Kraus C, Baumbach P, Ungewiß J, Michels R. Refractive errors. Dtsch Arztebl Int. 2016;113(41):693–702. doi:10.3238/arztebl.2016.0693.

[25] Lang G. Ophthalmology - a pocket textbook atlas. 2nd ed. [New York]: Thieme. 2004.

[26] Costakos DM. Eye disorders. In: Kliegman RM, Lye PS, Bordini B, Toth H, Basel D, editor. Nelson pediatric symptom-based diagnosis. [place unknown]: Elsevier; 2017. p. 563–93. doi:10.1016/B978-0-323-39956-2.00032-7.

[27] Kaimbo DKW. Astigmatism – definition, etiology, classification, diagnosis and non-surgical treatment. In: Goggin M, editor. Astigmatism: optics, physiology and management. London: IntechOpen; 2012. p. 59-74. doi:10.5772/18132.

[28] Ambrósio R, Nogueira LP, Caldas DL, Fontes BM, Luz A, Cazal JO, *et al*. Evaluation of corneal shape and biomechanics before LASIK. Int Ophthalmol Clin. 2011;51(2):11–39. doi:10.1097/IIO.0b013e31820f1d2d.

[29] Kanellopoulos AJ. Scheimpflug vs scanning-slit corneal tomography: comparison of corneal and anterior chamber tomography indices for repeatability and agreement in healthy eyes. Clin Ophthalmol. 2020;14:2583–92. doi:10.2147/OPTH.S251998.

[30] Motlagh MN, Moshirfar M, Murri MS, Skanchy DF, Momeni-Moghaddam H, Ronquillo YC, *et al*. Pentacam® corneal tomography for screening of refractive surgery candidates: a review of the literature, part I. Med Hypothesis Discov Innov Ophthalmol. 2019;8(3):177–203.

[31] Spadea L, Giovannetti F. Main complications of photorefractive keratectomy and their management. Clin Ophthalmol. 2019;13:2305–15. doi:10.2147/OPTH.S233125.

[32] Resan M, Vukosavljević M, Milivojević M. Wavefront aberrations. In Rumelt S, editor. Advices in ophthalmolgy. [Servia]: InTech. 2012. p. 191 – 204.

[33] Unterhorst HA, Rubin A. Ocular aberrations and wavefront aberrometry: a review. Afr Vision Eye Health. 2015;74(1)1-6. doi:10.4102/aveh.v74i1.21.

[34] Dobos MJ, Twa MD, Bullimore MA. An evaluation of the Bausch & Lomb zywave aberrometer. Clin Exp Optom. 2009;92(3):238–45. doi:10.1111/j.1444-0938.2009.00360.x.

[35] Cook W, McKelvie J, Wallace H, Misra S. Comparison of higher order wavefront aberrations with four aberrometers. Indian J Ophthalmol. 2019;67(7):1030–5. doi:10.4103/ijo.IJO_1464_18.

[35] McAlinden C, Khadka J, Pesudovs K. A comprehensive evaluation of the precision repeatability and reproducibility) of the oculus pentacam HR. Invest Ophthalmol Vis Sci. 2011;52(10):7731–7. doi:10.1167/iovs.10-7093.

[37] Li X, Zhou Y, Young CA, Chen A, Jin G, Zheng D. Comparison of a new anterior segment optical coherence tomography and Oculus Pentacam for measurement of anterior chamber depth and corneal thickness. Ann Transl Med. 2020;8(14):857. doi:10.21037/atm-20-187.

[38] Oculus. Pentacam ® Pentacam ® HR Pentacam ® AXL OCULUS - Interpretation Guide. 3rd ed. 2005. interpretation_guideline_3rd_edition_0417.pdf (pentacam.com).

[39] Werkmeister RM, Sapeta S, Schmidl D, Garhöfer G, Schmidinger G, Aranha dos Santos V, *et al*. Ultrahigh-resolution OCT imaging of the human cornea. Biomed Opt Express. 2017;8(2):1221-39. doi:10.1364/boe.8.001221.

[40] Rio-San Cristobal A, Martin R, Morejona A, Galarreta D. Inter-examiner agreement of the AS-OCT visante corneal thickness. J Optom. 2011;4(3):95–102. doi:10.1016/S1888-4296(11)70048-6.

[41] Penner V, Rocha G. Use of the visante for anterior segment ocular coherence tomography. Techniques in Ophthalmology. 2007;5(2):67–77. doi:10.1097/ITO.0b013e31806f4b4c.

[42] Ang M, Baskaran M, Werkmeister RM, Chua J, Schmidl D, Aranha dos Santos V, *et al*. Anterior segment optical coherence tomography. Prog Retin Eye Res. 2018;66:132–56. doi:10.1016/j.preteyeres.2018.04.002.

[43] Kim T, Alió del Barrio JL, Wilkins M, Cochener B, Ang M. Refractive surgery. The Lancet. 2019;393(10185):2085–98. doi:10.1016/S0140-6736(18)33209-4.

[44] Hu L, Huang Y, Lin M. Excimer laser and femtosecond laser in ophthalmology. In: Viskup, R, editor. High energy and short pulse lasers. London: IntechOpen; 2016. p. 377-92. doi:10.5772/64238.

[45] Sandoval HP, Donnenfeld ED, Kohnen T, Lindstrom RL, Potvin R, Tremblay DM, *et al*. Modern laser in situ keratomileusis outcomes. J Cataract Refract Surg. 2016;42(8):1224–34. doi:10.1016/j.jcrs.2016.07.012.

[46] Khairat YM, Mohamed YH, Moftah IA, Fouad NN. Evaluation of corneal changes after myopic LASIK using the Pentacam®. Clin Ophthalmol. 2013;7:1771–6. doi:10.2147/OPTH.S48077.

[47] Pateras E, Efi K. Comparison between the real corneal ablation (excimer laser) and the theoretical (Munnerlyn's formula) and the residual corneal thickness after lasik compared to safety limits. Opth Clin Ther 2020;4(3):6–10.

[48] Marcos S, Llorente L, Dorronsoro C, Merayo-Lloves J. Refractive surgery. In Dartt DA, Besharse J, Dana R, editor. Encyclopedia of the Eye. [place unknown]: Elsevier. 2010. p. 1–8. doi:10.1016/B978-0-12-374203-2.00242-6.

[49] Ong HS, Farook M, Tan BBC, Williams GP, Santhiago MR, Mehta JS. Corneal ectasia risk and percentage tissue altered in myopic patients presenting for refractive surgery. Clin Ophthalmol. 2019;13:2003–15. doi:10.2147/OPTH.S215144.

[50] Parafita-Fernández A, García-Gonzalez M, Katsanos A, Gros-Otero J, Teus M. Two femtosecond laser LASIK platforms: comparison of evolution of visual acuity, flap thickness, and stromal optical density. Cornea. 2019;38(1):98–104. doi:10.1097/ICO.0000000000001784.

[51] Liu Q, Zhou YH, Zhang J, Zheng Y, Zhai C Bin, Liu J. Comparison of corneal flaps created by wavelight FS200 and intralase FS60 femtosecond lasers. Int J Ophthalmol. 2016;9(7):1006–10. doi:10.18240/ijo.2016.07.12.

[52] Sarhan AR, Abd Elaziz MS, Zaki MA, Ibrahim AM, Youssef NG. Evaluation of corneal flap symmetry in the optical center by anterior segment optical coherence tomography: mechanical versus femtolaser flaps. Delta Journal of Ophthalmology. 2019;20(3):100-6. doi:10.4103/djo.djo_64_18.

[53] Chang AW, Tsang AC, Contreras JE, Huynh PD, Calvano CJ, Crnic-Rein TC, *et al*. Corneal tissue ablation depth and the Munnerlyn formula. J Cataract Refract Surg. 2003;29(6):1204–10. doi:10.1016/S0886-3350(02)01918-1.

[54] Aristeidou A, Taniguchi E V, Tsatsos M, Muller R, Mcalinden C, Pineda R, et al. The evolution of corneal and refractive surgery with the femtosecond laser. Eye Vis (Lond). 2015;2:12. doi:10.1186/s40662-015-0022-6.

[55] Tabacaru B, Stanca HT. One year refractive outcomes of femtosecond-LASIK in mild, moderate and high myopia. Rom J Ophthalmol. 2017;61(1):23–31. doi:10.22336/rjo.2017.5.

[56] Han DC, Chen J, Htoon HM, Tan DT, Mehta JS. Comparison of outcomes of conventional WaveLight® Allegretto Wave® and Technolas® excimer lasers in myopic laser in situ keratomileusis. Clin Ophthalmol. 2012;6:1159–68. doi:10.2147/OPTH.S29660.

[57] Crispim J, Allemann N, Hallak JA, Azar DT, De La Cruz J. Direct and indirect flap measurements in femtosecond laser-assisted in situ keratomileusis. Cornea. 2019;38(3):297–303. doi:10.1097/ICO.0000000000001836.

[58] Gil JQ, Lobo C, Tavares C, Costa E, Rosa AM, Quadrado MJ, *et al*. Guidelines for Excimer Laser Refractive Surgery on Cornea. Revista Sociedade Portuguesa de Oftalmologia. 2015;39(1):1–16. doi:10.48560/rspo.6907.

[59] Pidro A, Biscevic A, Pjano MA, Mravicic I, Bejdic N, Bohac M. Excimer lasers in refractive surgery. Acta Inform Med. 2019;27(4):278–83. doi:10.5455/aim.2019.27.278-283.

[60] Valbon B, Jr R, Gliceria J, Santos R, Luz A, Alves M. Unilateral corneal ectasia after bilateral LASIK: the thick flap counts. Int J Keratoconus Ectatic Corneal Dis. 2013;2(2):79–83. doi:10.5005/jp-journals-10025-1056.

[61] Motwani M. Biomechanical changes to the cornea from lasik flap creation resulting in inaccurate ablations and suboptimal refractive outcomes with topographic-guided ablation. Clinical Ophthalmology. 2020;14:2319–27. doi:10.2147/OPTH.S263896.

[62] Dai G. Wavefront optics for vision correction. Washington: Spie; 2008. doi:10.1117/3.769212.

[63] Tatar MG, Kantarci FA, Yildirim A, Uslu H, Colak HN, Goker H, *et al*. Risk factors in post-LASIK corneal ectasia. J Ophthalmol. 2014;2014:204191. doi:10.1155/2014/204191.

[64] Santhiago MR, Smadja D, Gomes BF, Mello GR, Monteiro MLR, Wilson SE, *et al*. Association between the percent tissue altered and post-laser in situ keratomileusis ectasia in eyes with normal preoperative topography. Am J Ophthalmol. 2014;158(1):87-95.e1. doi:10.1016/j.ajo.2014.04.002.

[65] Santhiago MR, Smadja D, Wilson SE, Krueger RR, Monteiro MLR, Randleman JB. Role of percent tissue altered on ectasia after LASIK in eyes with suspicious topography. J Refract Surg. 2015;31(4):258–65. doi:10.3928/1081597X-20150319-05.

[66] Ursea R, Feng M, Urs R, RoyChoudhury A, Silverman RH. Comparison of artemis 2 ultrasound and visante optical coherence tomography corneal thickness profiles. Journal of Refractive Surgery. 2013;29(1):36–41. doi:10.3928/1081597X-20121126-01.

Annexes

Table 1 – Descriptive statistics for four categories of ablation depth data. Please see Figure 22, Figure 23, Figure 24 and Figure 25.

	N	Minimum	Mean	Maximum	Std. Deviation
Real Measurement	45	12	57.69	118	28.539
Excimer Simulation	45	13	68.40	144	31.486
Approximated Munnerlyn	45	5	53.34	121	27.712
Exact Munnerlyn	45	6	61.25	137	31.360

Table 2 – Test of Normality for four categories of ablation depth data, it shows that all of them have a normal distribution since p-value > 0.05.

	Kolmogorov-Smirnov[a]			Shapiro-Wilk		
	Statistic	df	Sig.	Statistic	df	Sig.
Real Measurement	.118	45	.136	.950	45	.050
Excimer Simulation	.111	45	.200*	.968	45	.244
Approximated Munnerlyn	.090	45	.200*	.967	45	.224
Exact Munnerlyn	.091	45	.200*	.970	45	.299

*. This is a lower bound of the true significance.

a. Lilliefors Significance Correction

Table 3 – Independent Sample Test for real ablation depth and excimer simulation, since our sample had a normal distribution. Bonferroni adjusted p-value = 0.28 > 0.05, therefore we accept the null hypothesis.

		Levene's Test for Equality of Variances		t-test for Equality of Means						
									95% Confidence Interval of the Difference	
		F	Sig.	t	df	Sig. (2-tailed)	Mean Difference	Std. Error Difference	Lower	Upper
Values (µm)	Equal variances assumed	.088	.767	-1.691	88	.094	-10.711	6.335	-23.300	1.878
	Equal variances not assumed			-1.691	87.164	.094	-10.711	6.335	-23.302	1.880

Table 4 – Independent Sample Test for real ablation depth and approximated Munnerlyn formula, since our sample had a normal distribution. Bonferroni adjusted p-value = 1.00 > 0.05, therefore we accept the null hypothesis.

		Levene's Test for Equality of Variances		t-test for Equality of Means						
									95% Confidence Interval of the Difference	
		F	Sig.	t	df	Sig. (2-tailed)	Mean Difference	Std. Error Difference	Lower	Upper
Values (µm)	Equal variances assumed	.485	.488	.733	88	.466	4.345	5.930	-7.440	16.129
	Equal variances not assumed			.733	87.924	.466	4.345	5.930	-7.440	16.129

Table 5 – Independent Sample Test for real ablation depth and complex Munnerlyn formula, since our sample had a normal distribution. Bonferroni adjusted p-value = 1.00 > 0.05, therefore we accept the null hypothesis.

		Levene's Test for Equality of Variances		t-test for Equality of Means						
									95% Confidence Interval of the Difference	
		F	Sig.	t	df	Sig. (2-tailed)	Mean Difference	Std. Error Difference	Lower	Upper
Values (µm)	Equal variances assumed	.011	.918	-.563	88	.575	-3.561	6.321	-16.122	9.001
	Equal variances not assumed			-.563	87.230	.575	-3.561	6.321	-16.124	9.002

Table 6 – Independent Sample Effect Sizes for real ablation depth and excimer simulation, Cohen's d = -0.356, which indicates a small effect.

			Point	95% Confidence Interval	
		Standardizer[a]	Estimate	Lower	Upper
Values (µm)	Cohen's d	30.049	-.356	-.772	.061
	Hedges' correction	30.308	-.353	-.765	.061
	Glass's delta	31.486	-.340	-.758	.081

a. The denominator used in estimating the effect sizes.

Cohen's d uses the pooled standard deviation.

Hedges' correction uses the pooled standard deviation, plus a correction factor.

Glass's delta uses the sample standard deviation of the control group.

Table 7 – Independent Sample Effect Sizes for real ablation depth and approximated Munnerlyn formula, Cohen's d = 0.154, indicating a small effect.

		Standardizer[a]	Point Estimate	95% Confidence Interval Lower	Upper
Values (µm)	Cohen's d	28.129	.154	-.260	.568
	Hedges' correction	28.371	.153	-.258	.563
	Glass's delta	27.712	.157	-.259	.570

a. The denominator used in estimating the effect sizes.

Cohen's d uses the pooled standard deviation.

Hedges' correction uses the pooled standard deviation, plus a correction factor.

Glass's delta uses the sample standard deviation of the control group.

Table 8 – Independent Sample Effect Sizes for real ablation depth and exact Munnerlyn formula, Cohen's d = -0.119, showing a small effect.

		Standardizer[a]	Point Estimate	95% Confidence Interval Lower	Upper
Values (µm)	Cohen's d	29.983	-.119	-.532	.295
	Hedges' correction	30.241	-.118	-.527	.293
	Glass's delta	31.360	-.114	-.527	.301

a. The denominator used in estimating the effect sizes.

Cohen's d uses the pooled standard deviation.

Hedges' correction uses the pooled standard deviation, plus a correction factor.

Glass's delta uses the sample standard deviation of the control group.

Table 9 – Descriptive statistics of the different categories of ablation depth data with the real ablation depth. Please see Figure 27.

	N	Minimum	Mean	Maximum	Std. Deviation
Δexcimer	45	-36	-10.71	4	10.602
Δapproximated	45	-18	4.34	31	10.584
Δexact	45	-27	-3.56	21	11.175

Table 10 – Descriptive statistics for four categories of ablation depth data. Please see Figure 29, Figure 30, Figure 31 and Figure 32.

	N	Minimum	Mean	Maximum	Std. Deviation
Real Measurement	41	31	82.61	161	27.804
Excimer Simulation	41	39	83.07	131	23.224
Approximated Munnerlyn	41	15	50.06	90	18.216
Exact Munnerlyn	41	16	56.82	99	21.130

Table 11 – Test of Normality for four categories of ablation depth data, it shows that all of them have a normal distribution since p-value > 0.05.

	Kolmogorov-Smirnov[a]			Shapiro-Wilk		
	Statistic	df	Sig.	Statistic	df	Sig.
Excimer Simulation	.082	41	.200*	.981	41	.704
Real Measurement	.096	41	.200*	.970	41	.345
Approximated Munnerlyn	.078	41	.200*	.980	41	.675
Exact Munnerlyn	.055	41	.200*	.982	41	.753

*. This is a lower bound of the true significance.

a. Lilliefors Significance Correction

Table 12 – Independent Sample Test for real ablation depth and excimer simulation, since our sample had a normal distribution. Bonferroni adjusted p-value = 1.00 > 0.05, therefore we accept the null hypothesis.

		Levene's Test for Equality of Variances		t-test for Equality of Means						
									95% Confidence Interval of the Difference	
		F	Sig.	t	df	Sig. (2-tailed)	Mean Difference	Std. Error Difference	Lower	Upper
Values (µm)	Equal variances assumed	1.402	.240	-.277	88	.783	-1.566	5.665	-12.824	9.691
	Equal variances not assumed			-.277	83.596	.783	-1.566	5.665	-12.832	9.699

Table 13 – Independent Sample Test for real ablation depth and approximated Munnerlyn formula, since our sample had a normal distribution. Bonferroni adjusted p-value < 0.001 < 0.05, therefore we reject the null hypothesis.

		Levene's Test for Equality of Variances		t-test for Equality of Means						
									95% Confidence Interval of the Difference	
		F	Sig.	t	df	Sig. (2-tailed)	Mean Difference	Std. Error Difference	Lower	Upper
Values (µm)	Equal variances assumed	5.125	.026	5.071	88	.000	27.008	5.327	16.423	37.594
	Equal variances not assumed			5.071	76.349	.000	27.008	5.327	16.400	37.616

Table 14 – Independent Sample Test for real ablation depth and exact Munnerlyn formula, since our sample had a normal distribution. Bonferroni adjusted p-value < 0.001 < 0.05, therefore we reject the null hypothesis.

		Levene's Test for Equality of Variances		t-test for Equality of Means						
									95% Confidence Interval of the Difference	
		F	Sig.	t	df	Sig. (2-tailed)	Mean Difference	Std. Error Difference	Lower	Upper
Values (µm)	Equal variances assumed	3.594	.062	3.896	72	.000	24.262	6.228	11.846	36.677
	Equal variances not assumed			4.271	72.000	.000	24.262	5.681	12.937	35.586

Table 15 – Independent Sample Effect Sizes for real ablation depth and excimer simulation, Cohen's d = -0.058, which indicates a small effect.

			Point	95% Confidence Interval	
		Standardizer[a]	Estimate	Lower	Upper
Values (µm)	Cohen's d	26.871	-.058	-.471	.355
	Hedges' correction	27.102	-.058	-.467	.352
	Glass's delta	23.586	-.066	-.479	.347

a. The denominator used in estimating the effect sizes.

Cohen's d uses the pooled standard deviation.

Hedges' correction uses the pooled standard deviation, plus a correction factor.

Glass's delta uses the sample standard deviation of the control group.

Table 16 – Independent Sample Effect Sizes for real ablation depth and approximated Munnerlyn formula, Cohen's d = 1.069, indicating a large effect.

			Point	95% Confidence Interval	
		Standardizer[a]	Estimate	Lower	Upper
Values (µm)	Cohen's d	25.266	1.069	.624	1.509
	Hedges' correction	25.484	1.060	.619	1.496
	Glass's delta	19.723	1.369	.862	1.866

a. The denominator used in estimating the effect sizes.

Cohen's d uses the pooled standard deviation.

Hedges' correction uses the pooled standard deviation, plus a correction factor.

Glass's delta uses the sample standard deviation of the control group.

Table 17 – Independent Sample Effect Sizes for real ablation depth and exact Munnerlyn formula, Cohen's d = 0.928, showing a large effect.

		Standardizer[a]	Point Estimate	95% Confidence Interval Lower	Upper
Values (µm)	Cohen's d	26.154	.928	.434	1.415
	Hedges' correction	26.430	.918	.430	1.401
	Glass's delta	19.075	1.272	.692	1.837

a. The denominator used in estimating the effect sizes.

Cohen's d uses the pooled standard deviation.

Hedges' correction uses the pooled standard deviation, plus a correction factor.

Glass's delta uses the sample standard deviation of the control group.

Table 18 – Descriptive statistics of the different categories of ablation depth data with the real ablation depth. Please see Figure 35.

	N	Minimum	Mean	Maximum	Std. Deviation
Δexcimer	41	-23	-.46	30	12.898
Δapproximated	41	8	32.55	100	19.787
Δexact	41	-3	25.79	81	18.690

Table 19 – Descriptive statistics for flap thickness measurements data. Please see Figure 36 and Figure 37.

	N	Minimum thickness	Mean thickness Statistic	Std. Error	Maximum thickness	Std. Deviation
Flap 110 (µm)	33	100	116.79	1.656	139	9.516
Flap 120 (µm)	53	110	124.75	1.237	164	9.006

Table 20 – Test of Normality for flap thickness measurements data, 110 µm flap has a normal distribution since p-value > 0.05, and 120 µm flap has not a normal distribution since p-value < 0.05

	Kolmogorov-Smirnov[a]			Shapiro-Wilk		
	Statistic	df	Sig.	Statistic	df	Sig.
Flap 110 (µm)	.139	33	.105	.961	33	.276
Flap 120 (µm)	.143	53	.008	.879	53	.000

a. Lilliefors Significance Correction

Table 21 – One-Sample Test for flap with 110 µm thickness, since our sample had a normal distribution. p-value < 0.001 < 0.05, therefore we reject the null hypothesis.

	t	Df	Sig. (2-tailed)	Mean Difference	95% Confidence Interval of the Difference Lower	Upper
Flap 110 (µm)	4.098	32	.000	6.788	3.41	10.16

Table 22 – Hypothesis Test Summary (non-parametric test with Wilcoxon signed-rank) for flap with 120 µm thickness, since our sample had not a normal distribution. p-value < 0.001 < 0.05, therefore we reject the null hypothesis.

	Null Hypothesis	Test	Sig.	Decision
Flap 120 (µm)	The median of Flap 120 (µm) equals 120.	One-Sample Wilcoxon Signed Rank Test	.000	Reject the null hypothesis.

Asymptotic significances are displayed. The significance level is .050.

Table 23 – One-Sample Effect Sizes for flap with 110 µm thickness, Cohen's d = 0.713, which indicates a medium effect.

		Standardizer[a]	Point Estimate	95% Confidence Interval Lower	Upper
Flap 110 (µm)	Cohen's d	9.516	.713	.326	1.092
	Hedges' correction	9.746	.696	.318	1.066

a. The denominator used in estimating the effect sizes.

Cohen's d uses the sample standard deviation.

Hedges' correction uses the sample standard deviation, plus a correction factor.

Table 24 – One-Sample Effect Sizes for flap with 120 µm thickness, Cohen's d = 0.528, indicating a medium effect.

		Standardizer[a]	Point Estimate	95% Confidence Interval Lower	Upper
Flap 120 (µm)	Cohen's d	9.006	.528	.238	.813
	Hedges' correction	9.139	.520	.235	.802

a. The denominator used in estimating the effect sizes.

Cohen's d uses the sample standard deviation.

Hedges' correction uses the sample standard deviation, plus a correction factor.

Table 25 – Descriptive statistics for central corneal thickness (CCT) preoperative data. Please see Figure 41, Figure 42 and Figure 43.

	N	Minimum CCT	Mean CCT Statistic	Mean CCT Std. Error	Maximum CCT	Std. Deviation
Visante (µm)	86	495	543.37	2.772	617	25.707
Orbscan (µm)	86	496	550.65	2.978	634	27.613
Pentacam (µm)	86	502	549.37	2.881	631	26.714

Table 26 – Test of Normality for central corneal thickness preoperative data, it shows that all of them have a normal distribution since p-value > 0.05.

	Kolmogorov-Smirnov[a]			Shapiro-Wilk		
	Statistic	df	Sig.	Statistic	df	Sig.
Visante (µm)	.063	86	.200*	.972	86	.060
Orbscan (µm)	.086	86	.159	.975	86	.099
Pentacam (µm)	.095	86	.051	.955	86	.004

*. This is a lower bound of the true significance.

a. Lilliefors Significance Correction

Table 27 – Independent Sample Test for Visante and Orbscan measurements, since our sample had a normal distribution. Bonferroni adjusted p-value = 0.15 > 0.05, therefore we accept the null hypothesis.

		Levene's Test for Equality of Variances		t-test for Equality of Means						
									95% Confidence Interval of the Difference	
		F	Sig.	t	df	Sig. (2-tailed)	Mean Difference	Std. Error Difference	Lower	Upper
Measurement	Equal variances assumed	.604	.438	-1.789	170	.075	-7.279	4.068	-15.310	.752
	Equal variances not assumed			-1.789	169.137	.075	-7.279	4.068	-15.310	.752

Table 28 – Independent Sample Test for Visante and Pentacam measurements, since our sample had a normal distribution. Bonferroni adjusted p-value = 0.27 > 0.05, therefore we accept the null hypothesis.

		Levene's Test for Equality of Variances		t-test for Equality of Means						
									95% Confidence Interval of the Difference	
		F	Sig.	t	df	Sig. (2-tailed)	Mean Difference	Std. Error Difference	Lower	Upper
Measurement	Equal variances assumed	.432	.512	-1.501	170	.135	-6.000	3.998	-13.892	1.892
	Equal variances not assumed			-1.501	169.749	.135	-6.000	3.998	-13.892	1.892

Table 29 – Independent Samples Effect Sizes from Visante and Orbscan measurements. Cohen's d = -0.273, which indicates a small effect.

			Point	95% Confidence Interval	
		Standardizer[a]	Estimate	Lower	Upper
Measurement	Cohen's d	26.677	-.273	-.573	.028
	Hedges' correction	26.795	-.272	-.570	.028
	Glass's delta	27.613	-.264	-.564	.039

a. The denominator used in estimating the effect sizes.

Cohen's d uses the pooled standard deviation.

Hedges' correction uses the pooled standard deviation, plus a correction factor.

Glass's delta uses the sample standard deviation of the control group.

Table 30 – Independent Samples Effect Sizes from Visante and Pentacam measurements. Cohen's d = -0.229, indicating a small effect.

			Point	95% Confidence Interval	
		Standardizer[a]	Estimate	Lower	Upper
Measurement	Cohen's d	26.215	-.229	-.528	.071
	Hedges' correction	26.332	-.228	-.526	.071
	Glass's delta	26.714	-.225	-.525	.077

a. The denominator used in estimating the effect sizes.

Cohen's d uses the pooled standard deviation.

Hedges' correction uses the pooled standard deviation, plus a correction factor.

Glass's delta uses the sample standard deviation of the control group.

Table 31 – Descriptive statistics of the different categories of ablation depth data with the real ablation depth. Please see Figure 46.

	N	Minimum	Mean	Maximum	Std. Deviation
Δorbscan	86	-30	-7.28	13	9.923
Δpentacam	86	-18	-6.00	10	5.821

Table 32 – Descriptive statistics for central corneal thickness (CCT) postoperative data. Please see Figure 47, Figure 48 and Figure 49.

	N	Minimum CCT	Mean CCT		Maximum CCT	Std. Deviation
			Statistic	Std. Error		
Visante (μm)	86	411	473.80	3.329	554	30.873
Orbscan (μm)	86	373	467.24	3.967	555	36.787
Pentacam (μm)	86	425	481.06	3.467	563	32.151

Table 33 – Test of Normality for central corneal thickness postoperative data, it shows that all of them have a normal distribution since p-value > 0.05.

Tests of Normality

	Kolmogorov-Smirnov[a]			Shapiro-Wilk		
	Statistic	df	Sig.	Statistic	df	Sig.
Visante (μm)	.093	86	.063	.977	86	.125
Orbscan (μm)	.088	86	.099	.982	86	.295
Pentacam (μm)	.088	86	.093	.959	86	.008

a. Lilliefors Significance Correction

Table 34 – Independent Sample Test for Visante and Orbscan measurements, since our sample had a normal distribution. Bonferroni adjusted p-value = 0.41 > 0.05, therefore we accept the null hypothesis.

		Levene's Test for Equality of Variances		t-test for Equality of Means						
									95% Confidence Interval of the Difference	
		F	Sig.	t	df	Sig. (2-tailed)	Mean Difference	Std. Error Difference	Lower	Upper
Measurement	Equal variances assumed	1.702	.194	1.266	170	.207	6.558	5.179	-3.665	16.781
	Equal variances not assumed			1.266	165.033	.207	6.558	5.179	-3.667	16.783

Table 35 – Independent Sample Test for Visante and Pentacam measurements, since our sample had a normal distribution. Bonferroni adjusted p-value = 0.27 > 0.05, therefore we accept the null hypothesis.

		Levene's Test for Equality of Variances		t-test for Equality of Means						
									95% Confidence Interval of the Difference	
		F	Sig.	t	df	Sig. (2-tailed)	Mean Difference	Std. Error Difference	Lower	Upper
Measurement	Equal variances assumed	.083	.773	-1.510	170	.133	-7.256	4.806	-16.744	2.232
	Equal variances not assumed			-1.510	169.721	.133	-7.256	4.806	-16.744	2.232

Table 36 – Independent Samples Effect Sizes from Visante and Orbscan measurements. Cohen's d = 0.193, which indicates a small effect.

			Point	95% Confidence Interval	
		Standardizer[a]	Estimate	Lower	Upper
Measurement	Cohen's d	33.959	.193	-.107	.492
	Hedges' correction	34.110	.192	-.106	.490
	Glass's delta	36.787	.178	-.122	.478

a. The denominator used in estimating the effect sizes.

Cohen's d uses the pooled standard deviation.

Hedges' correction uses the pooled standard deviation, plus a correction factor.

Glass's delta uses the sample standard deviation of the control group.

Table 37 – Independent Samples Effect Sizes from Visante and Pentacam measurements. Cohen's d = -0.230, indicating a small effect.

			Point	95% Confidence Interval	
		Standardizer[a]	Estimate	Lower	Upper
Measurement	Cohen's d	31.518	-.230	-.530	.070
	Hedges' correction	31.658	-.229	-.527	.070
	Glass's delta	32.151	-.226	-.526	.076

a. The denominator used in estimating the effect sizes.

Cohen's d uses the pooled standard deviation.

Hedges' correction uses the pooled standard deviation, plus a correction factor.

Glass's delta uses the sample standard deviation of the control group.

Table 38 – Descriptive statistics of the different categories of ablation depth data with the real ablation depth. Please see Figure 52.

	N	Minimum	Mean	Maximum	Std. Deviation
Δorbscan	86	-28	6.56	70	17.341
Δpentacam	86	-76	-7.26	17	11.927